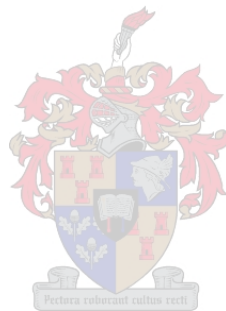


# Inverse Method for Static Load Reconstruction with Sensitivity Filtering and Optimal Sensor Placement

by

Mari Hanekom



*Thesis presented in partial fulfilment of the requirements for  
the degree of Master of Engineering (Mechanical) in the  
Faculty of Engineering at Stellenbosch University*

Supervisor: Prof. G. Venter

March 2021

# Declaration

By submitting this thesis electronically, I declare that the entirety of the work contained therein is my own, original work, that I am the sole author thereof (save to the extent explicitly otherwise stated), that reproduction and publication thereof by Stellenbosch University will not infringe any third party rights and that I have not previously in its entirety or in part submitted it for obtaining any qualification.

Date: ..... 2020/11/20 .....

Copyright © 2021 Stellenbosch University  
All rights reserved.

# Abstract

## Inverse Method for Static Load Reconstruction with Sensitivity Filtering and Optimal Sensor Placement

M. Hanekom

*Department of Mechanical and Mechatronic Engineering,  
University of Stellenbosch,  
Private Bag X1, Matieland 7602, South Africa.*

Thesis: MEng (Mech)

March 2021

Static load reconstruction is a technique that uses the surface strain response of a prototype structure, in conjunction with a numerical model, to determine the magnitude of the applied loads with a least-squares estimate. A unit-load finite-element (FE) model describes the relationship between every input load and the elemental output strain where each finite-element represents a potential location for mounting a strain gauge. The candidate set contains every desired potential gauge location-orientation combination (or candidate point). It is impossible to mount gauges at every candidate point, but with a D-optimal design, the optimal sensor placement can be determined. The response is assumed linear in order for the superposition principle to hold.

The D-optimal design selects elements that span the maximum volume of the candidate set, but makes no consideration for the practical aspects associated with mounting strain gauges. For example, during pilot studies, the design chose locations which were either inaccessible or where gauges measured incorrect strain values. A variety of filters have been designed to exclude specific elements from the candidate set to prevent any practical difficulties in mounting strain gauges. These filters are not limited to load reconstruction and can also be used in other strain gauge operations. The structural filters remove elements at open and sharp edges as well as triangular finite-elements. Next, incorrect values will be measured if the strain output is below the measuring capability of the sensor; thus, another filter excludes elements whose numerically computed strain values are below this

threshold. Experience has taught that a strain gauge should be mounted in an area of high strain, but of low strain gradient. The final filter is a statistical algorithm that considers high strain gradients to be outliers and utilises an adjusted boxplot method to remove candidate points that are associated with a high strain gradient.

Numerical experiments investigated the optimisation of various versions of the candidate set, as well as how the number of candidate points in the design matrix affects the reconstructed loads. All methods worked adequately, and more points in the design (proportionality) matrix improved the accuracy with which loads were calculated. During a physical experiment, it was found that a weighted average proportionality matrix should be used to reconstruct the applied loads if a strain gauge is glued over more than one finite-element. Furthermore, the most significant source of error between the calculated and actual loads originates from the differences between the FE and the actual model.

# Uittreksel

## **Inverse Metode vir die Berekening van Statiese Kragte met behulp van Sensitiwiteitsfiltering en Optimale Sensor Plasings**

*(“Inverse Method for Static Load Reconstruction with Sensitivity Filtering and Optimal Sensor Placement”)*

M. Hanekom

*Departement Meganiese en Megatroniese Ingenieurswese,  
Universiteit van Stellenbosch,  
Privaatsak X1, Matieland 7602, Suid Afrika.*

Tesis: MIng (Meg)

March 2021

Statische lasrekonstruksie is 'n tegniek wat die oppervlakterespons van 'n prototipe-struktuur gebruik om die grootte van die insetlaste te bepaal. As 'n prototipe van die struktuur bestaan, kan die vervorming op die oppervlak gebruik word, met behulp van 'n numeriese model, om die grootte van die insetlaste te bereken, mits die struktuur se respons linieêr is, sodat die beginsel van superposisie toegepas kan word. Die verhouding tussen die insetlaste en oppervlakvervorming kan bepaal word met behulp van 'n eenheidslas-eindige elementmodel, waar elke element in die eindige elementmodel 'n posisie voorstel waar 'n rekstrokie geplak kan word teen 'n sekere oriëntasie. Alle moontlike posisie-oriëntasie kombinasies word saamgestel in 'n enkele struktuur, wat die kandidaatstel genoem word. Dit is ontmoontlik om 'n rekstrokie by elke moontlik posisie-oriëntasie kombinasie (d.w.s kandidaatpunt) te plak, dus is 'n D-optimale ontwerp gebruik om optimale sensor plasings te bepaal.

Die D-optimale ontwerp kies kandidaatpunte wat strek oor die volume van die kandidaatstel, maar maak geen voorsiening vir die praktiese aanhegting van rekstrookies nie. Dit veroorsaak dat die algoritme elemente kies wat ontoeganklik is, of die rekstrokie verkeerde lesings meet. Filters is ontwerp om sekere elemente van die kandidaatstel te verwyder. Hierdie filters is nie beperk tot lasrekonstruksie nie en kan vir ander rekstrokie verwante toetse ook gebruik word. Die strukturele

filters verwyder alle driehoekige elemente, asook elemente wat teen oop en skerp rande gevind word vanuit die numeriese model. 'n Rekstrokie sal 'n verkeerde lesing meet indien dit geplak word waar die vervorming kleiner is as die minimum meetvermoë van die rekstrokie, dus moet elemente wat geassosieer word met 'n klein vervormingswaarde verwyder word van die kandidaatstel. Verder het ervaring geleer dat 'n rekstrokie ideaal in 'n area met hoë vervorming geplak moet word, maar waar die vervormingsgradiënt laag is. 'n Statistiese filter is ontwerp wat hoë spanningsgradiënte as uitskieters sien en 'n aangepaste 'boksplot' metode is gebruik om elemente, wat geassosieer word met hierdie uitskieters, vanuit die kandidaatstel te verwyder.

Numeriese eksperimente is uitgevoer om te ondersoek hoe verskillende variasies van die kandidaatstel die D-optimale ontwerp beïnvloed, asook hoe die aantal kandidaatspunte in die ontwerpsmatriks die rekonstruksie van insetlaste verander. Dit is bevestig dat alle variasies van die kandidaatstel bevredigend werk en dat hoe meer punte daar in die ontwerpsmatriks is, hoe meer akkuraat word die laste gerekonstrueer. Nadat al die bogenoemde oorwegings in ag geneem is, is 'n fisiese eksperiment uitgevoer. Daar is gevind dat indien 'n rekstrokie oor meer as een eindige-element geplak word, dat 'n geweegde gemiddelde ontwerpsmatriks gebruik moet word om die insetlaste te bereken. Verder is dit bevestig dat die grootste oorsaak van foute ontstaan uit verskille tussen die numeriese en die werklike model.

# Acknowledgements

I would like to sincerely thank Professor Gerhard Venter for not only his guidance but for being the creator of this study opportunity. Furthermore, a particular word of thanks to Louwrens Cuperus for his technical advice and guidance. I would also like to thank Pieter Hugo and Collin Moopanar from Transnet Engineering for allowing me the time to complete this project. Lastly, a special thank you to Christelle Van Eeden, Ferdi Zietsman and the Faculty of Engineering's Mechanical Workshop staff for their respective contributions and assistance.

# Dedications

*“An investment in knowledge pays the best interest.”*

*This thesis is dedicated to my parents, who do not always understand why I choose to take on specific endeavours, but continue to support me nonetheless.*



# Contents

<b>Declaration</b>	<b>i</b>
<b>Abstract</b>	<b>ii</b>
<b>Uittreksel</b>	<b>iv</b>
<b>Acknowledgements</b>	<b>vi</b>
<b>Dedications</b>	<b>vii</b>
<b>Contents</b>	<b>viii</b>
<b>List of Figures</b>	<b>xi</b>
<b>List of Tables</b>	<b>xvi</b>
<b>1 Introduction</b>	<b>1</b>
1.1 Project Background . . . . .	1
1.2 Project Scope and Objectives . . . . .	2
<b>2 Literature Review</b>	<b>3</b>
2.1 Load Reconstruction . . . . .	3
2.2 Multi-body System (MBS) Simulation . . . . .	4
2.3 Comparison of Methodologies . . . . .	5
2.4 Conclusion . . . . .	5
<b>3 Static Load Reconstruction</b>	<b>6</b>
3.1 Load Transducer Principle . . . . .	6
3.2 Proportionality Matrix . . . . .	8
3.2.1 Candidate Set . . . . .	8
3.2.2 Design Matrix . . . . .	9
3.3 Summary . . . . .	12

<b>4</b>	<b>Finite-element (FE) Model Preparations</b>	<b>14</b>
4.1	Two-dimensional (2D) Elements in Nastran . . . . .	14
4.2	Strain Gauge Considerations . . . . .	16
4.3	Mesh Size Considerations . . . . .	17
4.4	Geometrical Considerations . . . . .	18
4.5	Software Specific Considerations . . . . .	19
4.6	Summary . . . . .	20
<b>5</b>	<b>Software Development</b>	<b>21</b>
5.1	Filtering Software . . . . .	21
5.1.1	Sharp Edges Filter . . . . .	23
5.1.2	Open Edges Filter . . . . .	24
5.1.3	Triangular Element Filter . . . . .	25
5.1.4	Minimum Strains Filter . . . . .	26
5.1.5	Strain Gradient Filter . . . . .	26
5.1.6	Concluding Remarks . . . . .	32
5.2	Proportionality (or Design) Matrix Software . . . . .	34
5.3	Summary . . . . .	36
<b>6</b>	<b>Implementation of Filters</b>	<b>37</b>
6.1	Case Study I: Reinforced Pipe Simulations . . . . .	37
6.1.1	Structural Filters . . . . .	38
6.1.2	Strain Filters . . . . .	39
6.2	Case Study II: Hauler Truck Sub-Assembly . . . . .	45
6.2.1	Structural Filters . . . . .	45
6.2.2	Strain Filters . . . . .	45
6.3	Summary of Filter Selection . . . . .	48
<b>7</b>	<b>Numerical Investigations on Design Matrix</b>	<b>49</b>
7.1	Optimal Number of Strain Gauges . . . . .	51
7.2	Different Optimisation Methods . . . . .	52
7.3	Summary . . . . .	58
<b>8</b>	<b>Experimental Implementation</b>	<b>61</b>
8.1	Gauge Locations and Orientations . . . . .	62
8.2	Experimental Setup . . . . .	68
8.3	Measured Strain Values . . . . .	69
8.4	Actual Gauge Locations . . . . .	69
8.5	Load Reconstruction . . . . .	70
8.5.1	Load Case 1 . . . . .	72
8.5.2	Load Case 2 . . . . .	74

<i>CONTENTS</i>	<b>x</b>
8.5.3 Load Case 3 . . . . .	75
8.6 Summary . . . . .	77
<b>9 Conclusion</b>	<b>78</b>
9.1 Project Summary . . . . .	78
9.2 Future Recommendations . . . . .	79
<b>Appendices</b>	<b>81</b>
<b>A Gauge Placement Function</b>	<b>82</b>
A.1 Coordinate Systems in Nastran . . . . .	82
A.2 Mathematical Background . . . . .	83
A.2.1 Performance of Strain Gauge Placement Function . . . . .	85
<b>B Symmetric Outlier Detection Methods</b>	<b>87</b>
<b>C Filtering Function Application</b>	<b>91</b>
<b>D Additional Experimental Material</b>	<b>95</b>
D.1 Candidate Points of Unfiltered Candidate Set . . . . .	95
D.2 Measured Strain Responses . . . . .	97
D.3 Percentage Gauge Cover . . . . .	98
D.4 Averaged Design Matrix . . . . .	99
D.5 Weighted Averaged Design Matrix . . . . .	100
D.6 Additional Load Reconstruction Material . . . . .	102
D.6.1 Load Case 1 . . . . .	102
D.6.2 Load Case 2 . . . . .	103
D.6.3 Load Case 3 . . . . .	104
<b>List of References</b>	<b>106</b>

# List of Figures

3.1	Fixed cantilever beam with an axial and bending moment . . . . .	6
3.2	Arbitrary structure to illustrate the concept of superposition . . . . .	7
3.3	Matrix expansion of strain-load linear relationship . . . . .	10
3.4	Methodology for static load reconstruction . . . . .	13
4.1	Element geometry and associated coordinate systems of . . . . .	15
	(a) CQUAD4 elements . . . . .	15
	(b) CTRIA3 elements . . . . .	15
4.2	Cross-section of a two-dimensional (2D) element in Nastran . . . . .	17
4.3	Three-load cantilever beam for software compatibility demonstration .	19
4.4	Case Control section of Nastran's input file . . . . .	20
5.1	Sample FE model used to test the performance of filtering software . .	22
5.2	Unidirected graph of an FE model in a programming environment . . .	23
5.3	Results of the Sharp Edges filter on a sample FE model, selecting . . .	24
	(a) One layer . . . . .	24
	(b) Two layers . . . . .	24
5.4	Results of the Open Edges filter on a sample FE model, selecting . . .	25
	(a) One layer . . . . .	25
	(b) Two layers . . . . .	25
5.5	Results of the Triangular Element filter on a sample FE model, selecting	25
	(a) One layer . . . . .	25
	(b) Two layers . . . . .	25
5.6	Results of the Minimum Strain filter on a sample FE model . . . . .	26
5.7	Histogram of calculated strain gradients for the FE model in Figure 5.1	28
5.8	Boxplot with associated labels . . . . .	29
5.9	Results of the Strain Gradient filter on a sample FE model . . . . .	31
	(a) Standard boxplot method (113 outliers) . . . . .	31
	(b) Adjusted boxplot method (25 outliers) . . . . .	31
	(c) Strains of standard boxplot method . . . . .	31
	(d) Strains of adjusted boxplot method . . . . .	31
5.10	Results of all structural filtering on a sample FE model, selecting . . .	32

## LIST OF FIGURES

xii

(a)	One layer . . . . .	32
(b)	Two layers . . . . .	32
5.11	Comparison of the number of outliers detected with a standard and adjusted boxplot . . . . .	33
5.12	Data structures of strain values . . . . .	34
(a)	Dataframe as read from Nastran's OP2 file. . . . .	34
(b)	Dataframe constituting preliminary candidate set . . . . .	34
5.13	Schematic of in-plane strain transformation to demonstrate the rotation of gauges on the surface of a structure . . . . .	35
6.1	FE models of reinforced pipes as provided by Barry (2017) . . . . .	38
(a)	Collar Reinforced Tee . . . . .	38
(b)	Crotch Reinforced Tee . . . . .	38
(c)	Wrapper Reinforced Tee . . . . .	38
6.2	Structural filters on reinforced pipes with single layer removal . . . . .	40
(a)	Open Edges: Collar . . . . .	40
(b)	Sharp Edges: Collar . . . . .	40
(c)	Open Edges: Crotch . . . . .	40
(d)	Sharp Edges: Crotch . . . . .	40
(e)	Open Edges: Wrapper . . . . .	40
(f)	Sharp Edges: Wrapper . . . . .	40
6.3	Strain results of reinforced pipes . . . . .	41
(a)	Collar Reinforced Tee . . . . .	41
(b)	Crotch Reinforced Tee . . . . .	41
(c)	Wrapper Reinforced Tee . . . . .	41
6.4	Minimum Strains filter on reinforced pipes . . . . .	42
(a)	Collar Reinforced Tee . . . . .	42
(b)	Crotch Reinforced Tee . . . . .	42
(c)	Wrapper Reinforced Tee . . . . .	42
6.5	Strain Gradient filter on reinforced pipes . . . . .	43
(a)	Collar Reinforced Tee . . . . .	43
(b)	Crotch Reinforced Tee . . . . .	43
(c)	Wrapper Reinforced Tee . . . . .	43
6.6	All filters on reinforced pipes . . . . .	44
(a)	Collar Reinforced Tee . . . . .	44
(b)	Crotch Reinforced Tee . . . . .	44
(c)	Wrapper Reinforced Tee . . . . .	44
6.7	Structural filters on hauler truck model with single layer removal . . . . .	46
(a)	Open Edges Filter . . . . .	46
(b)	Sharp Edges Filter . . . . .	46
6.8	Strain filters on hauler truck model . . . . .	47

## LIST OF FIGURES

xiii

(a)	Minimum Filter . . . . .	47
(b)	Strain Gradient Filter . . . . .	47
7.1	An un-powered railway bogie with central pivoting and two side-bearers . . . . .	49
7.2	Typical forces experienced by a bogie with central pivoting . . . . .	50
7.3	Finite-element (FE) model used for numerical studies . . . . .	50
7.4	Test cases for investigating the effect of the number of design points . . . . .	51
(a)	Test Case 1 . . . . .	51
(b)	Test Case 2 . . . . .	51
(c)	Test Case 3 . . . . .	51
7.5	The effect of the number of design points (i.e. strain gauges) on the calculated RMS error of reconstructed loads with only distinct points in the proportionality matrix . . . . .	53
7.6	The effect of the number of design points (i.e. strain gauges) on the calculated RMS error of reconstructed loads with duplicate points in the proportionality matrix . . . . .	54
7.7	The effect of the number of design points in the proportionality matrix on the calculated RMS error . . . . .	55
7.8	Candidate set optimisation techniques . . . . .	56
(a)	Full Optimisation . . . . .	56
(b)	Partial Optimisation . . . . .	56
(c)	Double Optimisation . . . . .	56
7.9	Test cases for investigating the effect of various optimisation techniques . . . . .	57
(a)	Test Case 4 . . . . .	57
(b)	Test Case 5 . . . . .	57
(c)	Test Case 6 . . . . .	57
(d)	Test Case 7 . . . . .	57
(e)	Test Case 8 . . . . .	57
(f)	Test Case 9 . . . . .	57
7.10	Effect of various optimisation methods on the reconstruction of . . . . .	59
(a)	Test Case 4 . . . . .	59
(b)	Test Case 5 . . . . .	59
(c)	Test Case 6 . . . . .	59
7.11	Effect of various optimisation methods on the reconstruction of . . . . .	60
(a)	Test Case 7 . . . . .	60
(b)	Test Case 8 . . . . .	60
(c)	Test Case 9 . . . . .	60
8.1	Physical setup of multiple load reconstruction experiment . . . . .	61
8.2	Finite-element (FE) model of load reconstruction experiment . . . . .	62
8.3	Optimal candidate points for unfiltered Candidate Set 1 . . . . .	63

## LIST OF FIGURES

xiv

8.4	Assumed force magnitudes and Strain Gradient filter selections . . . . .	64
	(a) Load Case 1: Assumed Loads . . . . .	64
	(b) Load Case 1: 439 Elements . . . . .	64
	(c) Load Case 2: Assumed Loads . . . . .	64
	(d) Load Case 2: 269 Elements . . . . .	64
	(e) Load Case 3: Assumed Loads . . . . .	64
	(f) Load Case 3: 368 Elements . . . . .	64
8.5	Elements identified by analyst and structural filters . . . . .	65
8.6	Effect of various optimisation methods on . . . . .	66
	(a) Load Case 1 . . . . .	66
	(b) Load Case 2 . . . . .	66
	(c) Load Case 3 . . . . .	66
8.7	Optimal candidate points for Candidate Set 2 . . . . .	67
8.8	Actual placement of Gauge A relative to Element 1 729 . . . . .	68
8.9	Location of Gauge A in the FE model . . . . .	70
8.10	Location of Gauge D in the FE model . . . . .	70
8.11	Original candidate points in proportionality matrix . . . . .	71
8.12	Averaged candidate points in proportionality matrix . . . . .	71
8.13	Weighted averaged candidate points in proportionality matrix . . . . .	72
8.14	Location of Gauge A in the FE model with surrounding elements . . . . .	74
9.1	Final methodology for static load reconstruction . . . . .	79
A.1	Orientation of strain gauge with respect to a quadrilateral element and its elemental coordinate system . . . . .	82
A.2	Strain gauge position relative to the origin of a global coordinate system (GCSYS) or a reference node . . . . .	83
A.3	Rotation angles of vector $A$ relative to a global coordinate system . . . . .	84
A.4	Sample FE model to test mounting function . . . . .	85
B.1	Sample FE model used to test other outlier detection techniques . . . . .	87
B.2	Outliers detected based on <i>logarithmic transformation</i> and <i>standard</i> <i>boxplot</i> procedures . . . . .	88
B.3	Outliers detected based on <i>logarithmic transformation</i> and <i>adjusted</i> <i>boxplot</i> procedures . . . . .	88
B.4	Logarithmic transformed histogram of calculated strain gradients with standard boxplot parameters . . . . .	89
B.5	Logarithmic transformed histogram of calculated strain gradients with adjusted boxplot parameters . . . . .	90
C.1	Structural filters on reinforced pipes with double layer removal: . . . . .	92
	(a) Open Edges: Collar . . . . .	92

## LIST OF FIGURES

xv

(b)	Sharp Edges: Collar . . . . .	92
(c)	Open Edges: Crotch . . . . .	92
(d)	Sharp Edges: Crotch . . . . .	92
(e)	Open Edges: Wrapper . . . . .	92
(f)	Sharp Edges: Wrapper . . . . .	92
C.2	Structural filters on hauler truck model with double layer removal . . .	93
(a)	Open Edges Filter . . . . .	93
(b)	Sharp Edges Filter . . . . .	93
C.3	All filters on hauler truck model . . . . .	94
(a)	Wireframe View . . . . .	94
(b)	Elemental View . . . . .	94
D.1	Location of Gauge B in the FE model . . . . .	98
D.2	Location of Gauge C in the FE model . . . . .	98
D.3	Location of Gauge E in the FE model . . . . .	99
D.4	'Adapted' proportionality matrix for Load Case 1 . . . . .	102



# List of Tables

5.1	Results of Minimum Strain filter on a sample FE model . . . . .	26
5.2	Strain gradients identified by Barry (2017) . . . . .	27
5.3	Default argument values for developed pieces of software . . . . .	32
6.1	Incorrectly selected elements by Sharp Edges filter on pipe models . . . . .	38
6.2	Summary of elements removed by filters on real-life FE models . . . . .	48
8.1	Experimentally measured strain values . . . . .	69
8.2	Surface coverage of Gauge A . . . . .	70
8.3	Surface coverage of Gauge D . . . . .	70
8.4	Results of reconstructed loads for Load Case 1 . . . . .	72
8.5	Measured and calculated strain values for Load Case 1 . . . . .	73
8.6	Strain values of elements surrounding Gauge A for Load Case 1. . . . .	74
8.7	Results of reconstructed loads for Load Case 2 . . . . .	75
8.8	Measured strain values for Load Case 2 . . . . .	75
8.9	Results of reconstructed loads for Load Case 3 . . . . .	76
8.10	Measured strain values for Load Case 3 . . . . .	76
A.1	Results of mounting function. . . . .	86
D.1	Optimal design points of Candidate Set 1 . . . . .	96
D.2	Measured strain values at optimal design points for Load Case 1 . . . . .	97
D.3	Measured strain values at optimal design points for Load Case 2 . . . . .	97
D.4	Measured strain values at optimal design points for Load Case 3 . . . . .	98
D.5	Surface coverage of Gauge B . . . . .	98
D.6	Surface coverage of Gauge C . . . . .	98
D.7	Surface coverage of Gauge E . . . . .	99
D.8	Averaged candidate point corresponding to Gauge A . . . . .	99
D.9	Averaged candidate point corresponding to Gauge B . . . . .	99
D.10	Averaged candidate point corresponding to Gauge C . . . . .	100
D.11	Averaged candidate point corresponding to Gauge D . . . . .	100
D.12	Averaged candidate point corresponding to Gauge E . . . . .	100

*LIST OF TABLES***xvii**

D.13 Weighted averaged candidate point corresponding to Gauge A . . . . .	100
D.14 Weighted averaged candidate point corresponding to Gauge B . . . . .	101
D.15 Weighted averaged candidate point corresponding to Gauge C . . . . .	101
D.16 Weighted averaged candidate point corresponding to Gauge D . . . . .	101
D.17 Weighted averaged candidate point corresponding to Gauge E . . . . .	101
D.18 Strain values at elements surrounding Gauge C for Load Case 1. . . . .	102
D.19 Strain values at elements surrounding Gauge A for Load Case 2. . . . .	103
D.20 Strain values at elements surrounding Gauge C for Load Case 2. . . . .	103
D.21 Strain values at elements surrounding Gauge A for Load Case 3. . . . .	104
D.22 Strain values at elements surrounding Gauge B for Load Case 3. . . . .	104
D.23 Strain values at elements surrounding Gauge C for Load Case 3. . . . .	105
D.24 Strain values at elements surrounding Gauge E for Load Case 3. . . . .	105

# Chapter 1

## Introduction

### 1.1 Project Background

The Engineering Research Chair for the Passenger Rail Agency of South Africa (PRASA) at the Department of Industrial Engineering, Stellenbosch University, initiated a project that aimed to predict the durability of a Commonwealth bogie-frame of a class 5M train (Nickerson, 2017). A bogie-frame is a “load-bearing structure, generally located between [the] primary and secondary suspension” (BS EN 13749:2011). According to Nickerson, these trains, which have been in operation since 1958, have “poor levels of [life] predictability [...] due to decades of underinvestment.” Quantifying the durability of these bogie-frames is vital for future usage and “evaluating its current market value” (Nickerson, 2017). Transnet Engineering (TE), a subsidiary of Transnet SOC Ltd., which is responsible for the maintenance and manufacturing of rolling stock within South Africa, currently makes use of standards such as BS EN 13749:2011, to predict the strength of bogie-frames.

The durability of a structure depends on the inherent strength, characterised by its material behaviour and geometrical attributes, as well as the various applied forces (Johannesson and Speckert, 2014). These forces can often only be approximated; thus, engineers tend to design components with excessive safety factors that, in turn, lead to more significant production costs. TE’s Research and Development (R&D) department realised the importance of realistically representing the applied forces on any load-bearing structure, specifically bogie-frames, to predict its longevity. Any incorrect assumption could diminish its economic feasibility (Augustine *et al.*, 2016).

Mechanical forces are traditionally measured by placing a transducer (load cell) within the load path (Plaskitt, 2016), i.e. between the structure and load transferring body or mechanism, but these sensors have notable limitations. It has

the potential of changing the dynamic characteristic of the frame it is attached to, which can lead to inaccurate force estimations (Gupta, 2013). Also, the load paths are often inaccessible, and in some applications, loads are not directly measurable by transducers, such as fluid-flow induced forces (Gupta, 2013). Often the structure needs to be modified to accommodate load cells and not all desired degrees of freedom can be measured (Augustine *et al.*, 2016). Moreover, load cell technologies are expensive.

## 1.2 Project Scope and Objectives

This study aims to develop a methodology that determines the applied forces on any structure, without explicitly measuring these forces with a load cell, so that it can be used in future studies to determine the applied loading on a bogie-frame. Objectives are defined as follows:

- *Develop a software programme for numerical data processing and optimisation.* The programming tool must have two functions: process the structural response data of a finite-element (FE) model, in order to determine optimal sensor placement locations. Secondly, it should determine the relationship between the input force and structural response in order to back-calculate the imposed static forces using a linear least-squares estimate.
  - *Simulate a unit-load FE model of the structure.* The response of this model, which describes the relationship between the applied force and structural response, will be used as the input data set to the software programme mentioned above.
  - *Design an experiment in order to measure the actual response of the model.* Test results will be used, together with the second function of the software programme, to calculate the imposed forces on the structure. Concurrently, the exerted loads will be directly measured, to evaluate the accuracy of the calculated forces.
  - *Develop an auxiliary software programme for geometrical and sensitivity filtering purposes.* The intent is to exclude any data points from the numerical data set to prevent the measurement of incorrect responses. The incorrect measurement of the structural response can be due to both practical and numerical constraints.
-

# Chapter 2

## Literature Review

This study aims to develop a methodology that determines the applied forces on any structure, without explicitly measuring these forces with a load cell, so that in future studies it can be used to calculate the loads applied to a bogie-frame. Two overarching approaches exist for estimating loads. *Load reconstruction* makes use of the structural response to back-calculate the applied loading, i.e. working from the effect to the cause. A *multi-body system* (MBS) simulation involves deconstructing a vehicle system into an interconnected dynamic (mass-spring-damper) model. The road or rail path can be simulated to define the input loading, and, together with the dynamic model, the loads on the specific structure of interest can be calculated.

Transnet Engineering currently uses the British Standard (BS) EN 13749 to validate the mechanical strength of a bogie-frame. It requires performing an analysis, laboratory static and fatigue tests, and track tests. Commonly, a bogie that passes the laboratory fatigue test will not be subject to track testing. Real vehicle structures experience complex loading conditions that include combinations of both time-independent (static) and time-dependent (dynamic and quasi-static) loads. However, the laboratory tests detailed in EN 13749 utilise equivalent static and quasi-static loading conditions, as opposed to the real dynamic load cases. Thus, this study will also confine its scope to static and quasi-static loads. Quasi-static loads are time-dependent, but the effect of inertia can be neglected (Gupta, 2013).

### 2.1 Load Reconstruction

Load reconstruction involves the transformation of an ordinary structure into a force transducer where the magnitude of the applied loads can be determined with an FE model and the measured structural response (Wannenburg and Heyns, 2010). This technique is suitable for static, quasi-static and dynamic loading conditions (Gupta, 2013).

There are various advantages to using this technique: first of all, the sensors used to measure the structural response are inexpensive relative to load cells; thus it is a cost-effective method to determine loads without affecting the load path (Hunter, 2018). It was made clear by Maas (2015) that it is also beneficial for determining in-service loads when the technique was used on a mountain bicycle to determine the operational loads during extreme jumps. It is computationally efficient, since it only needs unit-load static FE solutions for creating the strain-load transfer matrix (Wannenburg and Heyns, 2010). However, it is required that a prototype or similar vehicle already exists and that direct measurement of the structural response is possible (Wannenburg and Heyns, 2010). Furthermore, the strain-load transfer matrix is historically ill-conditioned, but Gupta (2013) proposed the use of an exchange algorithm, and model order reduction for the dynamic load cases, to improve the condition or sensitivity of this matrix.

Commercial software products such as True-Load<sup>TM</sup> by Wolf Star Technologies (2017) and nCode (2020) by HBM Prenscia both use load reconstruction. Extensive research was performed by Gupta (2013) on various techniques used to reconstruct static, quasi-static and dynamic loads. Other researchers, from the same institution, studied the identification of dynamic moving loads (Augustine, 2015), distributed loads (Kobiske, 2015), impact loads (Chembakassery, 2018) and transient loads (Wagle, 2018). Load reconstruction has also been used by Xiaofeng *et al.* (n.d.), Slowinski (2017), Augustine *et al.* (2016), Maas (2015) and Murphy and Tanner (2015) at various stages during product development.

## 2.2 Multi-body System (MBS) Simulation

A mechanical system is decomposed into different rigid bodies with a mass and inertia tensor which are connected by idealised constraints or force elements. These connections describe the relative motion between the respective bodies. External forces are loads applied from the outside onto the system - for example, the loads imposed on the wheels of a rail-carriage system from the railroad. This set of rigid bodies, connections and external loads define the motion and reaction forces of the system. Ultimately, a dynamic model can be constructed and used to determine the forces between the interconnected components, such as the suspension loads on a bogie-frame.

This technique is useful if direct measurements are not feasible (Wannenburg and Heyns, 2010), since no existing prototype or similar vehicle is needed. A description of the road profile is required, but it can be simulated from known statistical or geometric information (Wannenburg, 2007, p.33). The rigid-body assumption is not always valid for bodies such as tyres or springs, but the technique can include the modelling of flexible bodies using the FE method (Johannesson and Speckert, 2014). According to Johannesson and Speckert (2014), a Multi-Body System (MBS) approach is most commonly used to calculate quasi-static and dy-

dynamic forces on a vehicle structure, in order to perform fatigue analyses. However, using MBS for estimating static loads is meaningless, since the dynamic model reduces to a static equilibrium problem where the unknowns can be calculated by solving the equilibrium equations.

Dietz *et al.* (1998) used MBS to predict the fatigue life of a railway bogie. A freight locomotive had been modelled with SIMPACK MBS software as well as the complete wheel-rail system. Then, the calculated dynamic loads were used in the MBS-post-processor, FEMBS<sup>-1</sup>, to transfer these loads to an FE-model for calculating the stress distribution. Stichel and Knothe (1998) calculated the interaction forces on a railway bogie from measured track irregularities to predict its fatigue life. Luo *et al.* (1994) used a similar methodology to Stichel and Knothe (1998), to develop a dynamic model of the vehicle using a software package developed by British Rail, called VAMPIRE. Nickerson (2017) also used MBS to perform a fatigue analysis on a Commonwealth bogie-frame.

## 2.3 Comparison of Methodologies

The objective of this study is to develop a methodology that determines the applied forces on a structure without explicitly measuring these forces with a load cell; the techniques associated with the two identified approaches are compared in the subsequent text. It should be noted that the scope of this study is limited to static and quasi-static loading conditions.

Load reconstruction is suitable for determining static, quasi-static and dynamic loading conditions, whereas MBS is not commonly associated with static loading problems. MBS considers the entire vehicle transportation structure and the road path, which makes this method computationally taxing. However, no existing structure or prototype is required. Load reconstruction allows for in-service testing, and Commonwealth bogie-frames are already in operation. Furthermore, since it only requires linear static unit-load FE solutions for creating the strain-load transfer matrix, load reconstruction is computationally more efficient than MBS.

## 2.4 Conclusion

Two methodologies for estimating the applied loads on a bogie-frame were identified and compared in this chapter. This information, together with the project background, concluded that the load reconstruction technique would be further investigated. The succeeding chapter will elaborate on the theoretical fundamentals of load reconstruction.

## Chapter 3

# Static Load Reconstruction

### 3.1 Load Transducer Principle

The load reconstruction methodology depends on the behaviour of the imposed loads as a function of time. Quasi-static forces are loads for which the effect of inertia is neglected; thus, the principles for load reconstruction is similar to that of static loads. Figure 3.1 will be used to explain the concept of transforming a structure into its own load transducer, which forms the basis of static load reconstruction. The fixed cantilever beam, with an axial force and bending moment applied at its free end, has two strain gauges respectively mounted at the top and bottom to measure the structural response.

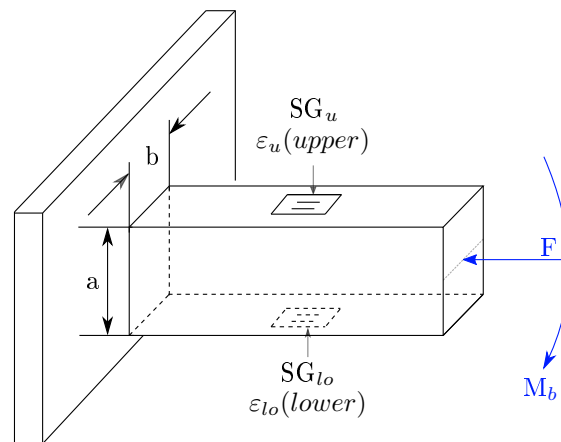


Figure 3.1: Fixed cantilever beam with an axial and bending moment applied at its free end. This schematic will be used to illustrate the concept of transforming a structure into its own load transducer.

For a linear elastic material, the gauge response to each load, i.e. the relationship between the axial force, bending moment and output strains at the upper and lower surface, can be obtained from the stress-strain equations:



$$\begin{aligned}
\varepsilon_{u,F} &= -\frac{1}{E} \frac{F}{ab} & \varepsilon_{lo,F} &= -\frac{1}{E} \frac{F}{ab} \\
\varepsilon_{u,M_b} &= \frac{1}{E} \frac{M_b \frac{a}{2}}{\frac{1}{12} a^3 b} & \varepsilon_{lo,M_b} &= -\frac{1}{E} \frac{M_b \frac{a}{2}}{\frac{1}{12} a^3 b} \\
&= \frac{1}{6} \frac{M_b}{a^2 b E} & &= -\frac{1}{6} \frac{M_b}{a^2 b E}
\end{aligned} \tag{3.1}$$

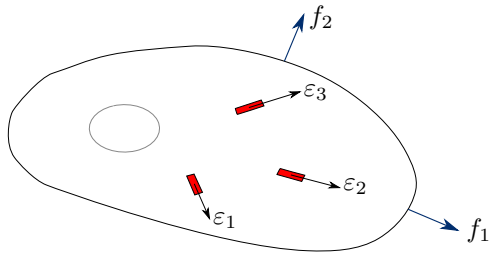
These equations can be superimposed to give:

$$\varepsilon_u = -\frac{F}{abE} + \frac{1}{6} \frac{M_b}{a^2 b E} \quad \varepsilon_{lo} = -\frac{F}{abE} - \frac{1}{6} \frac{M_b}{a^2 b E} \tag{3.2}$$

which can be rewritten as a system of linear equations:

$$\begin{Bmatrix} \varepsilon_u \\ \varepsilon_{lo} \end{Bmatrix} = \begin{bmatrix} -\frac{1}{abE} & \frac{1}{6} \frac{1}{a^2 b E} \\ -\frac{1}{abE} & -\frac{1}{6} \frac{1}{a^2 b E} \end{bmatrix} \begin{Bmatrix} F \\ M_b \end{Bmatrix} \tag{3.3}$$

The total strain value measured by the top (or bottom) strain gauge will be equal to the superimposed strain responses respectively caused by the axial force and bending moment. Thus, for any arbitrary structure, such as the one in Figure 3.2, the strain gauge measurements will equal:



$$\begin{aligned}
\varepsilon_1 &= c_{11} f_1 + c_{12} f_2 \\
\varepsilon_2 &= c_{21} f_1 + c_{22} f_2 \\
\varepsilon_3 &= c_{31} f_1 + c_{32} f_2 \\
&\Downarrow
\end{aligned} \tag{3.4}$$

Figure 3.2: Arbitrary structure to illustrate the concept of superposition

$$\begin{Bmatrix} \varepsilon_1 \\ \varepsilon_2 \\ \varepsilon_3 \end{Bmatrix} = \begin{bmatrix} c_{11} & c_{12} \\ c_{21} & c_{22} \\ c_{31} & c_{32} \end{bmatrix} \begin{Bmatrix} f_1 \\ f_2 \end{Bmatrix}$$

where  $c_{ij}$  is sensitivity of strain gauge  $i$  to load  $j$ . It is concluded that if the structural response is linear and the deformations are small enough for superposition to hold, the relationship between the input loading and output surface strain response can be written as:

$$\boldsymbol{\varepsilon} = \mathbf{C}\mathbf{f} \quad (3.5)$$

$\boldsymbol{\varepsilon}$  is a  $(m \times 1)$  vector of measured strains at  $m$  distinct locations and orientations,  $\mathbf{C}$  is a  $(m \times n)$  proportionality matrix where  $m \geq n$ , and  $\mathbf{f}$  is a  $(n \times 1)$  vector, known as the load vector, of  $n$  applied forces on the structure (Gupta, 2013, p.32). If the proportionality matrix is constructed from a unit-load FE model and the strain vector is measured through physical testing, the applied force vector can be calculated with a least-squares estimate:

$$\mathbf{f} = [\mathbf{C}^T\mathbf{C}]^{-1}\mathbf{C}^T\boldsymbol{\varepsilon} \quad (3.6)$$

This  $\mathbf{C}^T\mathbf{C}$  matrix is known as the variance-covariance matrix, alternatively referred to as the information matrix.

## 3.2 Proportionality Matrix

It has been shown in the preceding section how static loads can be reconstructed if the measured strain values and the relationship between the input load and output strains, also known as the proportionality matrix, are known. However, the conundrum is deciding where the analyst should measure these strain values, since it will also dictate the content of the proportionality matrix. The subsequent text will explain how the strain-load relationship in a numerical environment is used to determine the proportionality matrix, which ultimately dictates gauge mounting locations and orientations in an experimental environment.

### 3.2.1 Candidate Set

Certain key aspects of the linear equation should be defined first; thus, Equation 3.5 is expanded into its matrix form in Figure 3.3. The *force vector* ( $\mathbf{f}$ ) is a one-dimensional array where each element in the vector represents an imposed force. For instance, if two loads are applied to the structure, there will be two elements in the load vector (see Equations 3.3 and 3.4). The problem of interest is not necessarily identifying *where* forces are imposed on a structure, but instead its magnitudes. Thus, for load reconstruction purposes, the analyst should discreetly

choose which loads to include in the force vector. Maas (2015), for example, assumed an initial set of loads that were subsequently reduced. If a force is not included in the FE model, but acts on the physical structure, the estimated load results will be corrupt; this is also true if too many loads are assumed.

Each finite-element on the surface of the FE model represents a potential location at which a strain gauge can be mounted; thus, it can be viewed as a simulated representation of gauges in a numerical environment. If load  $f_j$  is the only load in the force vector with a magnitude of unity, and the rest of the components equal zero, the  $j^{\text{th}}$  column in the strain-load relationship model will be equal to the strain field over the entire FE model. This idea of sequentially activating loads with a magnitude of unity is used to construct the respective columns in this strain-load relationship model which is also known as the candidate set.

Strain gauges only record measurements in its axial direction, but can be glued onto a surface at different orientations to measure strain in various global directions. The candidate set must be extended to also include strain measurements in directions other than its axial direction. Henceforth, each row in the candidate set is a specific combination of gauge location and orientation known as a **candidate point**. Conclusively, if the superposition assumption remains true, the response of a strain gauge at location and orientation  $i$ , equals:

$$\varepsilon_i = c_{i1}f_1 + c_{i2}f_2 + \cdots + c_{ij}f_j + \cdots + c_{in}f_n \quad (3.7)$$

where  $c_{ij}$  is the sensitivity of gauge  $i$  to load  $j$ , similar as in Equation 3.4. Equation 3.7 is a linear regression model which describes the relationship between dependent (strain) and independent (applied force) variables.

### 3.2.2 Design Matrix

It is impossible to mount strain gauges at every possible candidate point, therefore, it is required to identify how many gauges should be mounted where, and at what orientation. Also, the composition of the proportionality matrix is directly dependent on these selected candidate points.

Heath (2002) stated that inverse problems, like the load reconstruction problem, is historically ill-conditioned, which means it is sensitive to round-off errors and small changes in the input data. According to Gupta (2013), previous researchers chose gauge locations that will decrease this sensitivity by improving the condition of the proportionality matrix. Masroor and Zachary (1991) defined a sensitivity parameter, which was directly proportional to the variance of the force estimates, and selected various mounting locations and orientations, based on their judgment, to reduce this variance. It was not practical to consider all pos-



sible combinations; thus, there was no guarantee that the global optimum set of gauge location-orientation combinations were chosen. Wickham *et al.* (1995), however, saw the selection of gauges as an optimisation problem and used an exchange algorithm to construct a D-optimal design.

Optimal designs are experimental designs that are optimal for some statistical criterion (Trutna *et al.*, 2013). The various forms of optimality criteria for a design matrix include A-optimality, G-optimality, V-optimality and D-optimality and are often referred to as alphabetic optimality criteria (Myers *et al.*, 2009). D-optimality tries to maximise the determinant of the information matrix of the design matrix (Trutna *et al.*, 2013) which, in succession, minimises the variances of the model regression coefficients of a pre-established model (Myers *et al.*, 2009; Trutna *et al.*, 2013). According to Erikson (2017), the D-optimal design will choose a subset that spans the maximum volume possible from the candidate set, which will maximise the determinant of the information matrix. It is required that the experimenter decide on the model of the design (e.g. a linear or second-order response surface model) as well as specify the desired number of design points in the design matrix. These design points are selected from a candidate set that contains all the experiments that can possibly exist (Trutna *et al.*, 2013).

The load reconstruction problem (Equation 3.7) is a linear model, and the candidate set consist of all the gauge location-orientation combinations. The methodology for creating this particular candidate set was explained in Section 3.2.1. The D-optimal subset of candidate points, is known as the design matrix where the rows correspond to optimal strain gauge locations and orientations. It is this ( $m \times n$ ) subset that is also known as the proportionality matrix.

Gupta (2013) suggested the use of a sequential or  $k$ -exchange algorithm to find a D-optimal design. He also noted that using D-optimality was efficient and famous, but that it can get stuck in a local optimum. Federov's Exchange Algorithm for D-optimal Design is open-source software that can be used to find the design (or proportionality) matrix. The algorithm was originally written in Fortran 77, but wrapper functions make it usable in modern programming languages. There are two shortfalls of the algorithm: it does not attempt to force different points, i.e. the same candidate point may be chosen several times and, occasionally, it fails to find a full-rank starting design (Miller and Nguyen, 1994). Federov's Exchange Algorithm uses Banachiewicz factorisation to calculate the determinant of the information matrix:

$$\mathbf{C}^T \mathbf{C} = \mathbf{R}^T \mathbf{D} \mathbf{R} \quad (3.8)$$

where  $\mathbf{R}$  is an upper triangular matrix and  $\mathbf{D}$  is a diagonal matrix. The determinant is equal to the product of the elements on the diagonal of  $\mathbf{D}$  (Miller and

Nguyen, 1994, pg. 670). According to Miller and Nguyen (1994), this method for computing determinants is not used in other D-optimal designs. The stages of the algorithm, as set out by Miller and Nguyen (1994), is:

1. Half of the points of the initial design are randomly selected. Sequentially points are added to fill the open design points by maximising the rank and determinant for this subspace.
2. The rank of the initial design is checked. If the rank is deficient, a candidate point is selected that will increase the rank. A design point in the current design, which can be removed without reducing the rank, is exchanged with a selected candidate point. The process is repeated until the rank is equal to  $n$  or cannot be further increased.
3. All points in the current design are considered for the exchange with any of the available candidate points. The pair that will maximise the increase in the determinant will be chosen for the exchange. This stage is repeated until no further increase is obtained.

The RSTART parameter is set to TRUE; thus, a random start point (or initial design) is created each time the algorithm runs. This procedure is repeated a user-prescribed number of times (default of 1000 runs) in hopes of finding a global, and not a local, optimum from a random starting point (Miller and Nguyen, 1994, pg. 671). A global optimum, however, is still not guaranteed.

### 3.3 Summary

In Figure 3.4 the general methodology for reconstructing static loads is outlined. The linear static FE solutions for individual unit-loads in the force vector are used to construct the candidate set. This set describes the linear relationship between the input loads and output strains for a limitless number of gauge location-orientation combinations (or candidate points). The component  $c_{ij}$  in the candidate set correspond to the strain at candidate point  $i$  due to an active unit-load at  $j$  in the load vector. A subset of candidate points, known as the design (or proportionality) matrix, are selected from this candidate set with a D-optimality design. The process entails selecting candidate points with an exchange algorithm that will maximise the determinant of the information matrix of the design matrix. Incidentally, this matrix also dictates the gauge mounting locations and orientations. The proportionality matrix and measured strain values can be utilised to estimate the applied loads with a least-squares estimation.

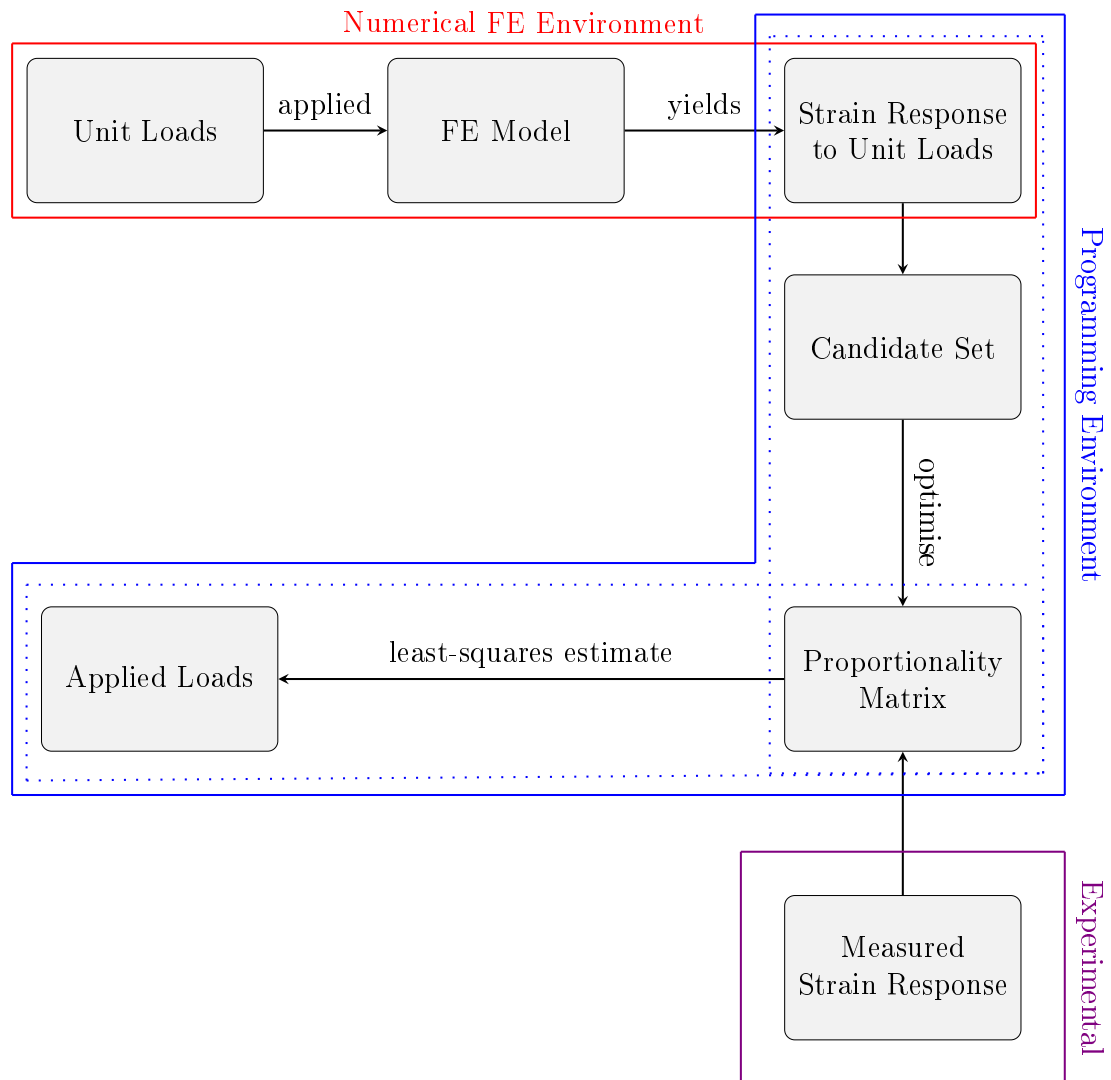


Figure 3.4: Methodology for static load reconstruction which includes constructing a strain-load transfer candidate set from a unit-load FE model. This set is then condensed to a matrix, using an optimisation algorithm, which is used together with experimental measurements to inversely calculate the applied loads.

## Chapter 4

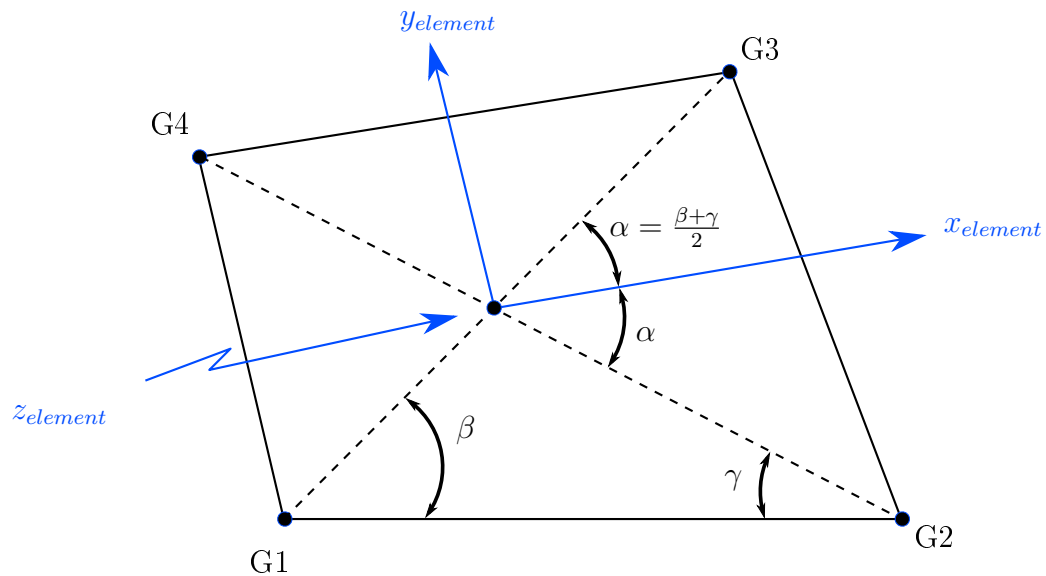
# Finite-element (FE) Model Preparations

The previous chapter described how the FE model is the link between the applied load vector and the measured strains. A well-prepared FE model is thus of paramount importance, since it is also utilised to determine where strain gauges should be mounted. This chapter will elaborate on the preparations that need to be made within an FE environment to ensure compatibility with the Proportionality or Design Matrix software (Section 5.2) and, ultimately, the testing environment. Nastran is the default FE solver used for this project.

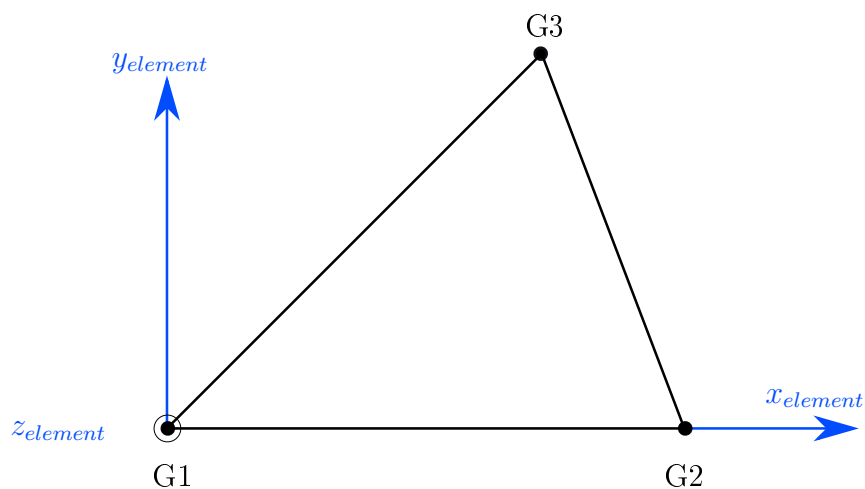
### 4.1 Two-dimensional (2D) Elements in Nastran

The load reconstruction software is only compatible with two-dimensional (2D) elements; thus, it is necessary to understand the geometry and associated elemental coordinate systems (ECSYS) of the 2D elements frequently used in Nastran. CQUAD4 (Figure 4.1a) is a four-node quadrilateral element and the most popular, followed by CTRIA3 (Figure 4.1b) that is a three-node triangular element. The orientation of the ECSYS is defined by the grid points order where the  $z$  axis, or positive normal, is determined using the right-hand rule (Siemens, 2014a). Quadrilateral elements are often preferred for accuracy reasons, and triangular elements are mostly used for “mesh transitions” or areas on the structure “when quadrilateral elements are impractical” (Siemens, 2014a, pg. 4-13). FE models that primarily consist of three-dimensional (3D) elements can be coated with 2D elements. In the remainder of this section, all statements will apply to both quadrilateral and triangular elements unless otherwise stated. However, when a decision needs to be made, the choice will be partial to CQUAD4 elements.





(a) CQUAD4 elements



(b) CTRIA3 elements

Figure 4.1: Element geometry and coordinate systems of the most commonly used two dimensional (2D) elements in Nastran (Siemens, 2014a, pg. 4-15,16).  $G_i$  indicates the respective grid points.

## 4.2 Strain Gauge Considerations

Strain gauges can only measure strain at the surface of a structure; thus, the necessary preparations must be carried out for the FE model to calculate strain values at the structural surface. Structures of three-dimensional (3D) nature, such as an engine or cast bogie-frame, can often only be modelled with solid elements. These elements can exclusively output stress and strain values at centroids and Gauss points, which are extrapolated to grid points (Siemens, 2014a, pg. 5-4). However, it does not calculate strain values at the structural surface. One could argue that the analyst can average the grid point outputs that shape the face of the element tangent to the surface of the structure, but averaging after extrapolation induces unwanted errors. Besides, there is no way of knowing which face of the solid element is tangent to the surface without a graphical user interface (GUI). The areas of interest for strain gauge measurements that consist of solid elements should consequently be coated with a layer of 2D elements. Xiaofeng *et al.* (n.d.) agreed that coating gives a more accurate surface output. Experience has taught that the same material characteristics may be used for the coated elements, but that an almost zero element thickness must be assigned not to change the stiffness characteristics of the structure. The validation procedure involves comparing displacements at grid points before and after surface coating; if there is no significant difference in the calculated displacements, the surface coat is adequately applied.

Strain can either be output at the reference plane and curvatures (STRCUR) or fiber distances (FIBER) (Siemens, 2014a, pg. 4-27). The FIBER command (see Figure 4.4) allows the analyst to specify at which positions, through the thickness of the 2D element, the strain output is desired. If the fiber distances (Z1, Z2) are not specified, Nastran will assume that Z1 corresponds to the bottom and Z2 to the top of the element based on the normal vector. The load reconstruction software developed here will only consider strain values for the candidate set at fiber distances greater than zero ( $Z > 0$ ), i.e. at the top of the element surface. To ensure compatibility with the Proportionality (or Design) Matrix software, the analyst should review element normals and fiber locations (Figure 4.2) in the FE environment, especially if an offset was used to define the element thickness.

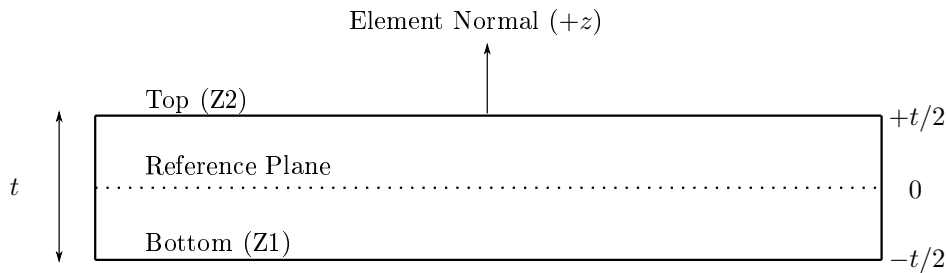


Figure 4.2: Cross-section of a two-dimensional (2D) element to explain the FIBER command in Nastran. This schematic assumes that an offset was not used when the element thickness was defined.

Strain for all elements is recovered at the “element centre, and Gauss points using the elemental strain matrix and the computed grid point displacements” (Siemens, 2014a, pg. 4-28). CQUAD4 elements have the option to extrapolate these computed values to grid points, using various methods (BILINEAR, CUBIC and SGAGE) (Siemens, 2014a, pg. 4-29). It was decided that a strain gauge should be attached at the centroid of an element; thus the strain results should be requested using the CENTER command in Nastran’s input file (see Figure 4.4).

Strain gauges can only measure strain in its axial direction, and since 2D elements are effectively computerised gauges, the elemental  $x$  direction will be chosen as the simulated axial direction. It was mentioned in Section 3.2.1 that strain gauges can be rotated on the surface of a structure to measure strain in various global directions, where each different orientation corresponds to another candidate point. Nastran’s output file only provides strain tensors that reference the elemental coordinate system (ECSYS); thus, the ECSYS will be used to rotate the computerised strain gauge in-plane about the elemental normal to calculate the strain output at various orientations.

### 4.3 Mesh Size Considerations

The discretisation of a structure into elements, also known as meshing, forms the core of any FE analysis. Mesh refinement is an iterative method that refines the mesh in order to increase the accuracy of the computed solution; thus, it is an essential operation in an FE analysis. Xiaofeng *et al.* (n.d.) highlighted that the most significant source of error between the calculated and actual loads originates from the differences between the FE and actual model. It was understood that the mesh size used by previous researchers in load reconstruction was dictated by the dimensions of the strain gauges used during testing (Gupta, 2013; Dhingra *et al.*,

2013). For this research, it was reasoned that a mesh refinement is critical and that it should determine the mesh size as opposed to the dimensions of gauges. If the mesh refinement produces an exceptionally fine mesh, the gauge will be mounted over several finite-elements and will effectively measure an average strain over the finite-elements covered by its grid length. This phenomenon will have a direct effect on the choice of elements that are to be included in the proportionality matrix, but this concern is investigated in Chapter 8.

## 4.4 Geometrical Considerations

The type of structure not only prescribes the element type that should be used (e.g. plate or solid elements), but its inherent shape could also hinder the attachment of gauges. It is occasionally not feasible to mount gauges in specific locations, such as near load application areas, at an edge, between two flushed components or other inaccessible areas specific to the structure. The elements that comprise these areas should be excluded from the group of elements submitted for computation within the pre-processor. Consequently, the calculated strain values associated with these elements will automatically be excluded from Nastran's results file and not be considered for the candidate set. Analysts and technicians often know from experience which regions to exclude, but manually selecting elements can become tedious and time-consuming, irrespective of how advanced the pre-processor is. A variety of filters were designed to automate the operation of selecting elements in the FE model, based on its location. Details of these structural filters can be found in Section 5.1. The filters do not account for all existing scenarios; thus it is inevitably still required from the analyst to review the filter selection and exclude any additional elements from the group submitted for computation, within the pre-processor.

The coordinates of the grid points in Nastran's input file could reference any random global coordinate system (GCSYS) if the FE model is incorrectly defined (see Section A.1 for more information on the different types of global coordinate systems in Nastran). Secondly, the angle of orientation used in the candidate set references the ECSYS of the corresponding shell element. An auxiliary function was thus designed to assist technicians with measuring out the mounting points of gauges. It transforms element location and orientation information to reference a specific GCSYS provided that it is predefined in the FE environment and its label (or ID) is known. The details of this software can be found in Appendix A.

## 4.5 Software Specific Considerations

Reference has been made to how the FE model should be set up to ensure compatibility with the developed Proportionality (or Design) Matrix software, but in addition to the requirements as mentioned earlier, it should also comply with the following criteria. The example in Figure 4.3 has three distinct loads imposed on the structure; i.e. the load vector has three components. The order of these loads in the vector is irrelevant, but will dictate the order of the columns in the candidate set. The strain response to each load, with an assigned magnitude of one (i.e.  $F_A = F_B = F_C = 1$ ), should respectively be computed as explained in Section 3.2.1. Thus, to ensure compatibility with the software, each unit-magnitude load component should be allocated to a subcase. The SUBCASE command is typically used in Nastran to “efficiently analyse multiple load cases in a single analysis” (Siemens, 2014b, pg. 8-2), where each subcase represents a separate, static loading condition. Subcases are defined in the Case Control Section of Nastran’s input file, of which an extract is provided in Figure 4.4. Requests above the first subcase (indicated by A) apply to all subcases, while requests within a subcase (indicated by B) are limited to only that subcase. The load reconstruction software only accepts OP2 output files; thus the Output Medium within the STRAIN requests command in Nastran’s input file (Figure 4.4) should be set to PLOT so that the results are reported in an OP2 file.

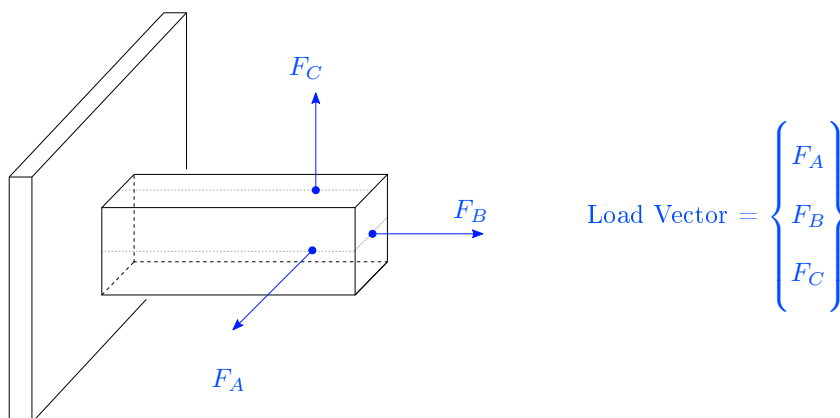


Figure 4.3: Three-load cantilever beam example used to explain the sequential activation of unit-loads for compatibility with Proportionality (or Design) Matrix software in Section 5.2.



# Chapter 5

## Software Development

It is required to process the FE model data in order to compile the proportionality matrix and determine the strain gauge mounting locations and orientations. This chapter will elaborate on the various pieces of software that were developed; the first algorithm identifies which finite-elements to exclude from the candidate set based on structural or strain-related criteria (Section 5.1), and the second algorithm compiles, extends and optimises the candidate set to a proportionality matrix that ultimately dictates gauge mounting locations and orientations (Section 5.2). pyNastran (Doyle, 2019), an open-source Python-based software interface for Nastran's input and output files, was extensively used. It has a BDF interface, that can read, edit and write Nastran input data, and an OP2 interface to read large, binary results files.

### 5.1 Filtering Software

It was found during trial tests that the optimisation algorithm chose candidate points for the D-optimal design, where it was not necessarily practical to mount strain gauges. Many of these areas can be manually removed from the solution set submitted for computation within the FE pre-processor, which will automatically exclude these finite-elements from Nastran's results file. Consequently, these elements will also not be considered in the candidate set. However, for complicated structures, the manual selection process can become tedious and time-consuming. Several filters were developed in Python to identify specific finite-elements that should not be considered as candidate points. The reasons for wanting to exclude these elements are not limited to load reconstruction, and thus these filters are also applicable to other strain gauge operations. The FE model in Figure 5.1 will be used as a reference in the subsequent text to illustrate the typical difficulties encountered when mounting strain gauges. The average element size equals 5 mm and no mesh refinement was performed.

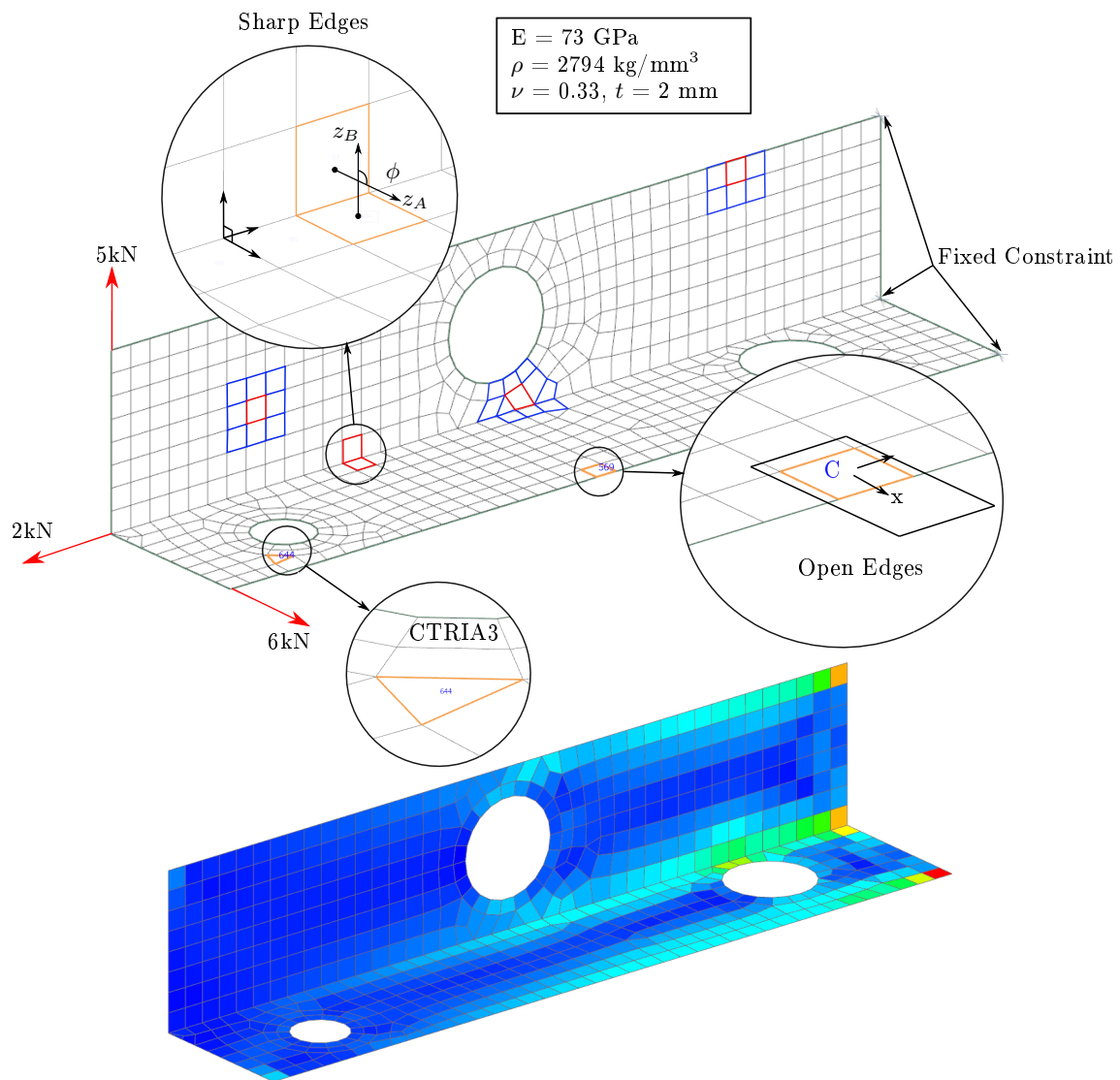


Figure 5.1: The sample FE model used to test the performance of filtering software. The strain response to the loads as indicated is also provided as reference for the strain-related filters.



The FE model had to be translated into an appropriate format for a programming environment first. Graphs were considered suitable objects, because these data-structures consist of vertices that are linked by edges (Hagberg *et al.*, 2019), which meant the interaction between vertices could conveniently be added to the metadata of the connecting edges. Each finite-element corresponds to a vertex within the graph; if two finite-elements share at least one grid point within the FE model, they are considered neighbours and an edge will be created between the two corresponding vertices. The metadata of vertices and edges are summarised in Figure 5.2, and each parameter will be defined throughout the subsequent text.

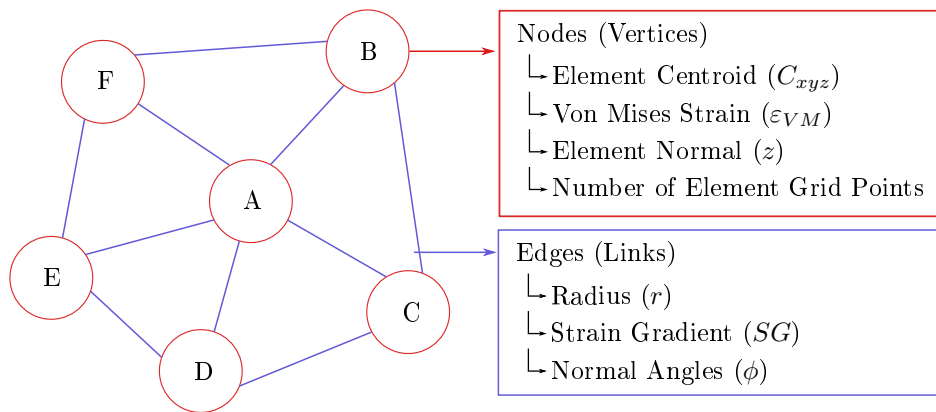


Figure 5.2: Unidirectional graph representing an FE model in a programming environment with the associated metadata for vertices and edges.

### 5.1.1 Sharp Edges Filter

It was challenging to place gauges at sharp or tight corners and to remove the installation tape subsequently; thus finite-elements that create sharp edges should not be considered as candidate points. A sharp edge is identified by investigating the element normals of neighbours; for example, in Figure 5.1 it is observed that the angle between normals is not parallel but instead within the range  $0^\circ < \phi < 180^\circ$ .

The elemental  $z$ -axes, or normals, can be calculated by taking the cross-product of intersecting vectors in the plane of the element (see Figure 4.1). Then, the angle between the normals of neighbouring finite-elements A and B in Figure 5.1, is:

$$\phi_{AB} = \cos^{-1} \left( \frac{\mathbf{z}_A \cdot \mathbf{z}_B}{\|\mathbf{z}_A\| \|\mathbf{z}_B\|} \right) \quad (5.1)$$

which is assigned to the graph edge that connects vertices A and B. For this particular example, all vertices linked by an edge where the normal angle is within the range  $85^\circ < \phi < 95^\circ$ , were added to the subset of elements that should be removed from the candidate set. The analyst needs to specify this range as an argument to the Sharp Edges filter.

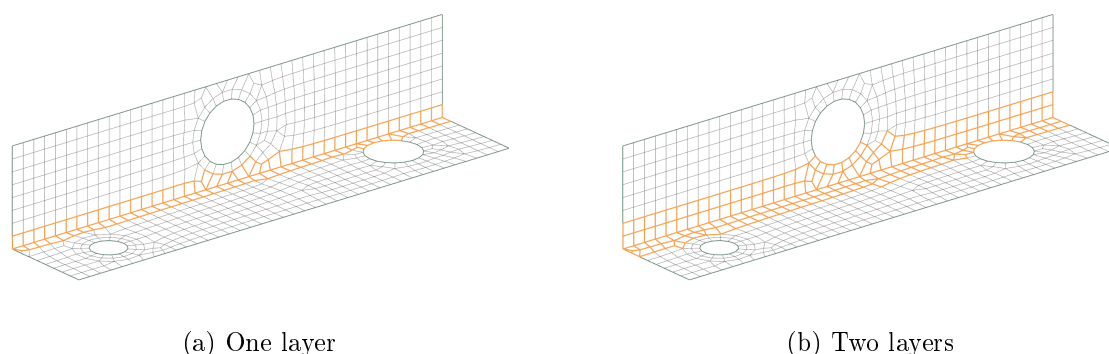


Figure 5.3: Results of the Sharp Edges filter on a sample FE model. In (a) only one layer of elements was removed and in (b) two layers of elements were removed from the sharp edge.

### 5.1.2 Open Edges Filter

It was not easy to mount gauges at open edges during trial tests, because the rough-textured surface finish typically found at edges, hindered the placement of sensors. Also, if a gauge needs to be mounted at the centre of Element C in Figure 5.1 at an orientation aligned with the elemental  $x$  axis, for example, the gauge will physically not fit. Simply moving the gauge inward is not an appropriate solution, particularly if a high strain gradient exists within that area. The high strain gradient phenomenon is detailed in Section 5.1.5.

A quadrilateral element at an open edge typically has five or less neighbouring elements; however, if the element is warped, it can have more (see Figure 5.1). This filter identifies all vertices with five or less neighbours and adds the associated finite-elements to a subset that should be removed from the candidate set. However, for this specific example where no mesh refinement was performed, finite-elements with six or fewer neighbours were added to the subset. `nNeighbours` is an argument to the Open Edges filter (default value of 5) that can be adapted by the analyst. In Figure 5.4a it is seen that the filter failed to select the encircled element because it has seven neighbours, but it was accounted for when a second surrounding layer was selected in Figure 5.4b. It is important that the analyst reviews the filter selections.

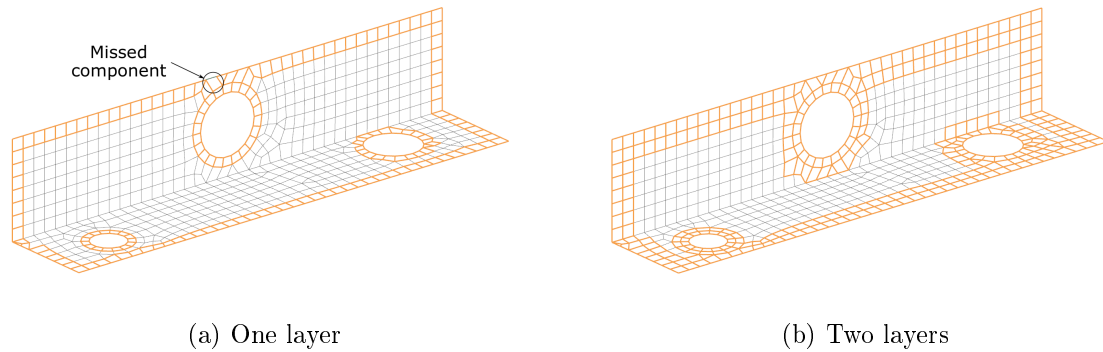


Figure 5.4: Results of the Open Edges filter on a sample FE model. In (a) only one layer of elements was removed and in (b) two layers of elements were removed surrounding the open edge.

### 5.1.3 Triangular Element Filter

Quadrilateral elements are preferred for reasons provided in Section 4.1; thus, triangular elements should not be included in the candidate set. However, if the structure is modelled with 3D tetrahedral elements, triangular elements will automatically be used for the surface coat (see Section 4.2); thus, for that particular situation, triangular elements should not be excluded from the candidate set. The results for Figure 5.1 are shown in Figure 5.5:

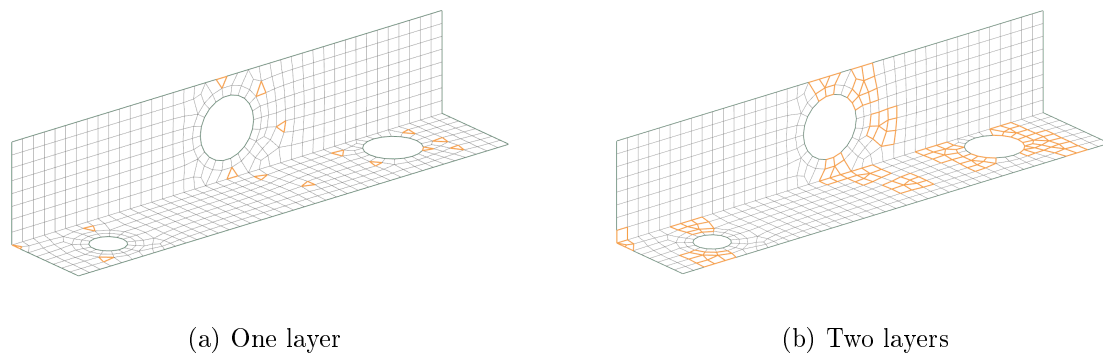


Figure 5.5: Results of the Triangular Element filter on a sample FE model. In (a) only one layer of surrounding elements was removed and in (b) two layers of surrounding elements were removed from the triangular element.

### 5.1.4 Minimum Strains Filter

In a load reconstruction pilot test, candidate points which corresponded to locations where the strain response was too small to be accurately measured by a strain gauge, were selected. The D-optimal design will inevitably pick finite-elements with small strains, since it chooses a subset of candidate points that span the largest volume possible from the entire candidate set, without taking the actual strain values into account (Erikson, 2017). The strain response, however, is dependent on the input loading; thus, the output file of an FE model that estimates the load magnitudes are required in order for this filter to work. The loads are indicated in Figure 5.1 and the elements, where  $\varepsilon_{VM} \leq 10^{-3}$  mm/mm, are shown in Figure 5.6. This threshold will be different for various experiments and depends on the minimum measuring ability of the strain gauge.

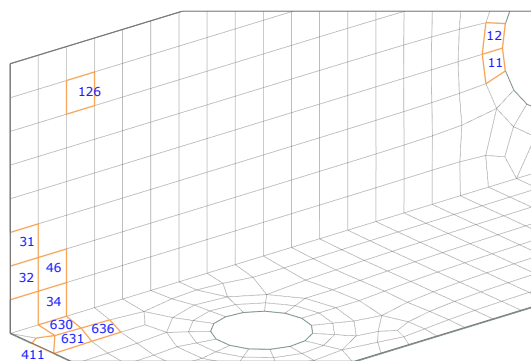


Figure 5.6: The minimum strain filter

Table 5.1: Minimum strain filter

Element ID	Von Mises ( $\varepsilon_{VM}$ )
11	$80.33 \times 10^{-6}$
12	$241.24 \times 10^{-6}$
31	$739.94 \times 10^{-6}$
32	$539.03 \times 10^{-6}$
34	$907.65 \times 10^{-6}$
46	$539.82 \times 10^{-6}$
126	$831.40 \times 10^{-6}$
411	$578.72 \times 10^{-6}$
630	$876.05 \times 10^{-6}$
631	$383.51 \times 10^{-6}$
636	$983.64 \times 10^{-6}$

### 5.1.5 Strain Gradient Filter

Strain gradient is the rate at which strain changes through a structure, and experience has taught that gauges should be glued in areas of high strain, but with small strain gradients. The typical problem associated with large strain gradients is matching the measured strain value to a finite-element in the FE model. Barry (2017), for example, found that at multiple locations the measured value did not correspond to the simulated strain value and it specifically occurred in areas with large strain gradients. Barry (2017) proceeded to investigate elements in a 20 mm radius of the approximate strain gauge position, and the gauge-element correlations were improved by choosing different finite-elements within this vicinity. An extract from Barry (2017) is provided in Table 5.2, where the initially calculated and improved percentage differences are compared. To conclude, if a gauge is not precisely glued on the exact candidate point as intended in an area with large strain gradients, the sensor could measure extreme erroneous strain values that will influence the accuracy of the reconstructed loads.

Large strain gradients in an FE model can be amplified if the step from one element to another adjacent element is too large, but by executing a mesh refinement or smoothing operation, the effect of this exaggerated gradient can be reduced (Cook *et al.*, 2002). Barry (2017), however, performed mesh refinements on all simulations to ensure that the models were converged yet pairing measured and simulated values persisted in being a problem (Barry, 2017, p.87). Conclusively, a filter needs to be designed that pre-processes the strain data so that the placement of gauges in areas where it could potentially measure erroneous values due to large strain gradients, can be avoided.

Table 5.2: The percentage difference calculated between measured and simulated strain values at elements in the FE model that correspond to the actual location of the gauge. Then, the percentage difference was calculated between the measured and simulated strain values of neighbouring elements within a 20 mm proximity of the initially selected element. Barry (2017) accepted values below 20 % which are indicated in bold.

Strain Gauge	Initial Element % Difference	Nearby Elements % Difference	Strain Gauge	Initial Element % Difference	Nearby Elements % Difference
A	62.0 %	<b>-15.7 %</b>	M	50.0 %	-33.3 %
C	<b>-10.0 %</b>	<b>-15.1 %</b>	N	<b>20.0 %</b>	<b>-9.4 %</b>
D	<b>-3.4 %</b>	<b>-14.6 %</b>	O	24.0 %	<b>-16.5 %</b>
E	31.3 %	<b>19.2 %</b>	P	21.5 %	<b>-7.8 %</b>
F	172.0 %	<b>19.9 %</b>	S	124.6 %	<b>10.8 %</b>
K	38.1 %	<b>16.4 %</b>	T	<b>18.2 %</b>	<b>9.7 %</b>
L	25.9 %	<b>-10.0 %</b>	W	<b>17.4 %</b>	26.1 %

Strain gradient depends on the interaction between finite-elements; thus, an appropriate parameter should be assigned to the graph edges. Strain values are direction-dependent, which makes it mathematically incorrect to compare the simulated strain values of different finite-elements if these values do not reference the same coordinate system. For example, in Figure 5.1, the elemental coordinate systems (ECSYS) of Elements A and B from Section 5.1.1 are not identical, thus  $\varepsilon_x$  of Element A cannot be compared to  $\varepsilon_x$  of Element B. The reader is reminded that Nastran only outputs strain in the coordinate system of the element. Therefore, the gradient is calculated using the Von Mises strain, since it is an equivalent measure that is coordinate system independent and incorporates all directions of in-plane strain. The strain gradient between two neighbouring elements equal:

$$SG_{AB} = \frac{|\varepsilon_A - \varepsilon_B|}{r_{AB}} \quad (5.2)$$

where  $\varepsilon_A$  is the Von Mises strain of Element A and  $\varepsilon_B$  is the Von Mises strain of Element B at the surface of the structure. The radius,  $r_{AB}$ , is the distance between the element centroids:

$$r_{AB} = \sqrt{(C_{x,A} - C_{x,B})^2 + (C_{y,A} - C_{y,B})^2 + (C_{z,A} - C_{z,B})^2} \quad (5.3)$$

The centroid of each element equals the vector average of either its three (CTRIA3) or four (CQUAD4) grid points  $G1$ ,  $G2$ ,  $G3$  or  $G4$  (Figure 4.1).

$$\mathbf{C}_{xyz} = \begin{cases} (G1_x + G2_x + G3_x)/3 \\ (G1_y + G2_y + G3_y)/3 \\ (G1_z + G2_z + G3_z)/3 \end{cases} \text{ or } \begin{cases} (G1_x + G2_x + G3_x + G4_x)/4 \\ (G1_y + G2_y + G3_y + G4_y)/4 \\ (G1_z + G2_z + G3_z + G4_z)/4 \end{cases} \quad (5.4)$$

The strain gradients are assigned to the graph edges and the finite-elements associated with large strain gradients should be identified next. However, the difficulty lies in choosing a mathematically justifiable border that classifies strain gradient as being acceptable or “too high”. In statistics, a large strain gradient can be considered an outlier which is a data point significantly different from the rest of the data. According to Aggarwal (2013), most outlier detection algorithms compute the “outlierness” of a data point based on how it deviates from a standard pattern. The strain gradients were calculated for the FE model in Figure 5.1 and graphed in Figure 5.7.

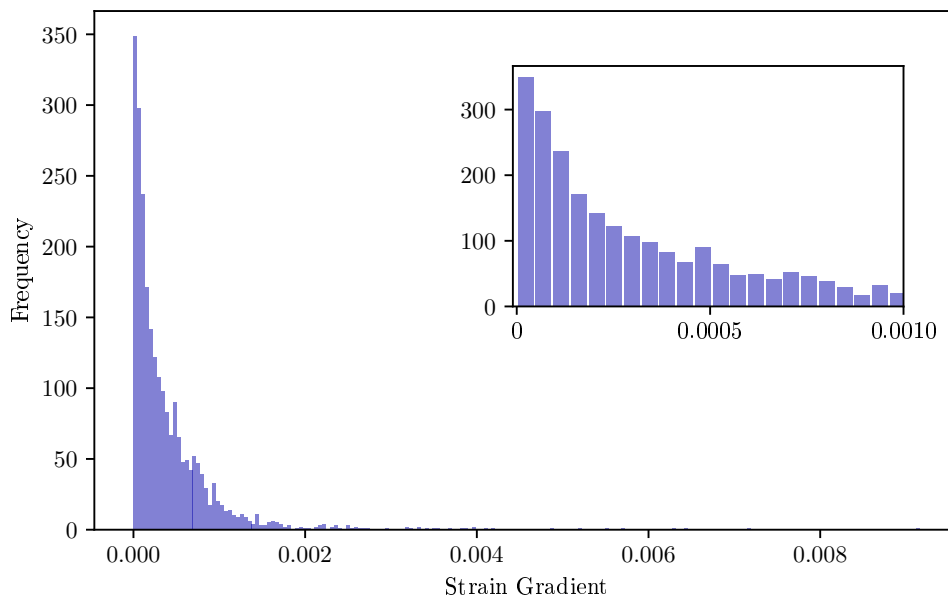


Figure 5.7: Histogram of calculated strain gradients for the FE model in Figure 5.1. The data is skewed to the right and follows a Weibull distribution.

The data profile of the strain gradient is shown in Figure 5.7, and it is seen in this histogram that the data is severely skewed to the right and follows a Weibull distribution. A statistically significant point that classifies data points in the tail as outliers, should be determined next. Common practice is to transform skewed data to a distribution that is as “normal” as possible to increase the validity of the associated statistical analyses (Feng *et al.*, 2014). The aim is to ultimately introduce symmetry into the data set. Statistical analyses tools for outlier detection of normal distributions include the use of standard deviations or the interquartile range (IQR). Techniques to introduce symmetry in the data set were tried and proven to be unsuccessful (see Appendix B). Further research found a method proposed by Hubert and Van der Veecken (2008) on how to detect outliers in skewed data, by adjusting a boxplot which does not rely on the assumption of a symmetrically distributed data set.

A boxplot, also known as a box-and-whisker plot, is a popular tool to visualise the data distribution of univariate data. The interquartile range of the data is enclosed in a box of which the edges represent the 25th percentile (lower quartile) and 75th percentile (upper quartile) as shown in Figure 5.8. The whiskers,  $w_1$  and  $w_2$ , of a standard plot, equals:

$$[Q_2 - 1.5 \text{ IQR}, Q_3 + 1.5 \text{ IQR}] \quad (5.5)$$

of which the IQR equals  $Q_3 - Q_1$ .  $Q_2$  are the median or middle value of the data set,  $Q_1$  are the middle value between  $w_1$  and  $Q_2$  and  $Q_3$  is the middle value between  $Q_2$  and  $w_2$ . The whiskers,  $w_1$  and  $w_2$ , are the “minimum” and “maximum” values respectively and excludes any outliers. Any values that extend beyond the whiskers are considered to be outliers (Walpole *et al.*, 2016). For this application it is only required to consider values that are greater than  $w_2$ .

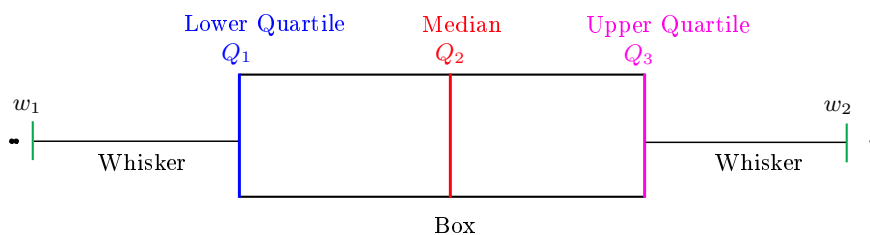


Figure 5.8: Standard boxplot with associated labels.

The method proposed by Hubert and Van der Veecken (2008) adjusts the whiskers to different scales on either side of the median; this adjusted boxplot

method has proven to make a more acceptable distinction between regular observations and outliers whilst not assuming any distribution of the data (Hubert and Vandervieren, 2008). The intervals are adjusted to:

$$[Q_1 - 1.5e^{-4\text{MC}} \text{ IQR}, Q_3 + 1.5e^{3\text{MC}} \text{ IQR}] \quad (5.6)$$

if  $\text{MC} > 0$  and

$$[Q_1 - 1.5e^{-3\text{MC}} \text{ IQR}, Q_3 + 1.5e^{4\text{MC}} \text{ IQR}] \quad (5.7)$$

for  $\text{MC} < 0$ . The medcouple, MC, is a robust alternative measurement of skewness as opposed to the classical skewness coefficient (Brys *et al.*, 2004). For univariate data  $\{x_1, \dots, x_n\}$  from a continuous unimodal distribution, the medcouple equals:

$$\text{MC} = \underset{x_i \leq Q_2 \leq x_j}{\text{med}} h(x_i, x_j) \quad (5.8)$$

where for all  $x_i \neq x_j$ , the kernel function is given by,

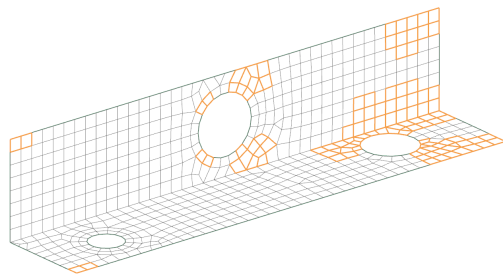
$$h(x_i, x_j) = \frac{(x_j - Q_2) - (Q_2 - x_i)}{x_j - x_i} \quad (5.9)$$

A specific definition applies for the special case where  $x_i = Q_2 = x_j$  and can be found in Brys *et al.* (2004). This case, however, “occurs with zero probability” (Hubert and Vandervieren, 2008, pg. 5). The medcouple thus equals the median of all  $h(x_i, x_j)$  values for which  $x_i \leq Q_2 \leq x_j$ . If the medcouple is equal to zero, Equations 5.6 and 5.7 will reduce to Equation 5.5. Robustats, which is a high-performance computation library of robust statistical estimators, was used to calculate the medcouple (Bovo, 2020).

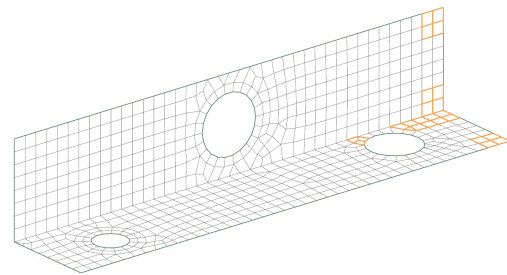
No elements must be removed from the FE solution set before applying this filter, since it is an outlier based technique which is influenced by the total number of data points within the population. Secondly, since the strain values are required, the analyst must estimate magnitudes for the applied loads. As opposed to the Minimum Strains filter, the number of elements that will be detected by the filter is not proportional to the magnitudes of the loads; thus, an assumed scaled value will also be satisfactory. This statement is explained with an example in Section 8.1. The Strain Gradient filter was applied to the sample FE model with the assumed load case in Figure 5.1. The vertices, which are linked by the edges that contain strain gradient metadata that are considered to be outliers, were identified and the associated elements are shown in the FE environment. The outliers detected



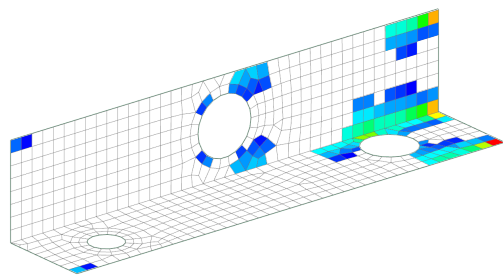
by the adjusted boxplot is compared to the outliers that would have been detected by a standard boxplot in Figures 5.9 and 5.11. It is observed that the standard boxplot detected more outliers than the adjusted boxplot method. Elements were commonly selected at discontinuities, such as sharp edges, and in areas near loads and constraints; these are all areas where large strain gradients are expected.



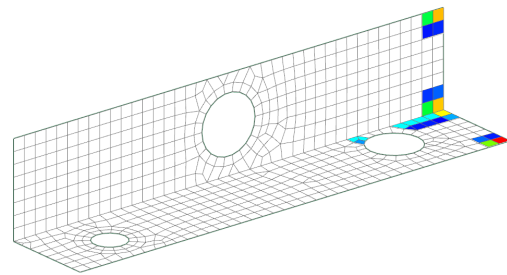
(a) Standard boxplot method (113 outliers)



(b) Adjusted boxplot method (25 outliers)



(c) Strains of standard boxplot method



(d) Strains of adjusted boxplot method

Figure 5.9: Results of the Strain Gradient filter on a sample FE model. Using the standard boxplot method (a) and the adjusted boxplot method (b). The strain overlays of these elements are provided in (c) and (d).

### 5.1.6 Concluding Remarks

All elements selected by the structural filters, i.e. the Sharp Edges, Open Edges and Triangular Element filters, are shown in Figure 5.10. It is observed that the candidate points are significantly reduced, solely due to the impracticality of mounting gauges in these selected areas. The reader is reminded that the structural filters can be used without any knowledge of the simulated strain values, but the same is not true for the strain related filters. The strain response is dependent on the input loading, thus it is required that the user provides an FE model that approximates the respective load cases, if these filters are used for static load reconstruction. Table 5.3 summarises the default parameters for each filter, which can be adjusted by the analyst.

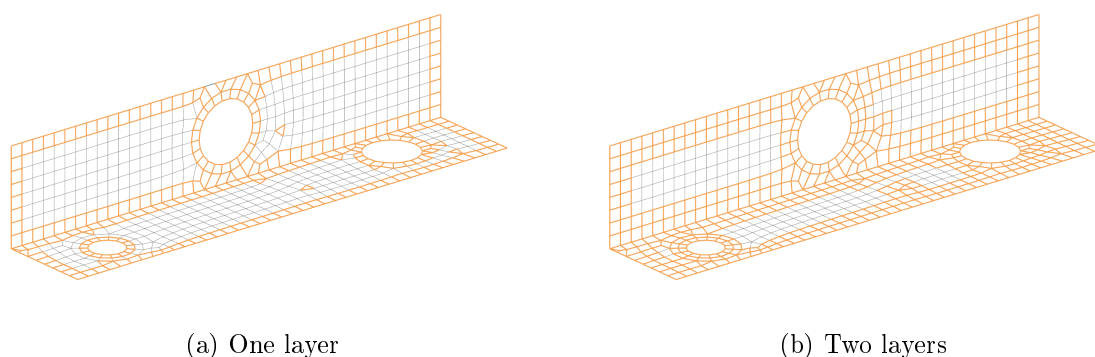


Figure 5.10: Results of all *structural* filtering on a sample FE model. In (a) only one layer of surrounding elements was removed and in (b) two layers of elements were removed.

Table 5.3: Default argument values for developed pieces of software

Variable	Default Value	Variable	Default Value
Open Edges	<code>nNeighbours</code> 5	Min. Strains	<code>minStrain</code> $10^{-4}$ mm/mm
Sharp Edges	<code>phi</code> $85^\circ \leq \phi \leq 90^\circ$	Layers	<code>nLayers</code> 1

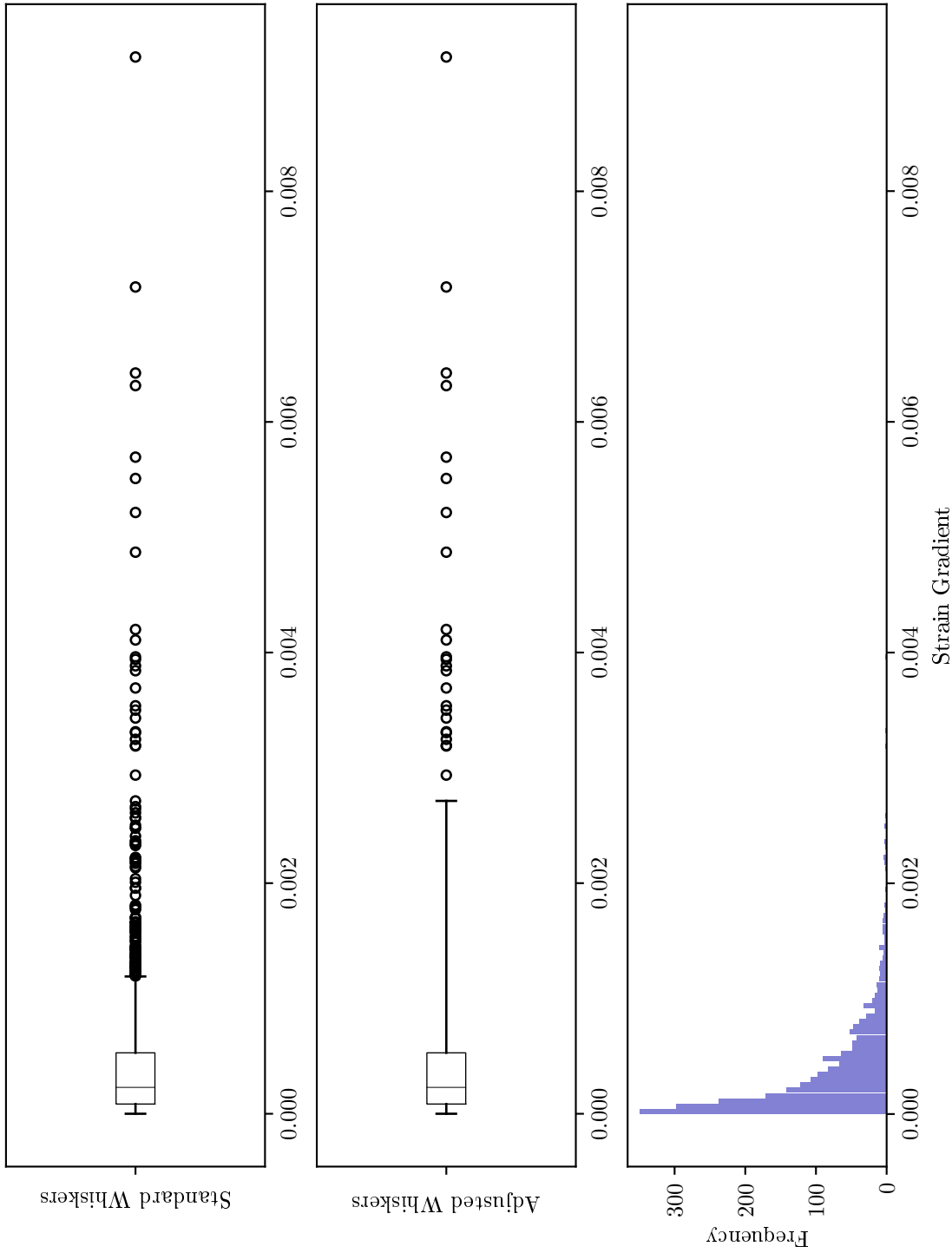


Figure 5.11: Comparison of the number of outliers detected, using a standard boxplot (whiskers defined in Equation 5.5) and an adjusted boxplot (whiskers defined in Equations 5.6 and 5.7). The histogram from Figure 5.7 is repeated here for reference.

## 5.2 Proportionality (or Design) Matrix Software

This function extracts the unit-load strain data from the output file of the FE model using pyNastran. If the model was prepared as explained in Section 4.2 and Section 4.5, the software will loop over the subcases and add the information of each subcase into dataframes (two-dimensional labelled data structures in Python), shown in Figure 5.12a. A total thickness of 1.6 mm was assigned about the reference plane and strain values were computed at the centre (CEN) of the elements. The  $\varepsilon_{xx}$  values at fiber distances greater than zero (`fiber_distance > 0`), which translates to the axial direction of gauges at the surface of the structure, are read into another dataframe (Figure 5.12b) which constitutes the first  $p$  rows of the candidate set.

ElementID	NodeID	Location	index	fiber_distance	Strain in ECSYS			Principal Strains			
					exx	eyy	exy	angle	emax	emin	von_mises
1	CEN	Top	0	0.8	-0.000169	-0.000651	0.000689	27.505350	0.000011	-0.000830	0.000557
		Bottom	1	-0.8	-0.000312	-0.000756	0.000484	23.727573	-0.000206	-0.000863	0.000520
2	CEN	Top	2	0.8	-0.000190	-0.000714	0.000514	22.222820	-0.000085	-0.000819	0.000520
		Bottom	3	-0.8	-0.000266	-0.000713	0.000461	22.973188	-0.000169	-0.000810	0.000494
3	CEN	Top	4	0.8	-0.000156	-0.000728	0.000456	19.268681	-0.000076	-0.000808	0.000515
		Bottom	5	-0.8	-0.000231	-0.000730	0.000380	18.668697	-0.000167	-0.000794	0.000483

(a) Dataframe as read from Nastran's OP2 file.

ElementID	Subcase (or Load) 1	Subcase (or Load) 2	Subcase (or Load) 3
1	-0.000169	-0.000031	-0.000768
2	-0.000190	-0.000087	-0.000714
3	-0.000156	-0.000028	-0.000587
4	-0.000123	0.000020	-0.000444
5	-0.000084	0.000081	-0.000298

(b) Dataframe constituting preliminary candidate set

Figure 5.12: The dataframe of elemental strain values, when read by OP2 interface, is shown in (a). This example contains the calculated strain values of Subcase 1 of an FE model with the input file shown in Figure 4.4. The dataframe in (b) contains the first  $p$  rows of the candidate set. This FE model consists of five finite-elements ( $p$ ) and has three imposed unit-loads ( $n$ ).

Strain in the elemental  $x$ -direction was chosen as the computerised axial direction of gauges; it is required to create an extended candidate set to accommodate various gauge orientations on the surface of a structure. Gauges can only be rotated in-plane (Figure 5.13), thus the axial strain at any angle  $\theta$  equals (Hibbeler and Sekar, 2013, pg. 536):

$$\varepsilon_{\theta} = \varepsilon_{xx} + \varepsilon_{yy} + (\varepsilon_{xx} - \varepsilon_{yy})\cos(2\theta) + \frac{\varepsilon_{xy}}{2}\sin(2\theta) \quad (5.10)$$

The candidate set was extended to include four rotations ( $g = 4$ ) at  $\theta = 0^{\circ}$ ,  $45^{\circ}$ ,  $90^{\circ}$  and  $135^{\circ}$  for which the results from Equation 5.10 were concatenated to construct the extended candidate set. These orientations can be modified, and the analyst is not limited to using all four of these angles.

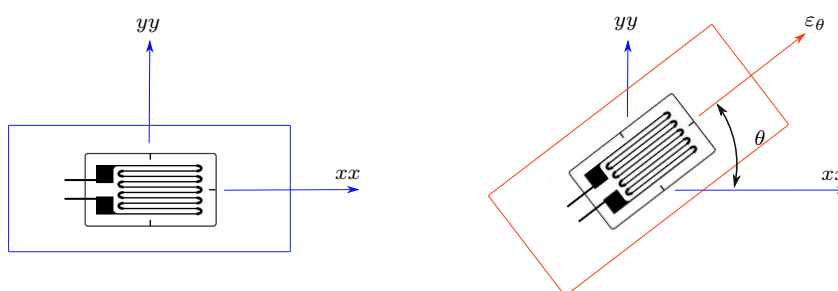


Figure 5.13: Schematic of in-plane strain transformation to demonstrate the rotation of gauges on the surface of a structure.

The second function is Federov's Exchange Algorithm (Miller and Nguyen, 1994), that reduces the extended candidate set to a design matrix that is ultimately used as the proportionality matrix in Equation 3.5. The candidate set that contains all the possible gauge location-orientation combinations is an argument (or variable) passed to the algorithm, and the candidate points that will maximise the determinant of the information matrix will be selected from this set. It is worth noting that the algorithm is deterministic; thus multiple random starting designs (default = 1000 runs) are evaluated before selecting the best design matrix, to deal with the presence of local minima. It also is required that the user passes the algorithm an integer value  $m$  ( $\geq n$ ) that equals the number of desired design points in the design matrix. However, as mentioned in Section 3.2.2, the algorithm does not attempt to force unique points, i.e. the same candidate point may be chosen several times; consequently, it will not necessarily find  $m$  distinct points.

## 5.3 Summary

This chapter detailed the various pieces of software that were developed. The first algorithm identifies which finite-elements to exclude from the candidate set, based on certain structural and strain related criteria. The second algorithm compiles, extends and optimises the candidate set to a proportionality matrix that dictates gauge mounting locations and orientations.

# Chapter 6

## Implementation of Filters

The previous chapter detailed the design of the filtering software and its application on a simple FE model. Four numerical models were additionally made available and used to test the performance of each filter. Three models were originally from another research project on reinforced pipes by Barry (2017), and the last model is a commercial model of a hauler truck sub-assembly constructed by a local engineering company.

### 6.1 Case Study I: Reinforced Pipe Simulations

Barry and Venter (2019) investigated reinforced steel pipes for bulk water pipelines. FE analyses were performed to investigate the stress-strain behaviour of various models and to evaluate the experimentally obtained measurements of the American Water Works Association's (AWWA) M11 design model. The pipes were modelled as mid-plane shell models and meshed with first-order bi-linear quadrilateral shell elements. A surface-to-surface fixed contact was used at the collar (Figure 6.1a) and wrapper (Figure 6.1c) interfaces since a zero relative displacement was assumed. Rigid (RBE2) elements constrained all nodes at the open ends of the pipes to an independent, imaginary centre node to which a force equal to the internal pressure was assigned. An independent node at one end was fully constrained to prevent rigid body motion.

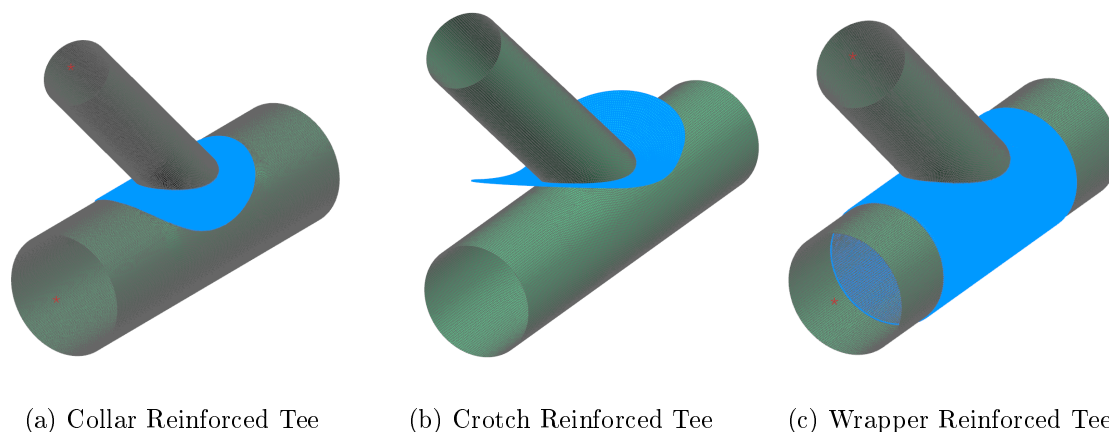


Figure 6.1: FE models of reinforced pipes as provided by Barry (2017). The reinforcements are highlighted in blue.

### 6.1.1 Structural Filters

The results of the Open Edges filter are provided in Figures 6.2a, 6.2c and 6.2e. Elements with five or fewer neighbours were considered (`nNeighbours = 5`), since a mesh refinement was already performed on all models. In Figure 6.2c it is seen that the filter did not select all elements on the crotch plate. However, the gaps are accounted for when the second layer of elements are removed (Figure C.1c). None of these models contain any triangular 2D elements. The results of the Sharp Edges filter are provided in Figures 6.2b, 6.2d and 6.2f. Neighbouring elements with normal angles within the range  $5^\circ < \phi < 175^\circ$  are highlighted. It is observed in Figures 6.2d and 6.2f that elements were selected on the vertical extension of the pipes. Further inspection on the wrapper reinforced model shows that the angles for these adjacent elements are within the range  $5^\circ < \phi < 5.5^\circ$ . The investigation was repeated for the crotch reinforced model, and the findings are summarised in Table 6.1.

Table 6.1: Incorrectly selected elements by Sharp Edges filter on pipe models.

Model	Total Elements in Mesh	Elements Incorrectly Selected by Filter	Range	Average Element Size [mm]
Collar	110174	0	-	10
Crotch	48262	268	$5.0 < \phi < 5.5$	20
Wrapper	70973	15	$5.0 < \phi < 6.6$	10

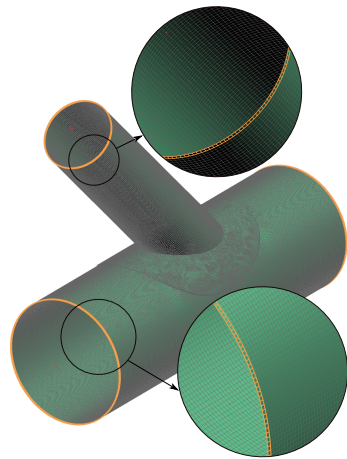


The crotch model was most affected by the incorrect selection of elements by the Sharp Edges filter. It has a coarser mesh than the other models, which means that a single finite-element covers a greater surface area; this resulted in the normals of neighbouring elements not to be parallel on a curved surface. Filters were designed to automate the selection process of elements that need to be excluded from the candidate set, because manually selecting these elements is tedious and time-consuming. It is, however, still required that the analyst reviews the filter selected elements in the FE pre-processor.

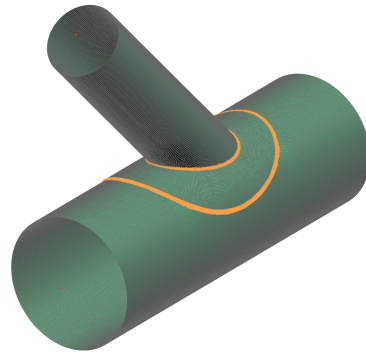
### 6.1.2 Strain Filters

Strain filters identify any finite-elements that are not measurable by a strain gauge or elements within an area with large strain gradients. For these filters to work with load reconstruction, estimates of the load magnitudes need to be made. However, since these models were externally procured and are real-life simulations with known loads, the models were used with forces magnitudes as provided. The strain response of each model is shown in Figure 6.3 for reference.

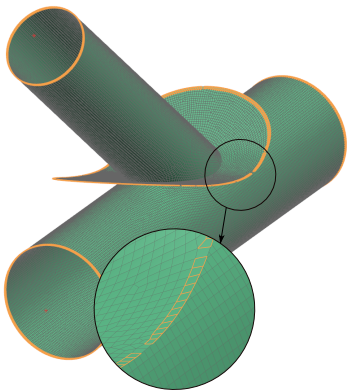
The Minimum Strains filter was used to select all elements with simulated strain values below  $100 \mu\text{mm}/\text{mm}$ , and the results are shown in Figure 6.4. For the crotch reinforced pipe, one can see that the Minimum Strains filter chose elements within the dark blue areas, which corresponds to small strains. The results of the Strain Gradient filter, that follows the adjusted boxplot outlier detection method, are shown in Figure 6.5. It is observed that the algorithm managed to identify elements in areas with rapidly changing strain contours. These areas are at the pipe intersections, and where the reinforcements of the collar and wrapper models connect to the pipe; it is expected to find high strain gradients at structural discontinuities. Outliers were also detected at the edges where reaction forces were applied. These loads get extrapolated to the dependent nodes of the RBE2 constraints, and it is expected to find a strain gradient at these load distribution points.



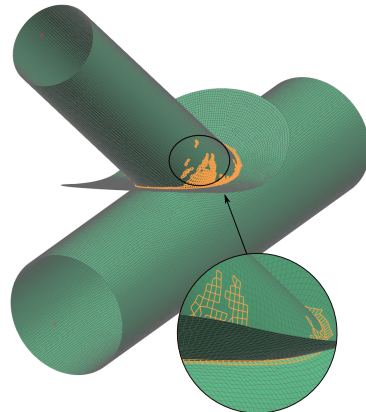
(a) Open Edges: Collar



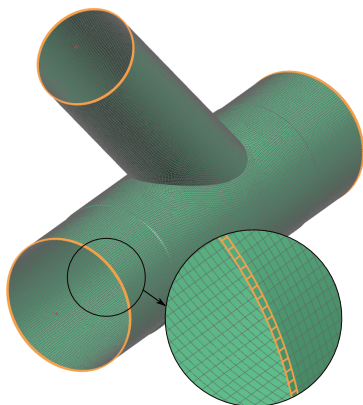
(b) Sharp Edges: Collar



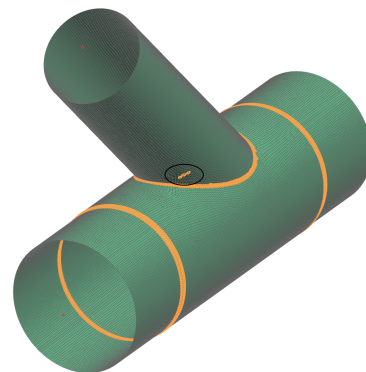
(c) Open Edges: Crotch



(d) Sharp Edges: Crotch

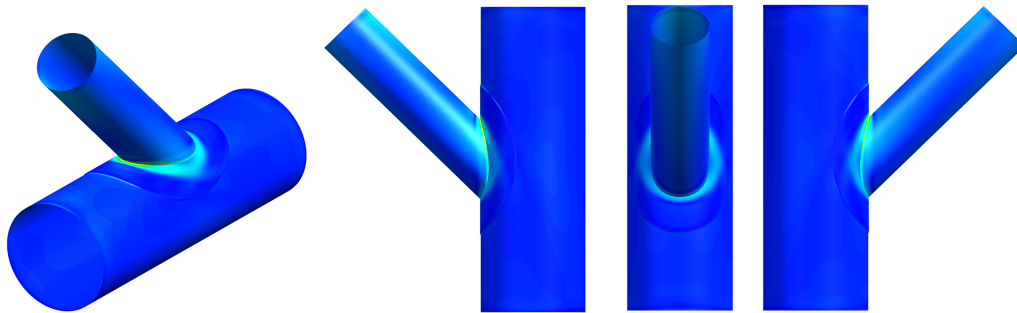


(e) Open Edges: Wrapper

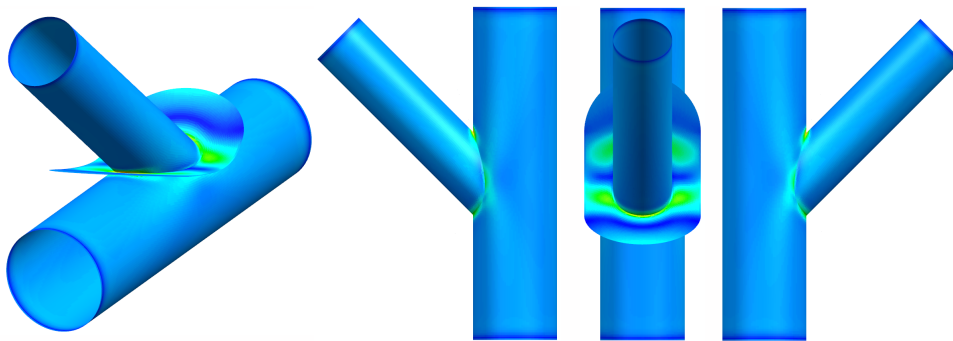


(f) Sharp Edges: Wrapper

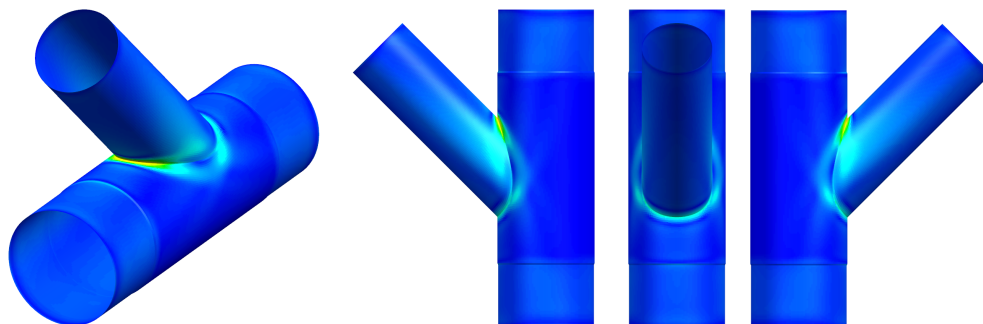
Figure 6.2: Structural filters on reinforced pipes with single layer removal. The elements in green are elements that are kept and those in orange are filtered out.



(a) Collar Reinforced Tee



(b) Crotch Reinforced Tee

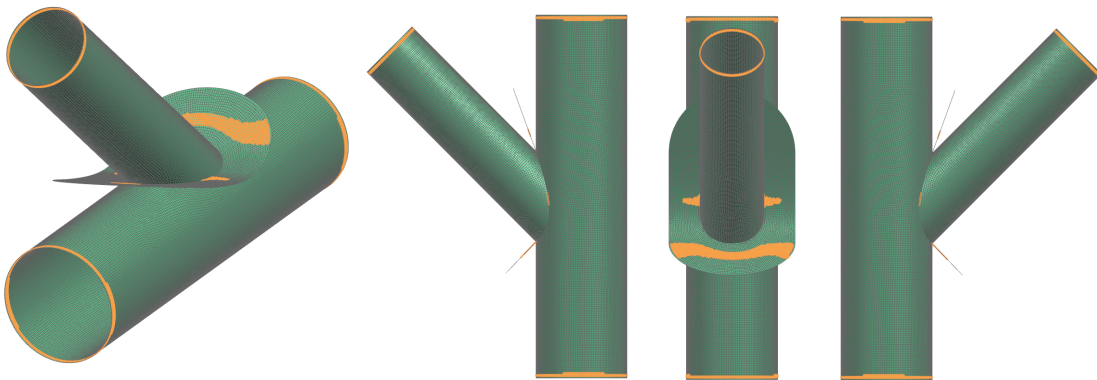


(c) Wrapper Reinforced Tee

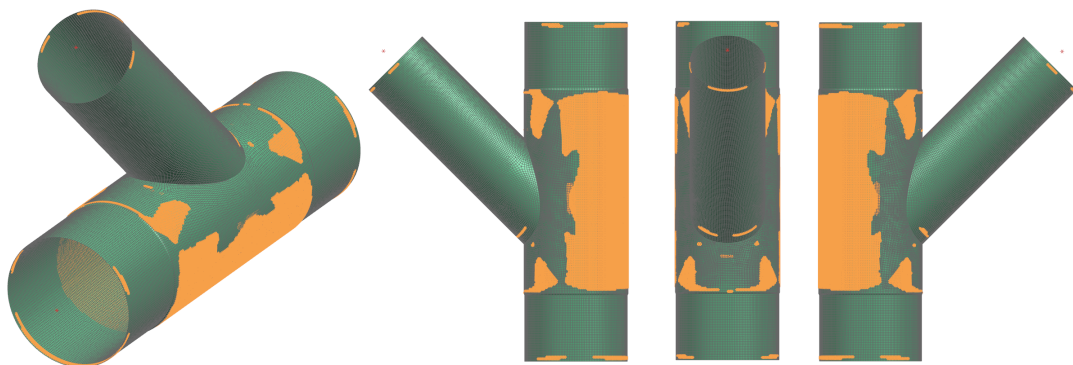
Figure 6.3: Strain results of reinforced pipes as provided by Barry (2017).



(a) Collar Reinforced Tee

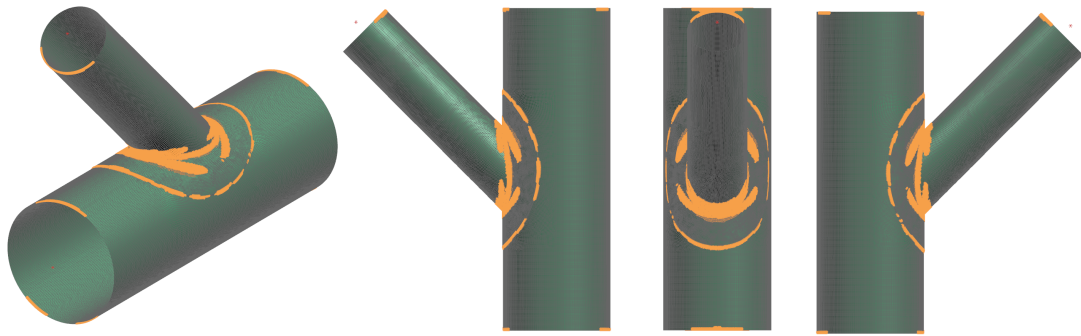


(b) Crotch Reinforced Tee

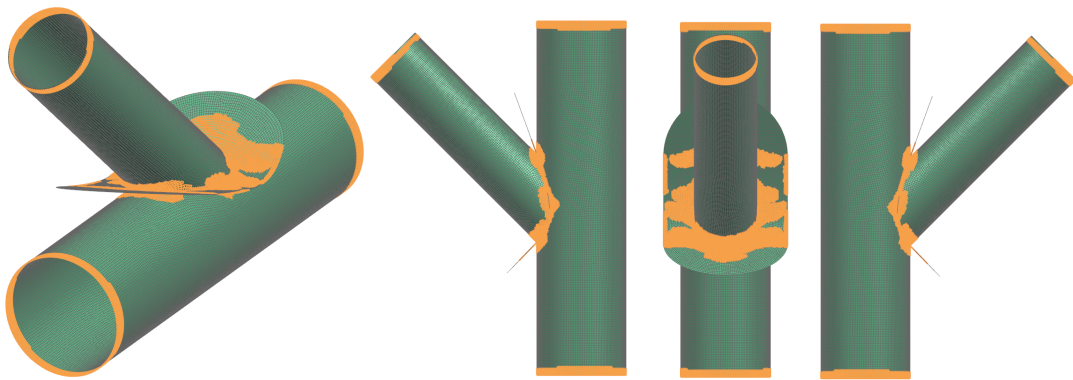


(c) Wrapper Reinforced Tee

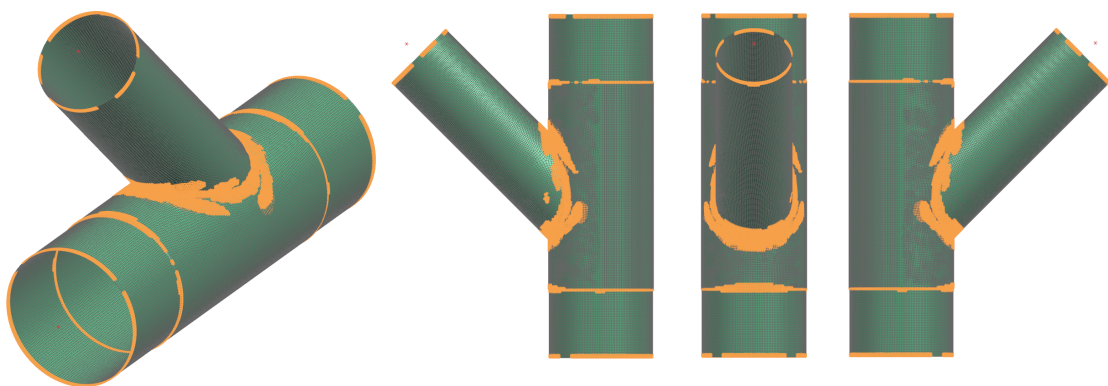
Figure 6.4: Minimum Strains filter on reinforced pipes. The elements in green are elements that are kept and those in orange are filtered out.



(a) Collar Reinforced Tee

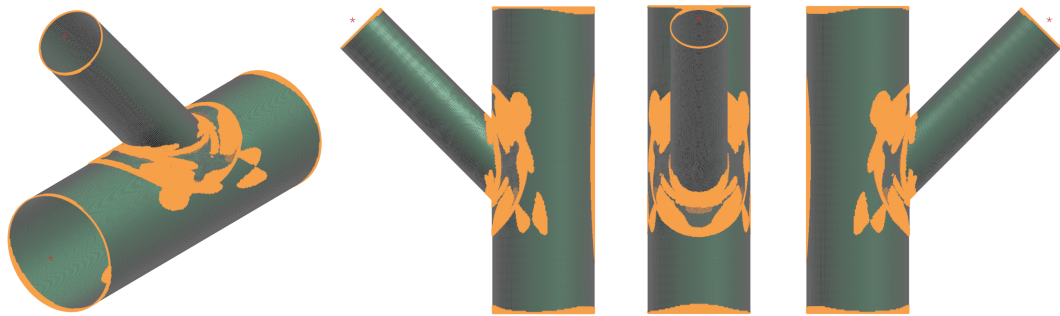


(b) Crotch Reinforced Tee

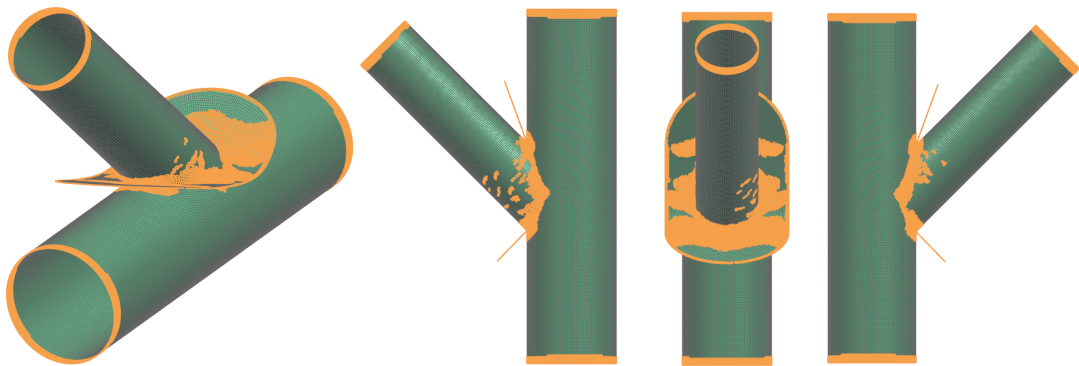


(c) Wrapper Reinforced Tee

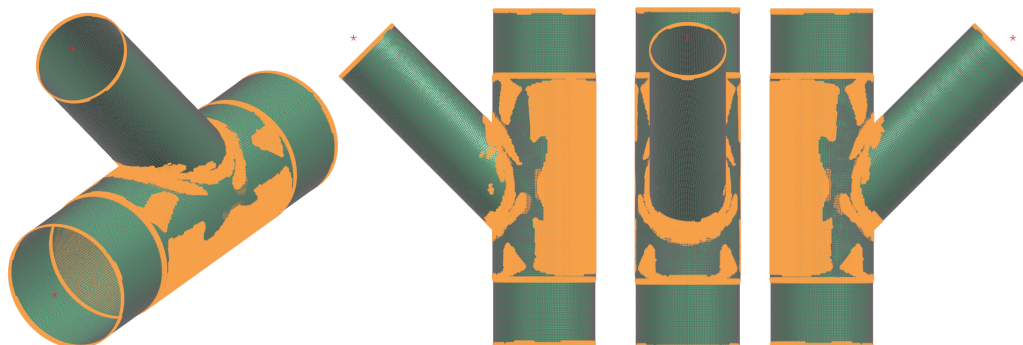
Figure 6.5: Strain Gradient filter, using the adjusted boxplot method, on reinforced pipes. The elements in green are elements that are kept and those in orange are filtered out.



(a) Collar Reinforced Tee



(b) Crotch Reinforced Tee



(c) Wrapper Reinforced Tee

Figure 6.6: All filters on reinforced pipes. The elements in green are elements that are kept and those in orange are filtered out.

## 6.2 Case Study II: Hauler Truck Sub-Assembly

An FE model was created of a sub-assembly on a hauler truck. This model does not solely consist out of two-dimensional (2D) elements, as was the case for the reinforced pipe simulations and other models used for testing the filters. The result of all structural and strain filters are shown in Figure C.3.

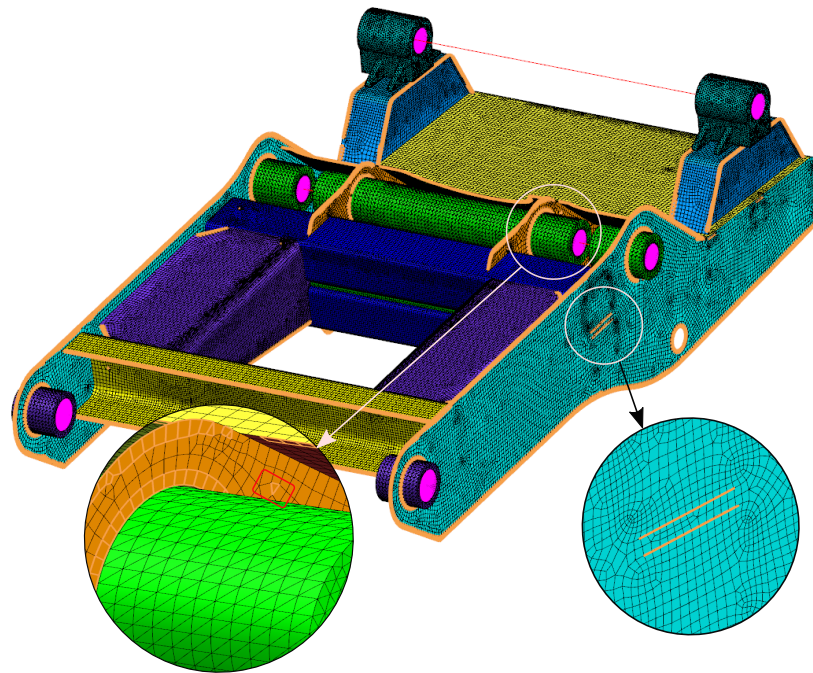
### 6.2.1 Structural Filters

The results of the Open Edges filter for single and double layer removals are shown in Figures 6.7a and C.2a and the findings were similar to the reinforced pipe simulations. It was noticed in Figure 6.7a that the Open Edges filter chose certain triangular elements, but since the Triangular Element filter will remove these elements, it is not a cause for great concern. In Figure 6.7a it appears as if elements were wrongfully selected where the dark blue mesh connects to the turquoise mesh, as shown in the insert; however, these elements do not share nodes with the turquoise mesh, due to the impracticality of welding the parts together within that area.

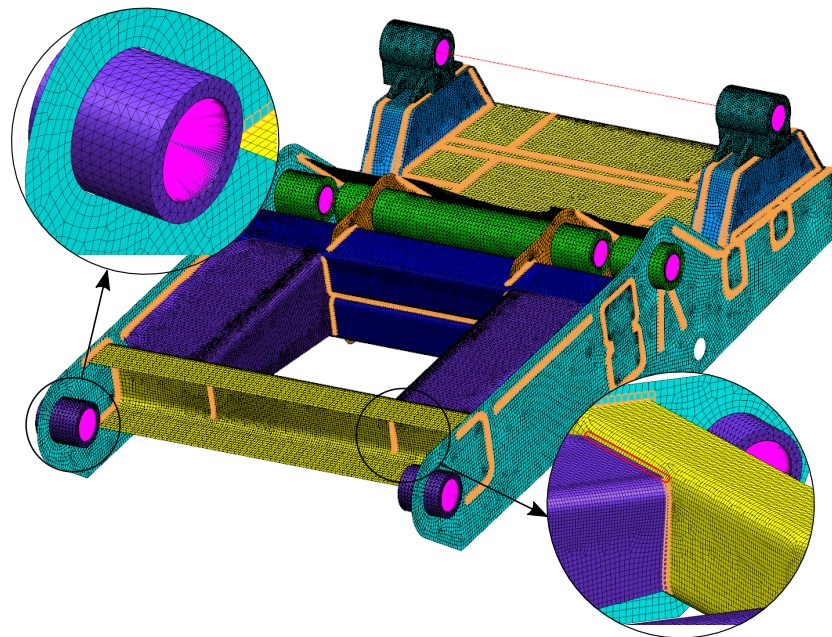
The results of the Sharp Edges filters are shown in Figure 6.7b and Figure C.2b. Normal angles within the range  $85^\circ < \phi < 95^\circ$  (perpendicular elements) were considered. It appears that not all elements (encircled in red) were selected; the angles between these elemental normals are actually at an average of  $65^\circ$ . The area where the 3D mesh fits into the 2D mesh was also not part of the selection, because these elements are not connected with mutual nodes. Note that the aim of the filters is to *decrease* the user's input, but not completely remove their contribution. One's discretion should be used when choosing a range of angles and to always validate the filter selection.

### 6.2.2 Strain Filters

The results of the Minimum Strains filter are shown in Figure 6.8a where strain values below  $100 \mu\text{mm}/\text{mm}$  were filtered out. Results for the Strain Gradient filter, that follows the adjusted boxplot outlier detection method, are shown in Figures 6.8b. Elements were selected by the filter at locations where high strain gradients are expected. Outliers were typically identified where the different meshes connect, such as sharp edges, and within the vicinity of applied loads and constraints (encircled with red). The filter also managed to select elements that comprise the modelled welds, i.e. according to the filter a large strain gradient exist in the welded areas.



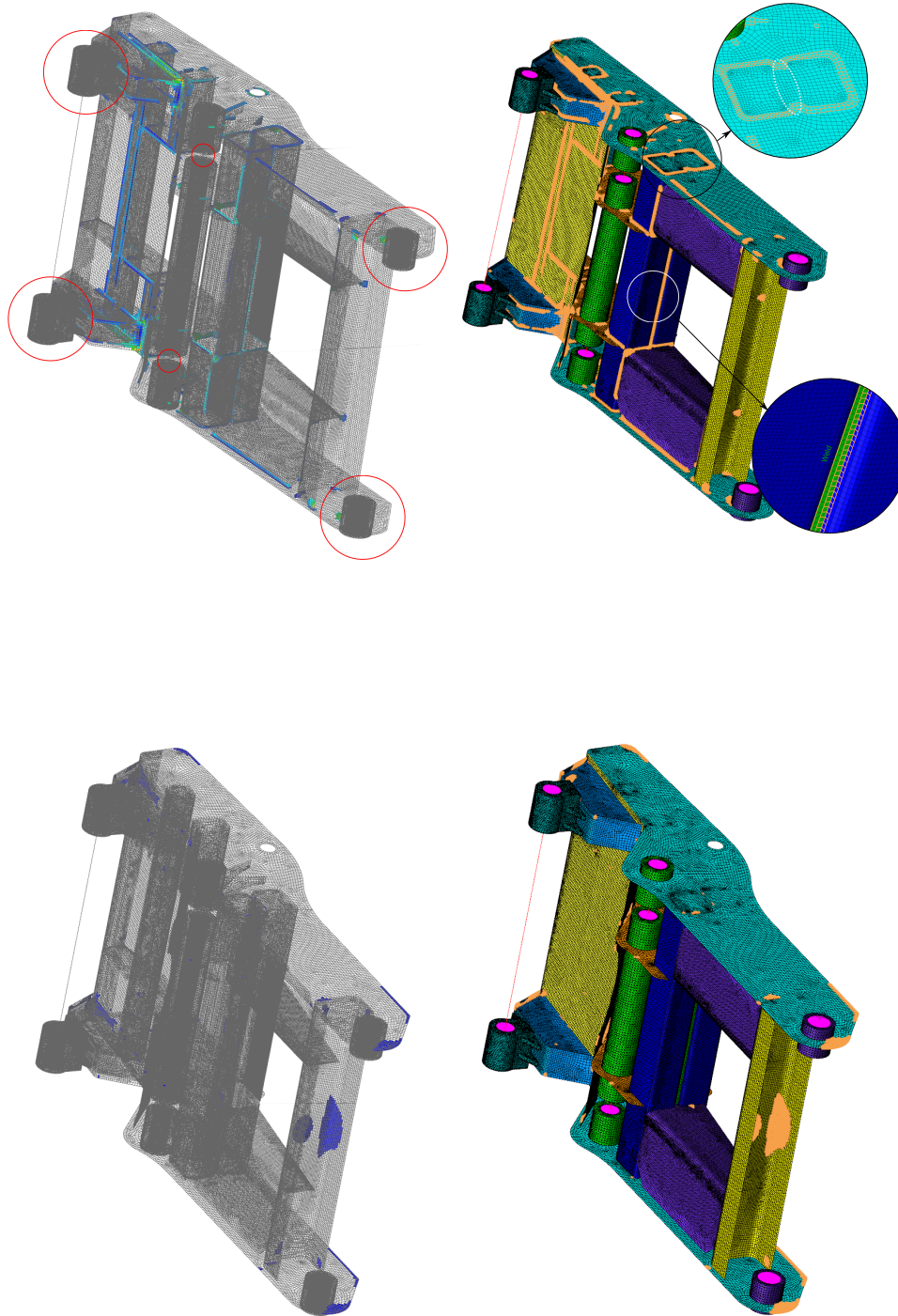
(a) Open Edges Filter



(b) Sharp Edges Filter

Figure 6.7: Structural filters on hauler truck model with single layer removal.





(a) Minimum Filter

(b) Strain Gradient Filter

Figure 6.8: Strain filters on hauler truck model.

### 6.3 Summary of Filter Selection

Various filtering functions were tested on four real-life FE analyses which allowed the evaluation of the software and further development thereof. Table 6.2 summarises the percentage elements that each respective filter removed from the FE models. For the hauler model, 7.47 % of the elements can be excluded from the candidate set, only due to the inability of mounting a strain gauge at sharp edges. Any elements that the filters ‘incorrectly’ selected were not excluded from these calculations, and individual filters might have removed similar elements. The “All Filters” row refers to the combined number of elements removed by all filters. Conclusively, the filters significantly reduce the effort required to manually select finite-elements, but the user is still required to review all filter selections to identify any elements that were incorrectly selected as in Figures 6.2d and 6.2f.

Table 6.2: Summary of elements removed by filters on real-life FE models.

	Collar		Crotch		Wrapper		Hauler Model	
Total 2D Elements	110 174	100 %	48 262	100 %	70 973	100 %	123 750	100 %
Open Edges	728	0.66 %	717	1.49 %	520	0.73 %	2 965	2.40 %
Sharp Edges	2 415	2.19 %	713	1.48 %	2 306	3.25 %	9 245	7.47 %
Triangular Elements	-		-		-		1 362	1.10 %
Minimum Strains	13 488	12.24 %	1 119	2.32 %	13 457	18.96 %	2 638	2.13 %
Strain Gradient	6 525	5.92 %	5 464	11.32 %	5 818	8.20 %	10 376	8.38 %
All Filters	19 939	18.10 %	6 264	12.98 %	19 654	27.69 %	17 379	14.04 %

## Chapter 7

# Numerical Investigations on Design Matrix

Reducing the candidate set to a proportionality matrix seems straightforward until certain practicalities are considered. For example, typical loading conditions experienced by un-powered railway bogies with central pivoting and two side-bearers (see Figure 7.1) are illustrated in Figure 7.2. Potentially, nine loads can be imposed on the bogie, but not necessarily all simultaneously. According to BS EN 13749:2011, two cases are considered for mass bearing vertical forces: in Case 1, the mass of a coach or wagon is either entirely carried by the pivot ( $F_p$ ) or in Case 2, also known as *rolling*, the force is applied to both the pivot and one side-bearer (either  $F_{z1}$  or  $F_{z2}$ ). If a train vehicle travels around a bend, an additional transverse axle force ( $\pm F_y$ ) will also act on the bogie. If the wheels do not align accurately with the rail, longitudinal lozenging forces will exist.

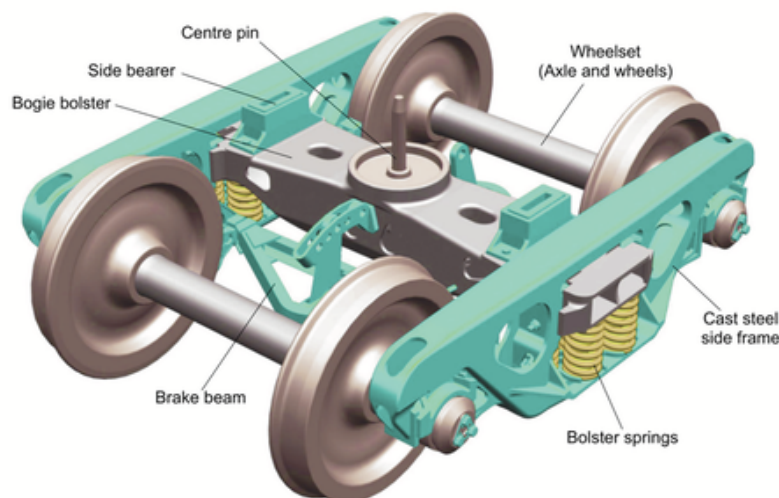


Figure 7.1: An un-powered railway bogie with central pivoting and two side-bearers (Connor, 2019).

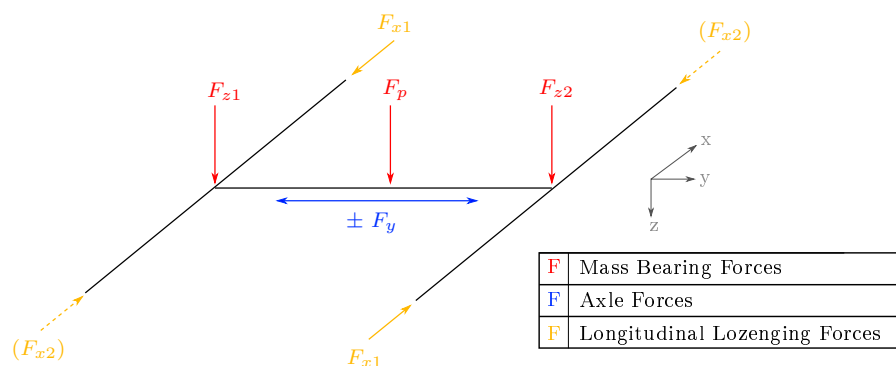


Figure 7.2: Typical forces experienced by a bogie with a central pivot and two side-bearers.

It will be investigated whether all potential forces should be included in the candidate set or only those active during a particular operation. This aspect was not dealt with in the literature studied, since previous work by other researchers only had a single load case where all components were active. It will be investigated how the optimisation process, that dictates gauge mounting locations and orientations, is affected and how the number of design points in the proportionality matrix influences the reconstruction of loads. The numerical model in Figure 7.3, which was the initial concept for a physical load reconstruction experiment, will be used for these studies. It should be noted that a mesh refinement was performed, but that no filtering was applied.

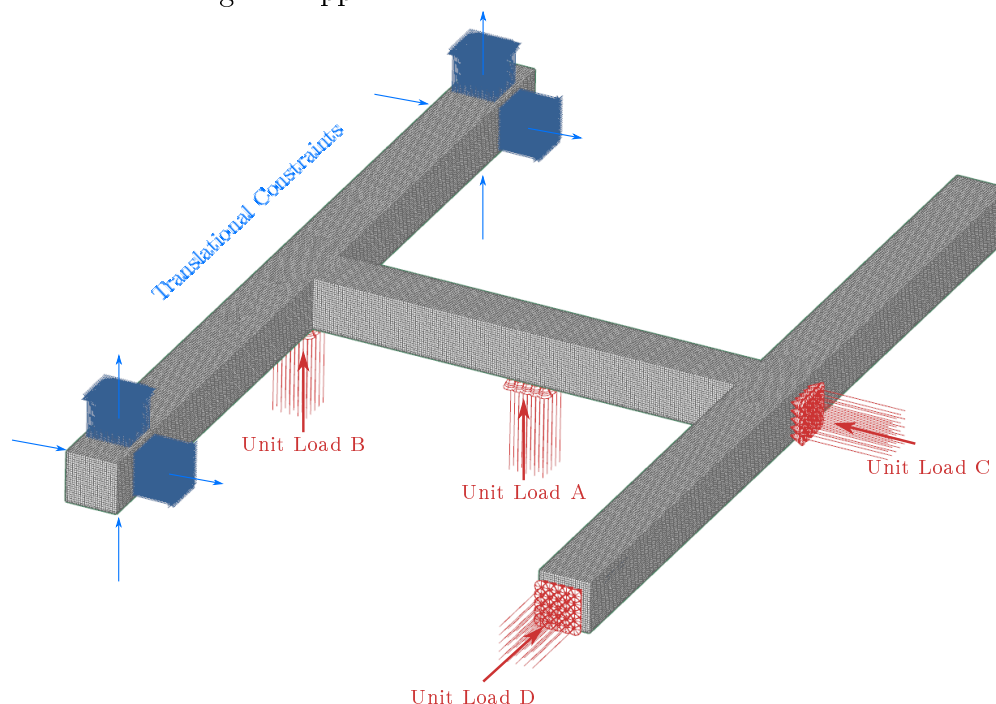


Figure 7.3: Finite-element (FE) model of initial testing setup that is used for numerical studies.

## 7.1 Optimal Number of Strain Gauges

A decision needs to be made on how many candidate points to include in the proportionality matrix, since it ultimately dictates the number of strain gauges that should be mounted. According to Gupta (2013), more gauges will result in a better estimate of the applied loads, since additional information is known, but it was also noted in Section 3.2.2 that Federov's Exchange Algorithm does not attempt to force unique design points. This characteristic of the algorithm can cause duplicate rows in the design matrix to exist.

In Test Cases 1 to 3, all four potential loads are simultaneously applied at unit-load positions and will be used to investigate the statements as mentioned earlier. One should be reminded that the minimum number of candidate points to be included in the proportionality matrix,  $m$ , must be equal or greater than the number of columns in the candidate set, i.e.  $m \geq n$ . Thus, there should be at least four rows in the design matrix for Test Cases 1 to 3. The linear static solution of each test case in Figure 7.4 was solved, and a uniformly distributed random error was arbitrarily added to the strain results, i.e.

$$Cf' = \varepsilon + e \quad (7.1)$$

where  $e$  is a  $(m \times 1)$  vector with  $-0.05\varepsilon_i \leq e_i \leq 0.05\varepsilon_i$ . The candidate set of each test case was constructed from the same unit-load model in Figure 7.3, thus the design (or proportionality) matrices will be identical for all test cases.

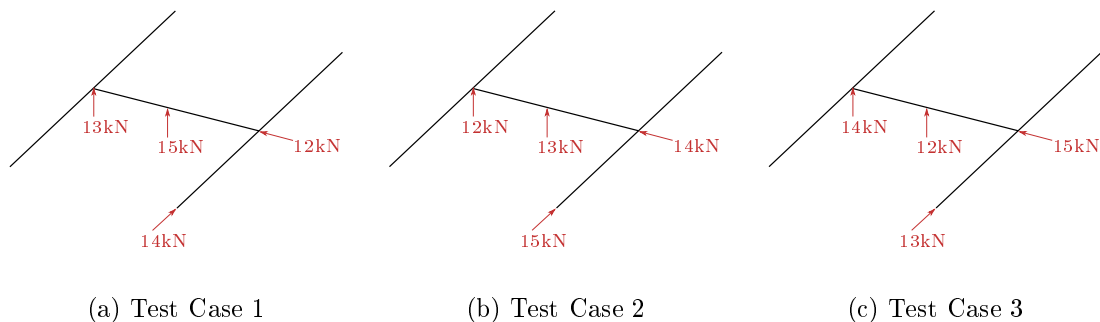


Figure 7.4: Test cases for investigating how the number of design points (i.e. strain gauges) influence load reconstruction. All four potential loads are applied simultaneously.

The least-squares estimation of  $\mathbf{f}'$  was determined for 100 different error induced strain vectors (i.e.  $\boldsymbol{\varepsilon} + \mathbf{e}$ ). The percentage root-mean-square (RMS) error between the applied and calculated forces were determined as follows (Gupta, 2013, pg. 30):

$$e_{\%rms} = \left( \frac{\sqrt{\sum (f_{app} - f_{rec})^2}}{\sqrt{\sum (f_{app})^2}} \times 100 \right) \% \quad (7.2)$$

where  $f_{app}$  is the measured (or known) applied load, and  $f_{rec}$  is the reconstructed load. This calculated RMS error for Test Cases 1 to 3 is plotted in Figure 7.5 and Figure 7.6 against the number of design points ( $m$ ) the user requested to be in the design matrix. As mentioned, even though the user requests  $m$  design points, the algorithm does not always manage to find  $m$  distinct design points. The proportionality (or design) matrices used in Figure 7.5 only contain the distinct design points, and in Figure 7.6, the duplicate points were included in the proportionality matrix, i.e. the same row may appear multiple times.

From Figure 7.5 it can be seen that the optimal number of design points for this particular model equals double the number of unit-loads (candidate set columns ( $n$ )) and that it exceeds the performance of 9 design points. Even though the user increased the request for design points, Federov's Exchange Algorithm failed in finding the corresponding amount of distinct points. Figure 7.6 proves that adding duplicate points makes no significant improvement in the calculated RMS error, which is confirmed by Figure 7.7. The minimum RMS error in Figure 7.6 corresponds to 9 design points; however, only 8 of these points are distinct. It is thus concluded that, for this particular experiment, a number of strain gauges that equals double the number of unit-loads (i.e. eight strain gauges) are the optimal quantity for reconstructing the applied loads and it is sufficient to only include the distinct design points in the proportionality matrix.

## 7.2 Different Optimisation Methods

In the introduction of this chapter, it was explained how a bogie has multiple potential forces, but that not all are necessarily simultaneously applied. If a bogie travels around a bend and the vehicle mass is carried by the pivot and one side-bearer, only three of the nine potential loads will be imposed ( $F_p$ ,  $F_{z1}$  or  $F_{z2}$ , and  $+F_y$  or  $-F_y$ ). An option exists to optimise the full candidate set, i.e. the nine-column set, and to only reduce columns *after* optimisation to ensure compatibility with Equation 3.5. Alternatively, one can optimise a partial candidate set, i.e. a

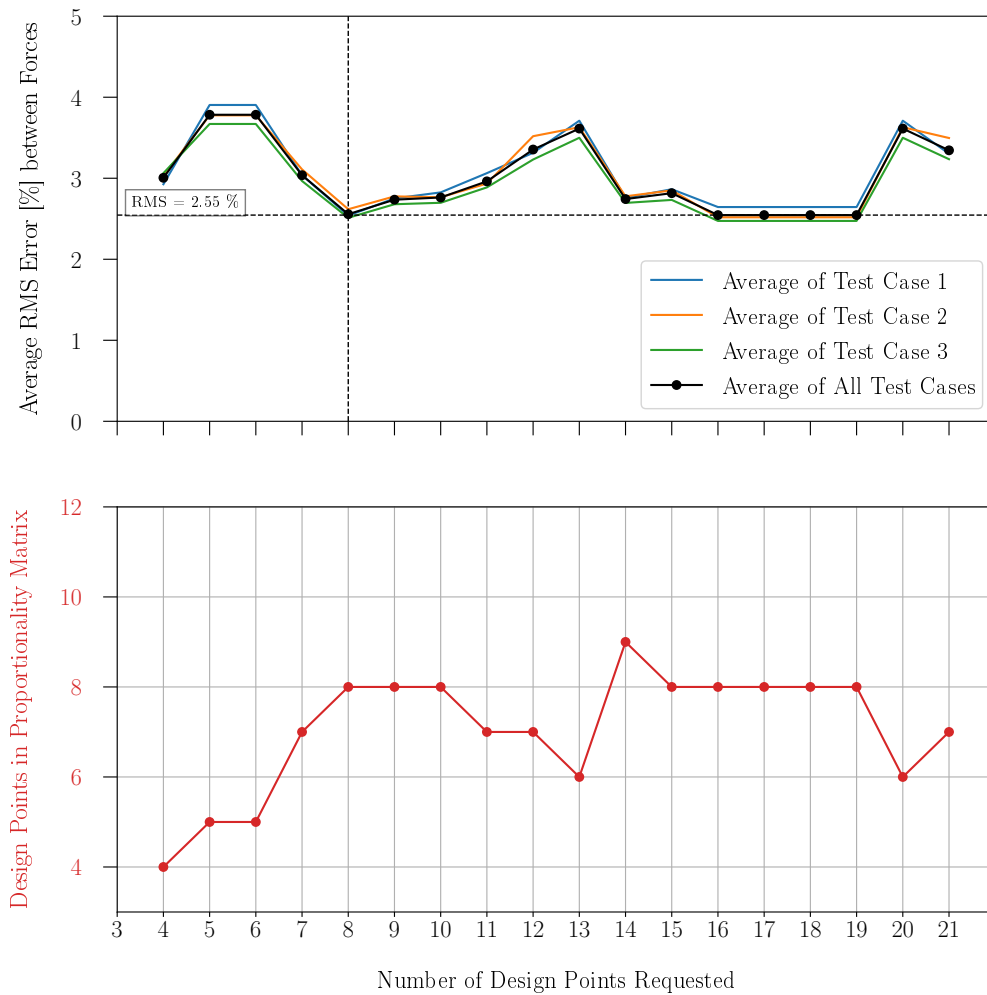


Figure 7.5: The effect of the number of design points (i.e. strain gauges) on the calculated RMS error of reconstructed loads with only distinct points in the proportionality matrix.

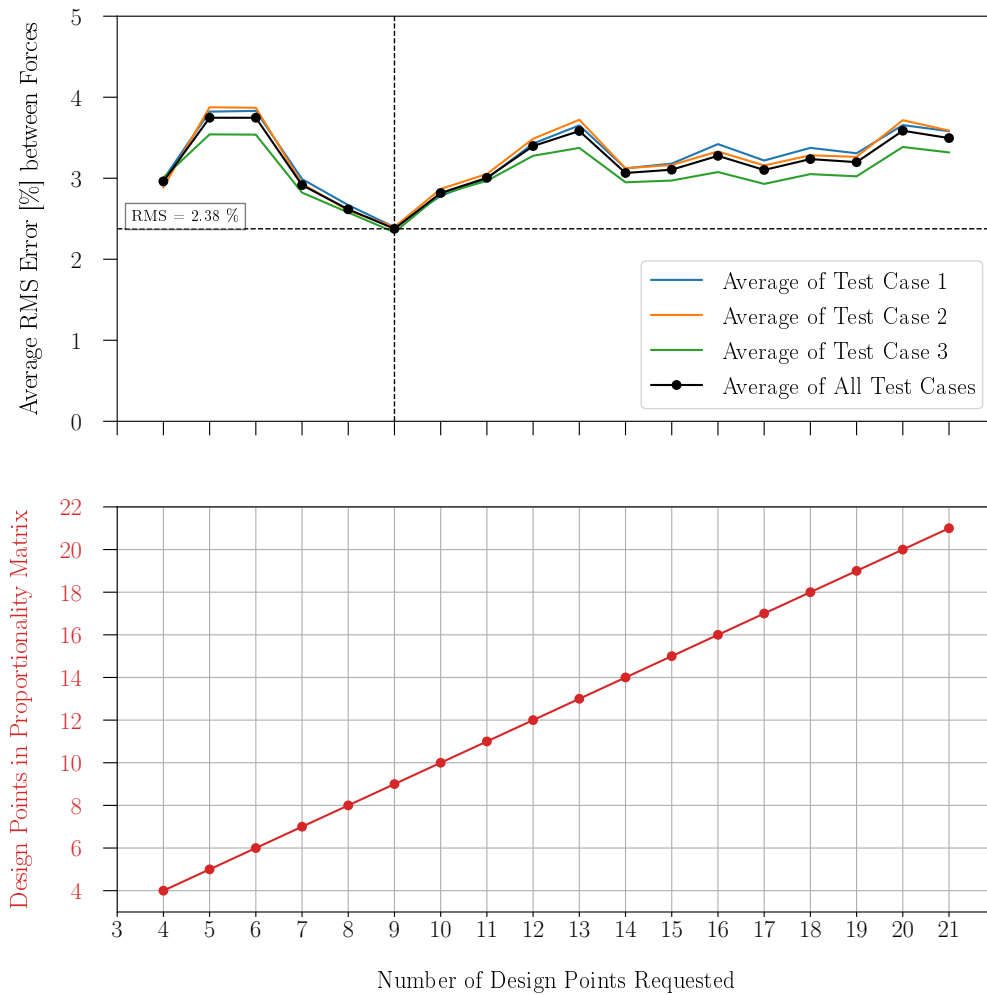


Figure 7.6: The effect of the number of design points (i.e. strain gauges) on the calculated RMS error of reconstructed loads with duplicate points in the proportionality matrix.



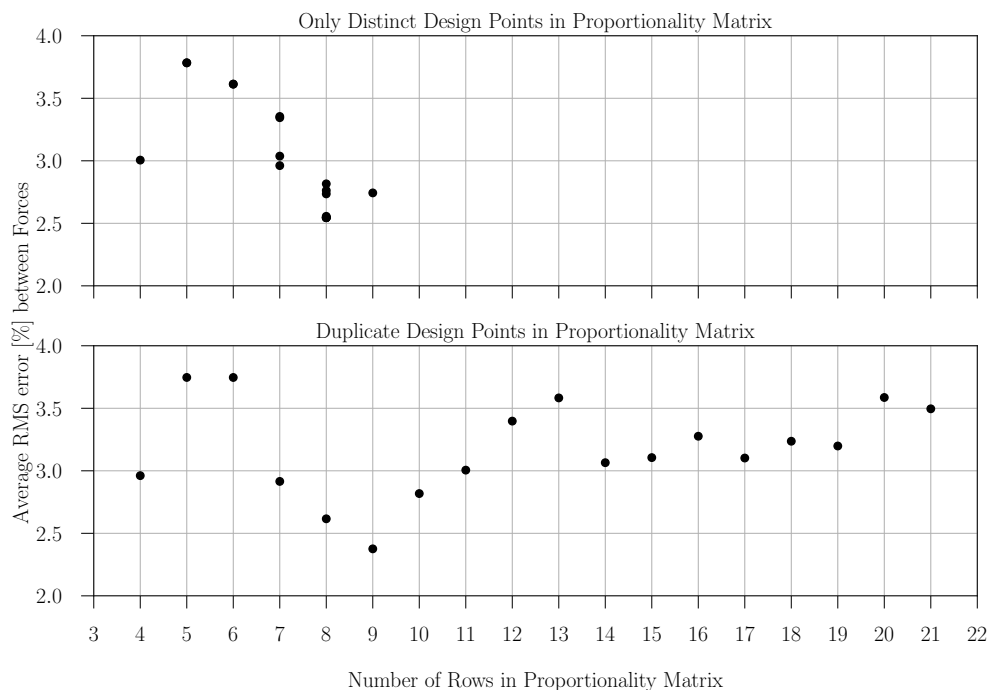


Figure 7.7: The effect of the number of design points in the proportionality matrix on the calculated RMS error.

reduced three-column set. Similarly, the model in Figure 7.3 contains a set of four loads, yet in Test Cases 4 to 9 only a subset of these loads are imposed.

Three different optimisation methods are illustrated in Figure 7.8. The first method optimises the full candidate set, and the columns of the output matrix are reduced to the proportionality matrix, the second method optimises a partial candidate set, and the last method performs a double optimisation where the full candidate set is optimised, followed by the partial optimisation of the consequent design matrix. The resultant proportionality matrices will be used to reconstruct the loads with a least-squares estimate. It is expected that the partial optimisation method will be the best performer, since it optimises a candidate set without breaking the D-optimality criterion. Both the full and double optimisation methods add an extra variable to the candidate set that changes the actual mathematical model in question. However, if one chooses the partial or double optimisation method, there is the potential for having different sets of strain gauges for each load case, which is not practical.

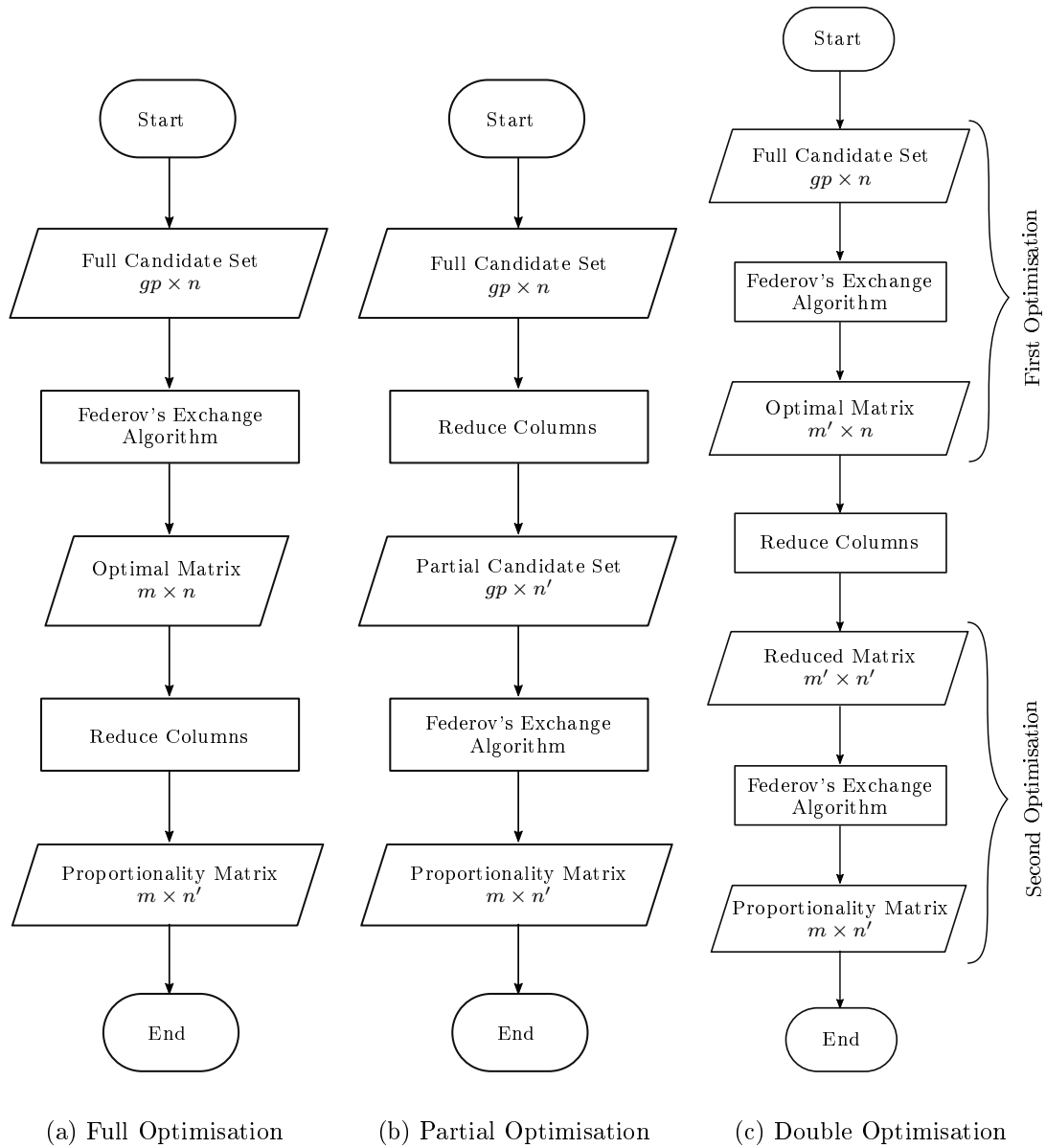


Figure 7.8: Candidate set optimisation techniques

The three optimisation methods will be applied to the test cases in Figures 7.9, and the performance of each method will be investigated and compared in the following text. Based on the findings in Section 7.1, only unique design points will be used throughout these optimisation processes as well as an error induced strain vector, explained in Equation 7.1, for the force calculations. It should be noted that the minimum number of design points that can be included in the proportionality matrix depends on the number of columns in the candidate set *before* candidate set reduction (Miller and Nguyen, 1994).

Test Cases 4 to 9 can be considered sub-loading conditions of Test Cases 1 to 3. As mentioned, the sequence in which unit-loads are applied to the unit FE model will dictate the order of the columns in the candidate set and, consequently, the columns in the design (or proportionality) matrix. For example, in Test Case 4 there is no load at location D - i.e. the load at this location equals zero - thus whenever the columns of either the candidate set or matrix need to be reduced (see Figure 7.8), the fourth column will be removed. Similarly, for Test Case 6, the first column will be removed during column reduction.

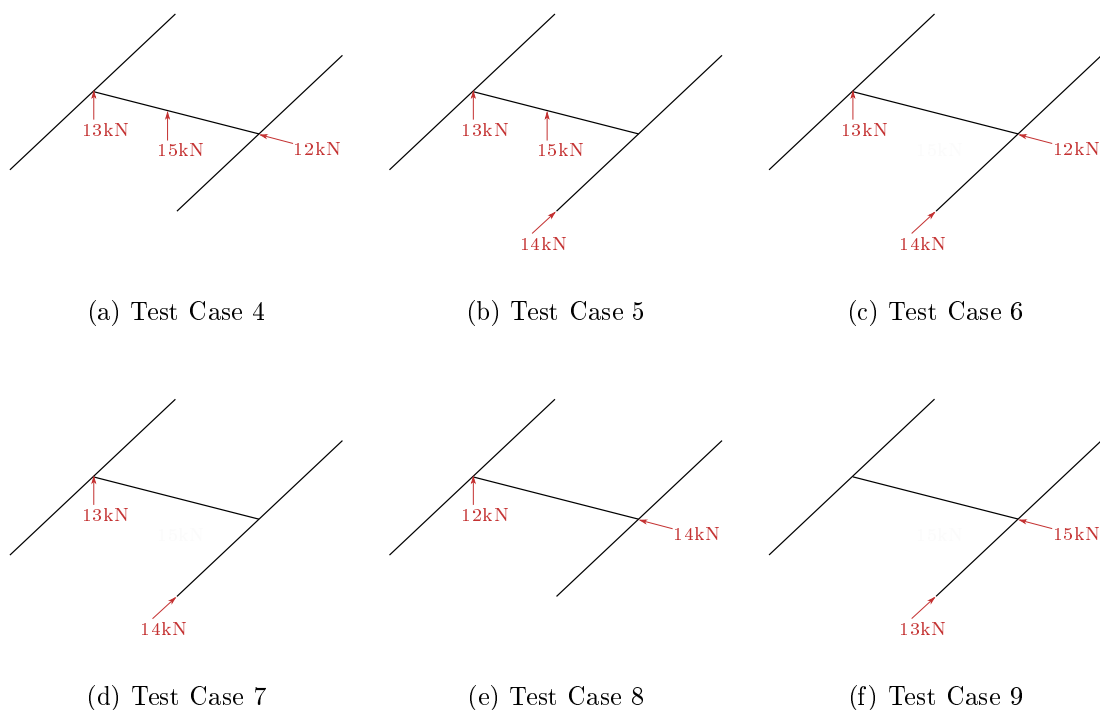


Figure 7.9: Test cases for investigating how various optimisation techniques influence load reconstruction.

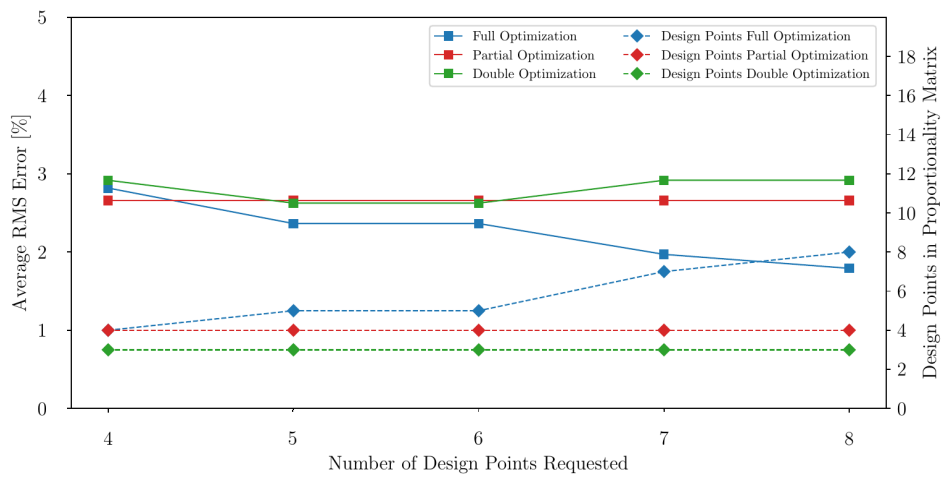
The different methods are compared in Figures 7.10 and 7.11. The full optimisation method resulted in the lowest average RMS error, except for Test Cases 6 and 9, even though it was expected that the partial optimisation method would outperform the other methods. It can be due to the ability of the optimisation algorithm to find more distinct design points when optimising the full candidate set, as opposed to the other candidate sets. It is also clear from all plots that the average RMS error decreased as the number of distinct design points in the proportionality matrix increased, except for Test Case 6 and 9. The partial and double optimisation methods failed to increasingly find distinct design points even though the request for more increased.

### 7.3 Summary

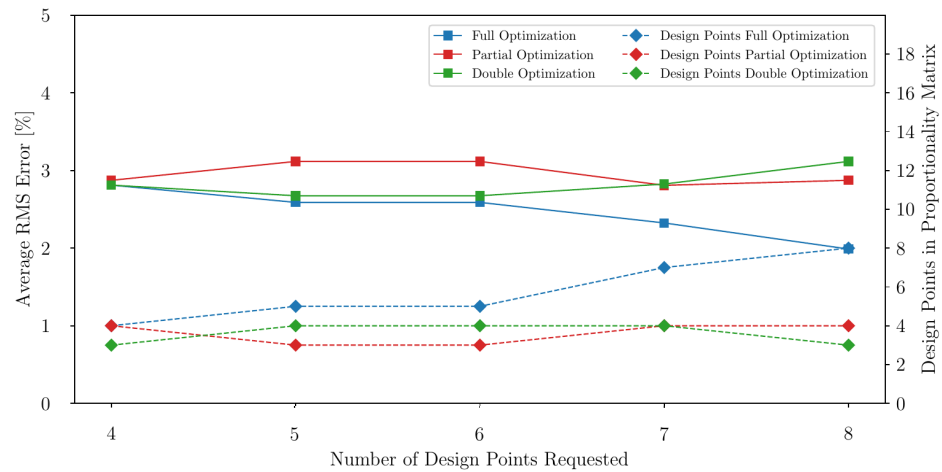
From Test Cases 1 to 3 it was found that only considering distinct design points in the proportionality matrix, is sufficient for load reconstruction. Then, it was confirmed that smaller RMS errors are calculated if the number of distinct design points in the proportionality matrix increased, however, the optimal number of design points, for this particular example, equalled double the amount of columns in the candidate set, i.e.  $m = 2n = 8$  even though nine distinct points were found. Ultimately, eight strain gauges should be mounted for the particular model in Figure 7.3.

It can be deduced from Section 7.2 that the full optimisation method may be used to determine which design points to include in the proportionality matrices. This implies that only one candidate set needs to be optimised, thus less computational effort is required. Also, Test Cases 4 to 9 will all have the same design points, and thus only a single set of strain gauges can be mounted to reconstruct multiple test cases. Ultimately, choosing the full optimisation method decreases both the computational and physical effort for performing load reconstruction. However, it is worth noting that actual locations and orientations of gauges were not investigated. There is thus the possibility that the design points which the algorithm selected, are not conducive for practically mounting gauges.

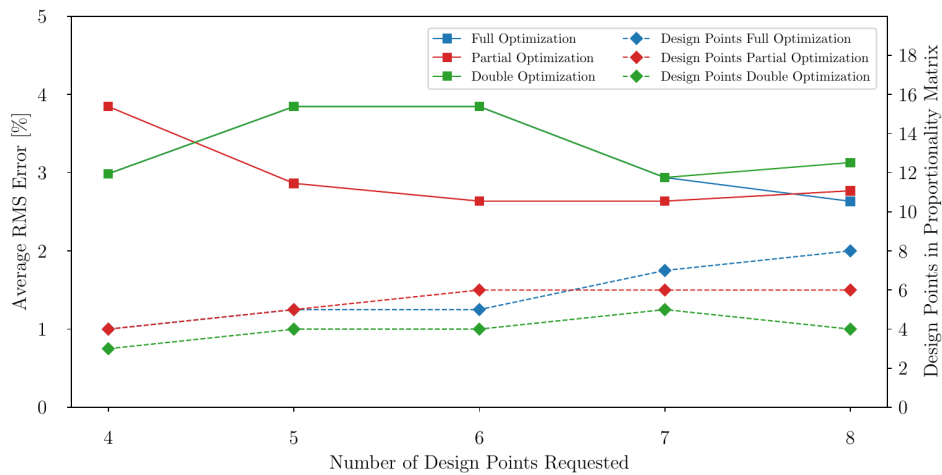
Conclusively, even though the full optimisation method is preferred, all three methods seem to work adequately. It is thus advised that the analyst run all three methods and select the most practical set of results. This will be demonstrated in Chapter 8.



(a) Test Case 4

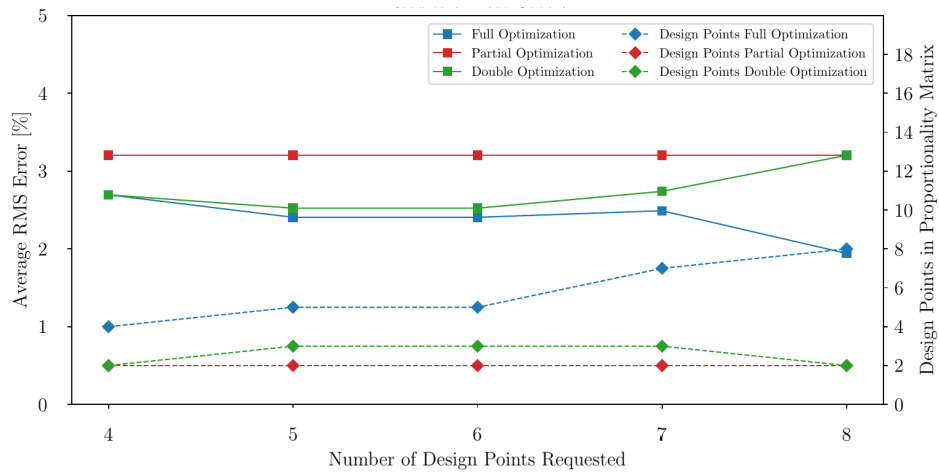


(b) Test Case 5

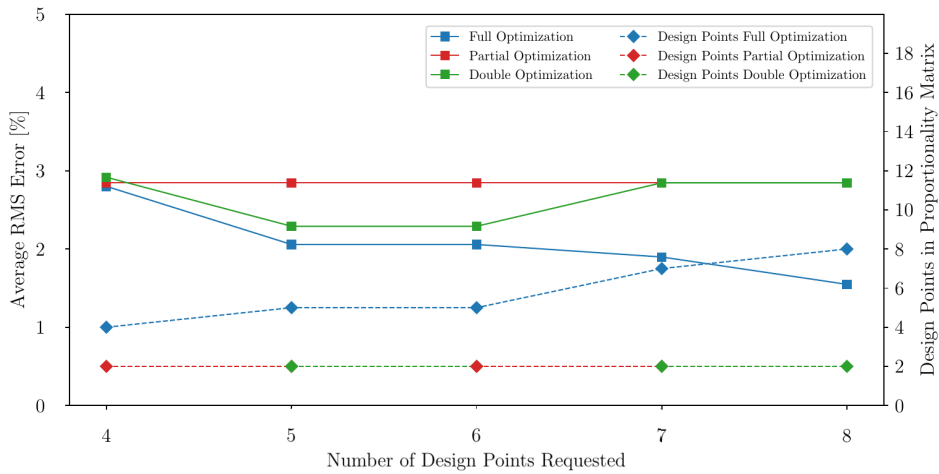


(c) Test Case 6

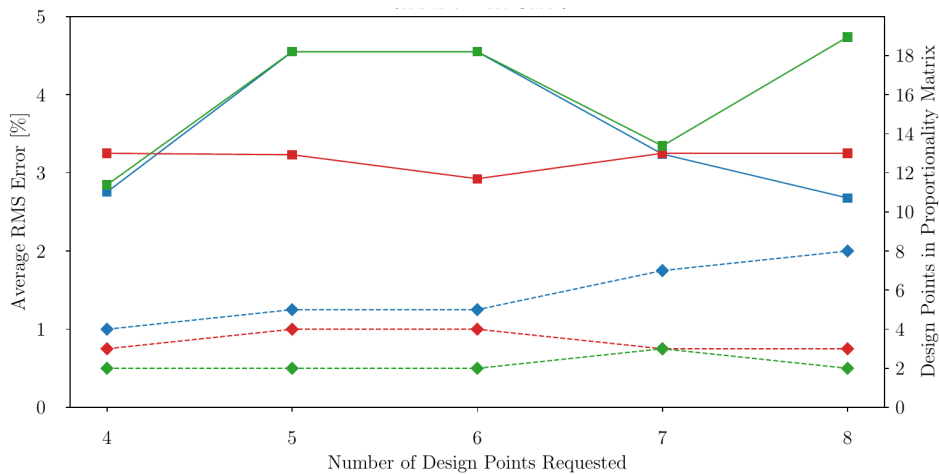
Figure 7.10: Effect of various optimisation methods on the reconstruction of loads in Test Cases 4 to 6.



(a) Test Case 7



(b) Test Case 8



(c) Test Case 9

Figure 7.11: Effect of various optimisation methods on the reconstruction of loads in Test Cases 7 to 9.

## Chapter 8

# Experimental Implementation

The numerical implementation of the various software and the considerations made concerning optimising different candidate sets were investigated in the previous chapters. This chapter will incorporate all these aspects into an actual static load reconstruction test. A bogie was not available for testing; thus, it was decided to use a representative, but a geometrically simplified structure where loads were applied by suspending weights (see Figure 8.1). The strain response was measured with uni-directional electrical resistant strain gauges, and the ability of the technique to reconstruct multiple loads was investigated.

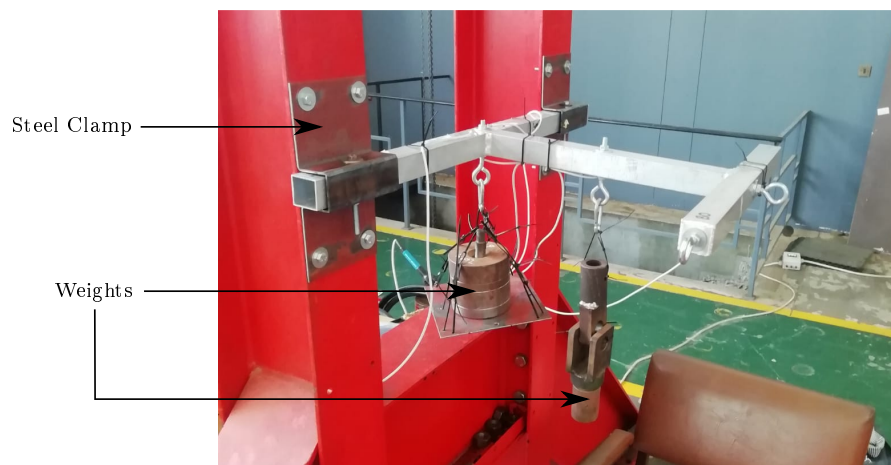


Figure 8.1: Physical setup of multiple load reconstruction experiment. This specific image corresponds to the setup for Load Case 3

Geometrical mid-planes meshed with 2D elements were used to model the structure numerically. Washers were inserted between the aluminium tube and the steel clamp on all four sides; thus the translation degrees of freedom (DOF) of all nodes in the circular areas were constrained with RBE2 elements as indicated in Figure 8.2. Similarly, a single DOF was constrained on the sides of the frame. A mesh refinement was performed, welds were not modelled, and the default material properties for an aluminium alloy in the FE pre-processor was used.

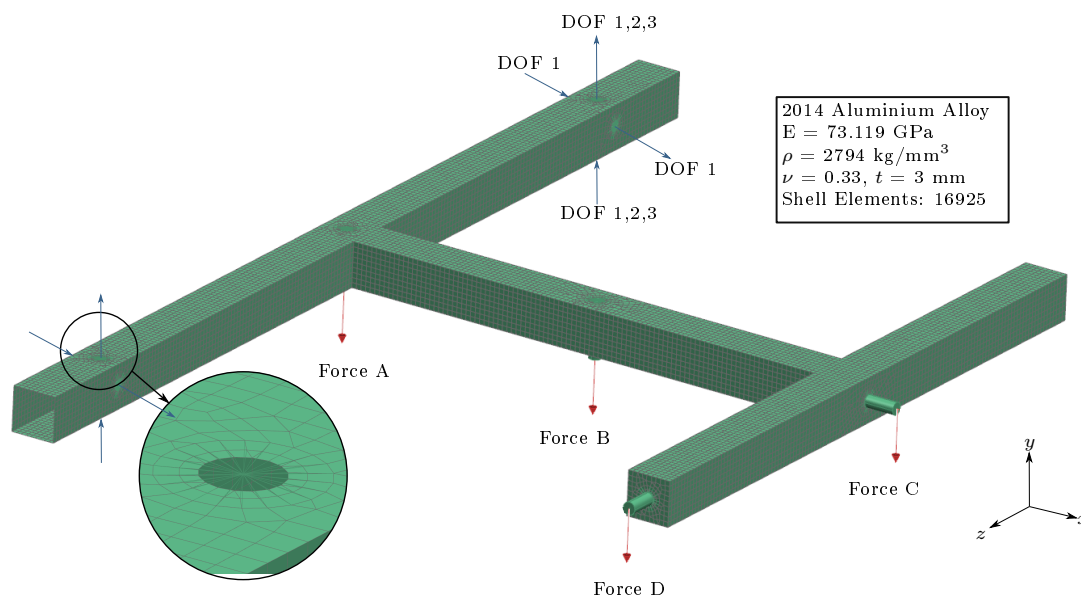


Figure 8.2: Finite-element (FE) model of the experimental setup for the reconstruction of multiple statically applied loads.

## 8.1 Gauge Locations and Orientations

The optimal candidate points for the unfiltered FE model, i.e. the candidate set that consist of all 2D elements (Candidate Set 1), were determined first. The user requested an initial number of four design points and sequentially increased the demand; the resultant optimal candidate points are summarised in Table D.1 for each number of design points requested. Ultimately, a consolidated total of 14 unique gauge locations and orientations combinations were found, which are highlighted in Figure 8.3. The algorithm selected elements that are either inaccessible due to the presence of a washer; or at sharp edges where it is challenging to glue gauges.



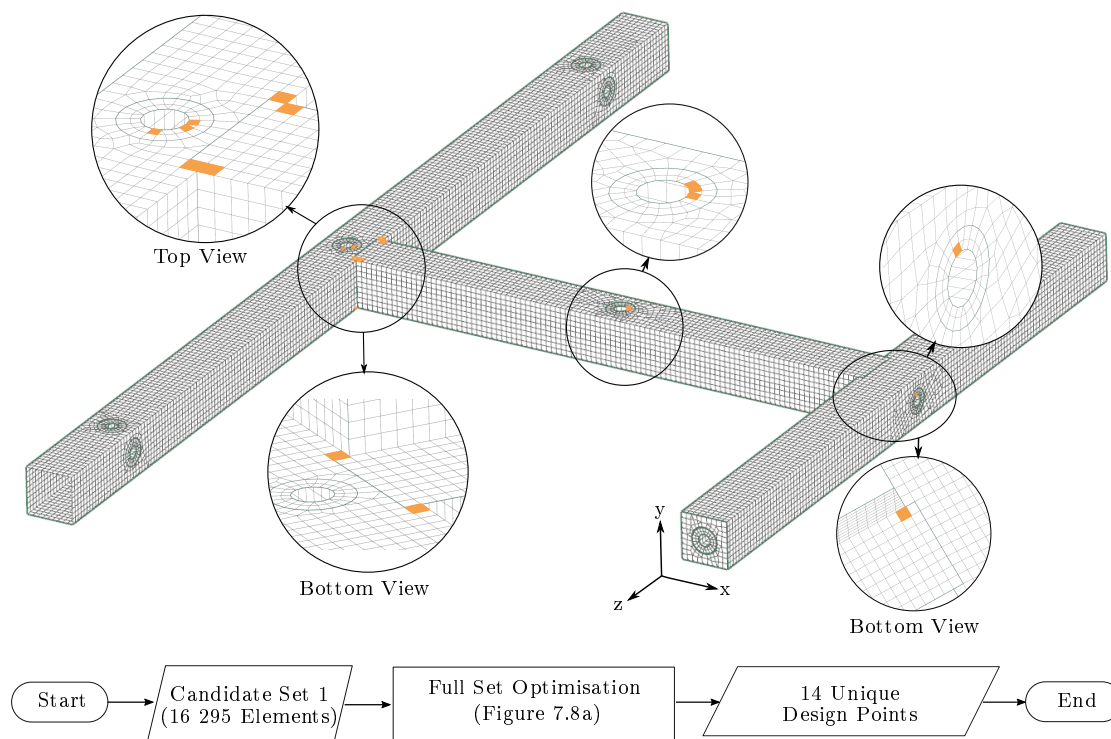


Figure 8.3: Optimal candidate points from unfiltered Candidate Set 1 using the full optimisation method. The user requested an initial number of four design points and subsequently increased the demand. 14 different gauge location-orientation combinations were obtained.

Next, the respective structural and strain filters were applied. The strain response of the unit-load model is not sufficient for implementing the strain filters; thus, the response of the respective load cases had to be obtained with approximate force magnitudes. No elements must be removed from the FE solution set before this stage, since the Strain Gradient filter is an outlier based algorithm which is influenced by the total number of data points within the population. One should also mention that for the Strain Gradient filter specifically, scaled values of the applied forces can be assumed. For example, it is presumed that weights of 8 kg and 4 kg will be suspended at Forces C and D. The same outliers will be detected by the Strain Gradient filter if loads with magnitudes 4 kg and 2 kg were assigned, as opposed to loads with magnitudes 8 kg and 4 kg, to Forces C and D. It is only important for the loads to be accurately approximated relative to one another. If the forces are linearly scaled, the strain data will be scaled accordingly, and the same outliers will be detected. The load cases with assumed magnitudes are shown in Figures 8.4a, 8.4c & 8.4e and the elements identified by the Strain Gradient filter are shown in Figures 8.4b, 8.4d & 8.4f. It is observed that the filter selected elements at sharp edges and at the areas where loads and constraints are applied.

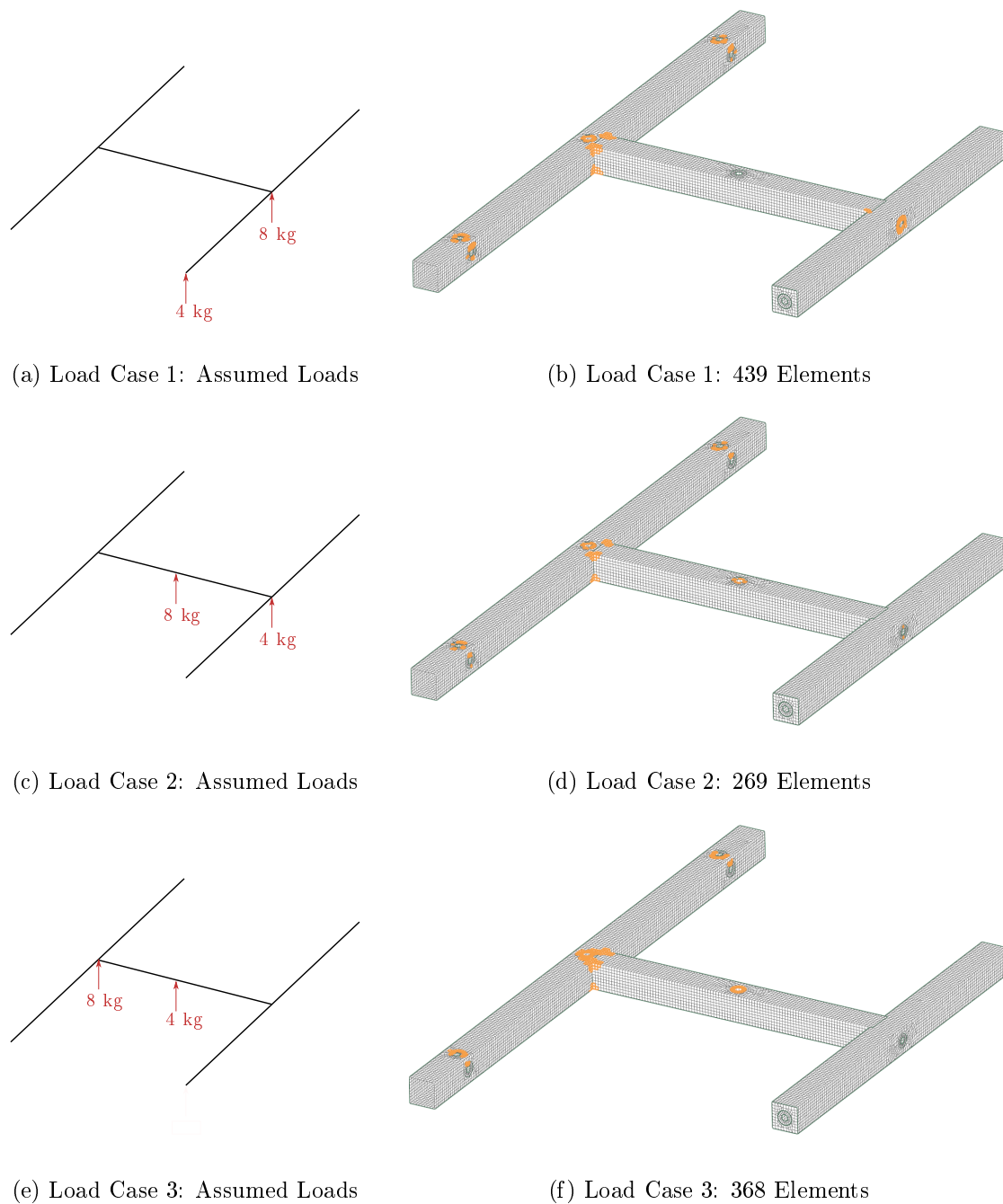


Figure 8.4: Assumed force magnitudes of load cases investigated during experimental testing and used for strain gradient filtering. The orange elements are the elements selected for removal by the Strain Gradient filter.

The elements in *blue* in Figure 8.5 were selected by the Open, Sharp Edges and Triangular Elements filters with default settings, as shown in Table 5.3. The elements in *magenta* were selected by the analyst based on the knowledge of how the frame will be attached to the support structure, how it was assembled and how the forces will be applied with additional clearance for the welds. All elements highlighted in Figures 8.4 and 8.5 were removed from Candidate Set 1. The resultant filtered set, which excludes all these selected elements, i.e. Candidate Set 2, now only consist of 9091 elements.

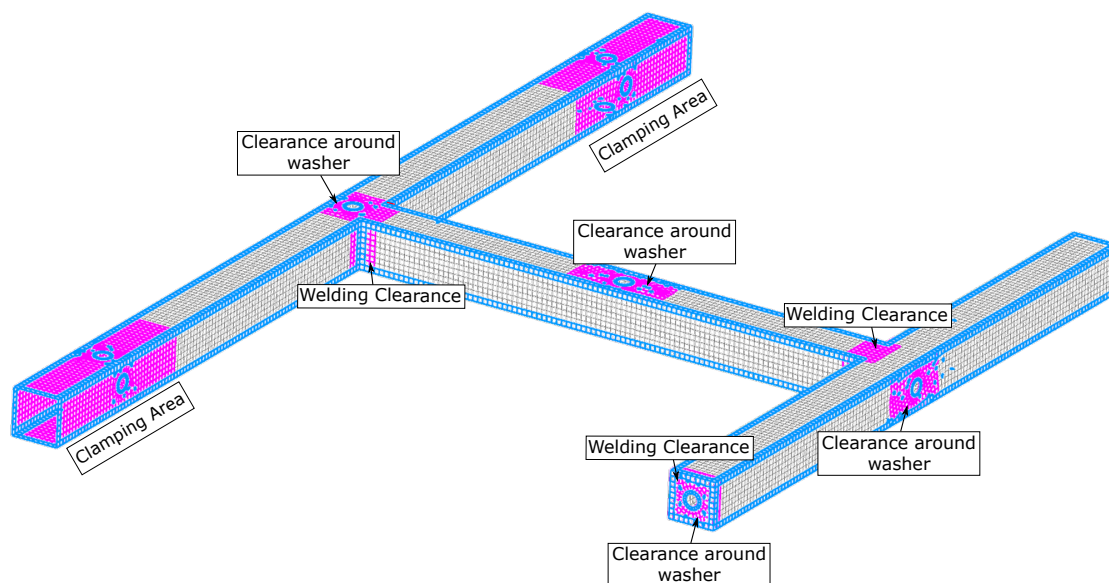
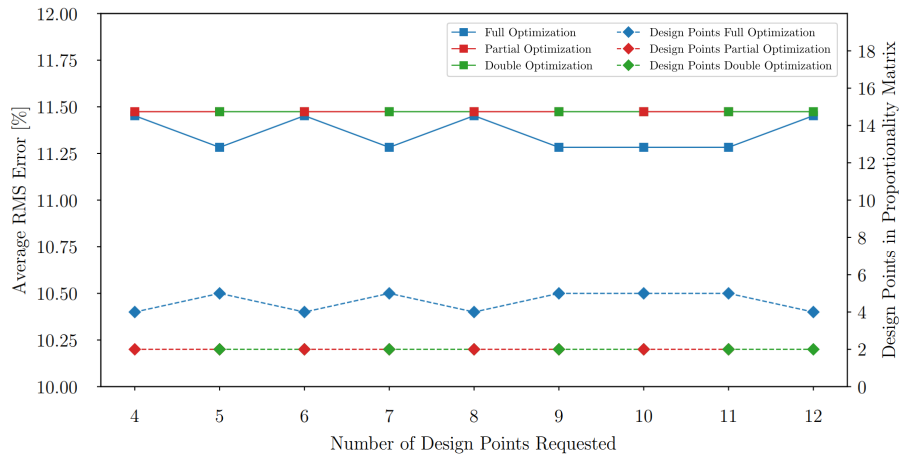
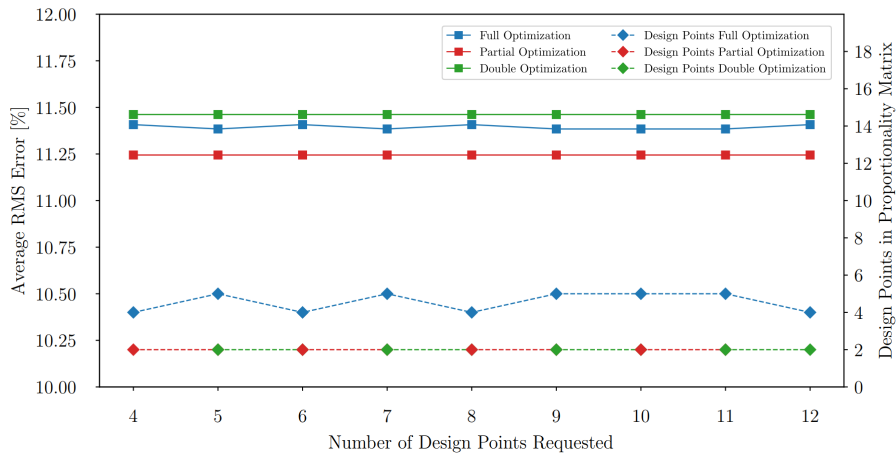


Figure 8.5: Elements identified by analyst and structural filters that should be removed from the unfiltered FE model (Candidate Set 1).

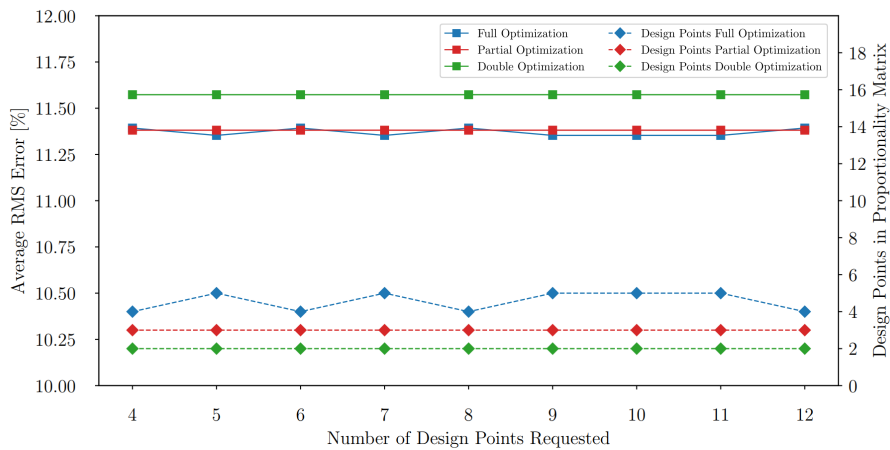
It was concluded in Chapter 7 that more candidate points in the design matrix result in better load reconstruction. It was also found that all three optimisation methods had satisfactory results. Ultimately, the method that finds the most distinct design points will be preferred, provided that it is physically feasible to mount strain gauges at the designated design points. Yet, it was thought necessary to repeat the process utilised in Section 7.2 with the assumed load cases in Figure 8.4 on Candidate Set 2, for which the results are shown in Figure 8.6.



(a) Load Case 1



(b) Load Case 2



(c) Load Case 3

Figure 8.6: Effect of various optimisation methods on the reconstruction of load cases in Figures 8.4a, 8.4c & 8.4e. The graphs show the calculated RMS errors after loads were reconstructed, as well as the unique candidate points in the design matrix.

The full optimisation method outperformed the partial and double optimisation methods, except for Load Case 2, due to its ability to find more distinct candidate points for the design (or proportionality) matrix. Noteworthy is the ability of the partial optimisation method to consistently outperform the double optimisation method. Furthermore, the minimum RMS error corresponded to a design matrix with five candidate points, which are shown in Figure 8.7, with the corresponding orientations indicated with arrows and in brackets. It was deemed feasible to mount strain gauges at each of these locations and orientations. The user should choose the optimisation method that finds the most design points. Next, the practicality of mounting strain gauge at the output candidate points should be confirmed. If all methods manage to find the same number of design points, and there are no practical concerns, the full optimisation method is favoured, followed by the partial optimisation method.

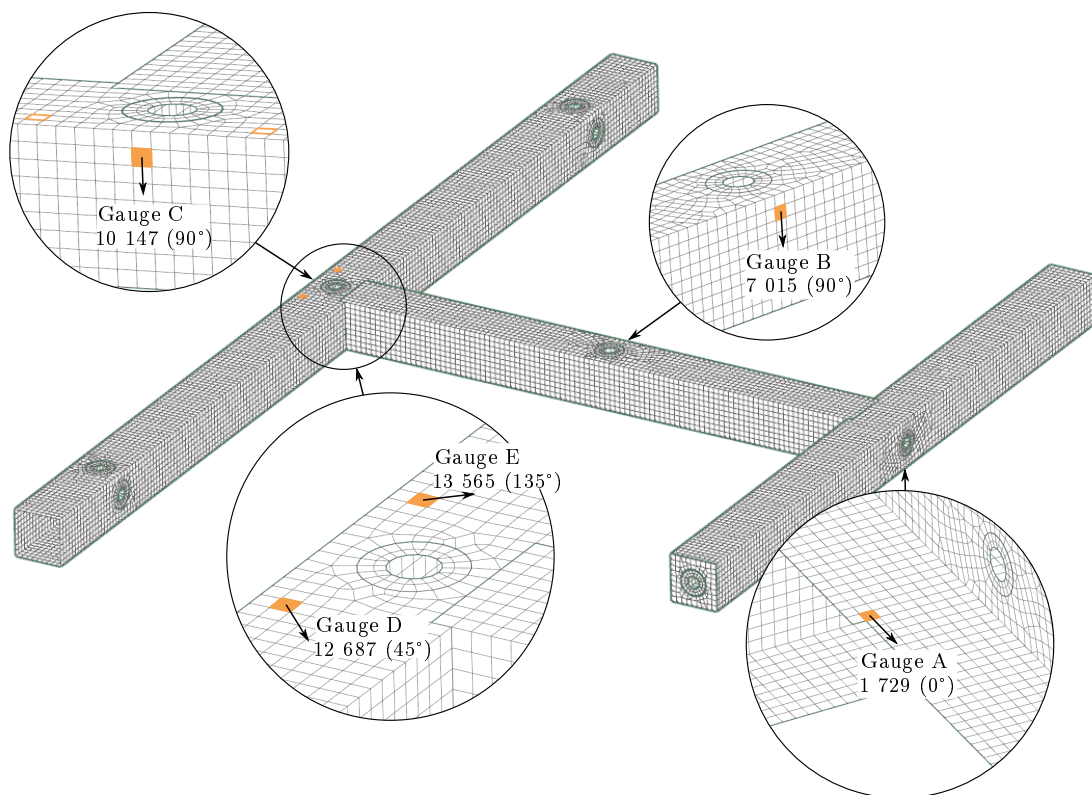


Figure 8.7: Optimal candidate points from Candidate Set 2, using the full optimisation method. Five design points were requested by the user to obtain these candidate points, based on the conclusions made from Figure 8.6.

## 8.2 Experimental Setup

The strain responses were measured with uni-directional electrical resistant ( $350 \Omega$ ) strain gauges in quarter-bridge configurations. Gauges were mounted at the locations and orientations as indicated in Figure 8.7. However, the size of the welds was underestimated when areas were excluded from the candidate set (Figure 8.5). In Figure 8.8 it is shown where the strain gauge was meant to be mounted (on Element 1 729) and where it was actually placed. The strain gradient filter did not exclude this area from the candidate set; thus, this shift was considered not to be a problem. It should be noted that the welds were not modelled; thus, the residual stresses and strains are not accounted for in the FE model.

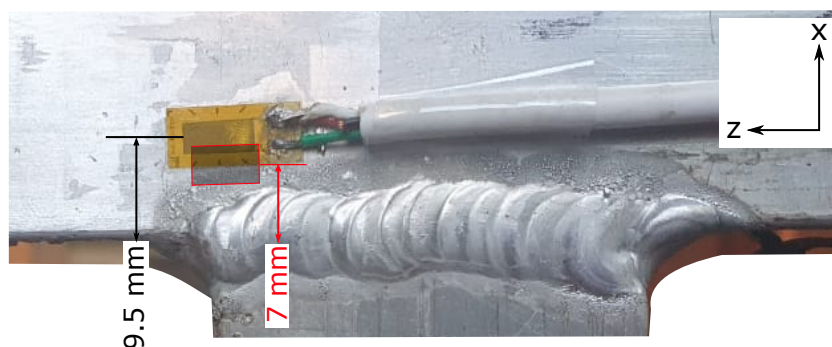


Figure 8.8: Actual placement of Gauge A relative to Element 1 729 (red square).

Weights of 3.609 kg and 8.435 kg were suspended from the aluminium frame similarly as indicated in Figures 8.4a, 8.4c & 8.4e. For data capturing, a QuantumX M1615b data acquisition (DAQ) system was used to record the measured values at a sample rate of 5 Hz. The weights were suspended for 60 seconds to allow the system to stabilise; this process was repeated five consecutive times. A coefficient of variance (COV), which is the ratio of the standard deviation to the average, was calculated and is commonly used to indicate the level of dispersion around the average. The purpose of calculating the COV was to serve as an indication of the repeatability of the measured values. Wili *et al.* (2017) studied the effective yield properties of human trabecular bone and the COV was similarly used on the strain measurements. 44.4 % of the test values (8 out of the 18 tests) yielded a COV of less than 10 % and 33.3 % of the test values yielded a COV between 10 % and 20 %. According to Ebrahimi (2018), an acceptable COV is dependent on the kind of research, but that a  $COV \leq 10 \%$  is typically considered as good, a COV between 10 % and 30 % is satisfactory and  $COV \geq 30 \%$  is unacceptable. Based on the information from Wili *et al.* (2017) and Ebrahimi (2018), all strain measurements for which a COV of less than 10 % are calculated, will be accepted.

### 8.3 Measured Strain Values

The measured strain results are summarised in Table 8.1 and detailed in Table D.2, Table D.3 and Table D.4. An unacceptable COV value of 200.3 % was calculated for Gauge A in Load Case 3. It should be noted that the strain value is close to the minimum measuring capability of these strain gauges ( $1 \times 10^{-9}$  mm/mm) and that the analyst failed to verify and exclude any elements from the candidate set with strain values below this threshold. Based on these realisations, it is expected that the gauge will measure incorrect values and consequently yield a high COV.

Table 8.1: Experimentally measured strain values

	Load Case 1		Load Case 2		Load Case 3	
	Strain [mm/mm]	% COV	Strain [mm/mm]	% COV	Strain [mm/mm]	% COV
Gauge A	$-6.53 \times 10^{-05}$	-4.1 %	$-7.23 \times 10^{-06}$	-3.1 %	$9.66 \times 10^{-08}$	<b>200.3 %</b>
Gauge B	$-3.28 \times 10^{-05}$	-0.7 %	$5.20 \times 10^{-05}$	4.7 %	$1.07 \times 10^{-05}$	2.8 %
Gauge C	$-4.98 \times 10^{-04}$	-0.1 %	$-2.88 \times 10^{-04}$	-0.1 %	$6.14 \times 10^{-05}$	3.5 %
Gauge D	$-4.16 \times 10^{-04}$	-0.2 %	$-2.66 \times 10^{-04}$	-0.4 %	$-1.03 \times 10^{-04}$	-2.3 %
Gauge E	$-3.69 \times 10^{-04}$	-0.3 %	$-2.41 \times 10^{-04}$	-0.6 %	$-1.04 \times 10^{-04}$	-1.1 %

### 8.4 Actual Gauge Locations

A strain gauge measures an average strain value over the surface area covered by the active grid length. It is possible that the physical location of the gauge might be off due to measuring difficulties encountered during test setup as for Gauge A in Section 8.2. The actual location of the active grid of each strain gauge was measured and the corresponding finite-elements were determined. Then, a percentage surface coverage was calculated if a gauge happens to cover more than one element; this value indicates which fraction of the overall active grid falls onto a specific element. The results are shown in Figures 8.9 and 8.10 and Tables 8.2 and 8.3, as well as in Figures D.1 to D.3 and Tables D.5 to D.7.

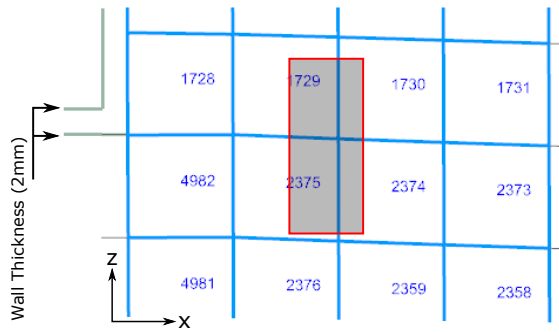


Figure 8.9: Location of Gauge A

Table 8.2: Surface coverage of Gauge A

Element	% Coverage
1729	30.2 %
1730	15.6 %
2374	18.4 %
2375	35.9 %

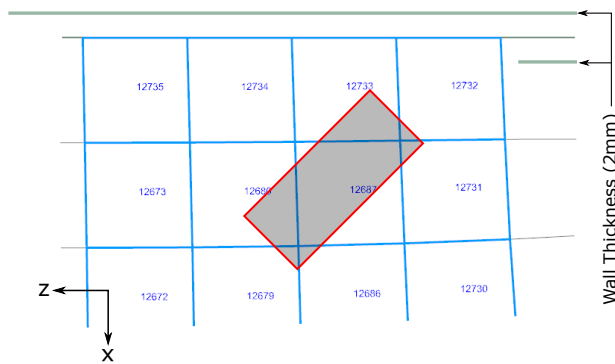


Figure 8.10: Location of Gauge D

Table 8.3: Surface coverage of Gauge D

Element	% Coverage
12679	18.1 %
12680	1.8 %
12686	19.1 %
12687	54.9 %
12731	2.4 %
12732	2.0 %
12733	1.9 %

## 8.5 Load Reconstruction

The proportionality (or design) matrix describes the relationship between the input loading and output strain response and at this point there are different variations of this matrix that can be used for load reconstruction. First of all, there is the option of using the original design matrix obtained in Section 8.1, where each row corresponds to an optimal candidate point obtained from the full optimisation method. This matrix is shown in Figure 8.11. It was mentioned in Section 3.2.1 that component  $c_{ij}$  in the proportionality matrix, is the sensitivity of gauge  $i$  to load  $j$ . If the first row in Figure 8.11 is inspected, it is observed that Element 1729 is the most sensitive to Force D and least sensitive to Force A. This knowledge can be used in future studies to compare the elements selected by experienced technicians to the location selected by the algorithm.



It was pointed out that the gauges do not necessarily line up with these initial candidate points and, for this particular mesh size, the gauge is actually mounted over several finite-elements. Subsequently, it was decided to create a variation of the design matrix, where each row consist of the averaged candidate points of all elements onto which the strain gauge is mounted. This matrix is shown in Figure 8.12. However, the strain gauge does not equally cover all elements (Section 8.3) and a weighted average should rather be calculated. This matrix is shown in Figure 8.13. The data used to construct the proportionality matrices in Figures 8.12 and 8.13 are provided in Sections D.4 and D.5.

$$\begin{array}{c}
 \begin{array}{l}
 (1729, 0^\circ) \longrightarrow \\
 (7015, 90^\circ) \longrightarrow \\
 (10147, 90^\circ) \longrightarrow \\
 (12687, 45^\circ) \longrightarrow \\
 (13565, 135^\circ) \longrightarrow
 \end{array}
 \begin{array}{cccc}
 f_A & f_B & f_C & f_D \\
 \downarrow & \downarrow & \downarrow & \downarrow \\
 \begin{bmatrix}
 -2.44 \times 10^{-13} & -1.23 \times 10^{-10} & -4.49 \times 10^{-06} & -5.25 \times 10^{-05} \\
 -8.83 \times 10^{-12} & 8.54 \times 10^{-06} & -2.56 \times 10^{-06} & -2.11 \times 10^{-06} \\
 1.01 \times 10^{-05} & -1.29 \times 10^{-05} & -3.33 \times 10^{-05} & -2.92 \times 10^{-05} \\
 -5.45 \times 10^{-06} & -1.55 \times 10^{-05} & -3.67 \times 10^{-05} & -2.61 \times 10^{-05} \\
 -5.42 \times 10^{-06} & -1.55 \times 10^{-05} & -3.65 \times 10^{-05} & -3.84 \times 10^{-05}
 \end{bmatrix}
 \end{array}
 \begin{array}{c}
 \left. \begin{array}{c} \\ \\ \\ \\ \end{array} \right\} = \begin{array}{c} \left. \begin{array}{c} \varepsilon_A \\ \varepsilon_B \\ \varepsilon_C \\ \varepsilon_D \\ \varepsilon_E \end{array} \right\} \\
 \uparrow \\
 \text{Load Vector}
 \end{array}
 \end{array}
 \end{array}$$

Figure 8.11: Expanded equation that describes the relationship between the input loading and measured strains, with only the original optimal candidate points included in the proportionality (design) matrix.

$$\begin{array}{c}
 \begin{array}{l}
 \text{Avg. Point for Gauge A} \longrightarrow \\
 \text{Avg. Point for Gauge B} \longrightarrow \\
 \text{Avg. Point for Gauge C} \longrightarrow \\
 \text{Avg. Point for Gauge D} \longrightarrow \\
 \text{Avg. Point for Gauge E} \longrightarrow
 \end{array}
 \begin{array}{cccc}
 f_A & f_B & f_C & f_D \\
 \downarrow & \downarrow & \downarrow & \downarrow \\
 \begin{bmatrix}
 -5.34 \times 10^{-13} & -4.91 \times 10^{-11} & -2.86 \times 10^{-06} & -4.61 \times 10^{-05} \\
 -1.04 \times 10^{-11} & 8.31 \times 10^{-06} & -2.48 \times 10^{-06} & -2.35 \times 10^{-06} \\
 1.07 \times 10^{-05} & -1.28 \times 10^{-05} & -3.30 \times 10^{-05} & -2.89 \times 10^{-05} \\
 -4.82 \times 10^{-06} & -1.54 \times 10^{-05} & -3.63 \times 10^{-05} & -2.61 \times 10^{-05} \\
 -5.58 \times 10^{-06} & -1.47 \times 10^{-05} & -3.46 \times 10^{-05} & -3.58 \times 10^{-05}
 \end{bmatrix}
 \end{array}
 \begin{array}{c}
 \left. \begin{array}{c} \\ \\ \\ \\ \end{array} \right\} = \begin{array}{c} \left. \begin{array}{c} \varepsilon_A \\ \varepsilon_B \\ \varepsilon_C \\ \varepsilon_D \\ \varepsilon_E \end{array} \right\} \\
 \uparrow \\
 \text{Load Vector}
 \end{array}
 \end{array}
 \end{array}$$

Figure 8.12: Expanded equation that describes the relationship between the input loading and measured strains, with only averaged candidate points included in the proportionality (design) matrix.

$$\begin{array}{r}
 \begin{array}{l}
 \text{Weight Avg. for Gauge A} \\
 \text{Weight Avg. for Gauge B} \\
 \text{Weight Avg. for Gauge C} \\
 \text{Weight Avg. for Gauge D} \\
 \text{Weight Avg. for Gauge E}
 \end{array}
 \left[ \begin{array}{cccc}
 \begin{array}{c} f_A \\ \downarrow \\ -5.35 \times 10^{-13} \end{array} & \begin{array}{c} f_B \\ \downarrow \\ -4.74 \times 10^{-11} \end{array} & \begin{array}{c} f_C \\ \downarrow \\ -2.78 \times 10^{-06} \end{array} & \begin{array}{c} f_D \\ \downarrow \\ -4.57 \times 10^{-05} \end{array} \\
 \begin{array}{c} -1.05 \times 10^{-11} \\ 8.09 \times 10^{-06} \\ -2.47 \times 10^{-06} \\ -2.40 \times 10^{-06} \end{array} & \begin{array}{c} 1.19 \times 10^{-05} \\ -1.42 \times 10^{-05} \\ -3.65 \times 10^{-05} \\ -3.20 \times 10^{-05} \end{array} & \begin{array}{c} -5.24 \times 10^{-06} \\ -1.44 \times 10^{-05} \\ -3.39 \times 10^{-05} \\ -2.48 \times 10^{-05} \end{array} & \begin{array}{c} -4.58 \times 10^{-06} \\ -1.33 \times 10^{-05} \\ -3.09 \times 10^{-05} \\ -3.10 \times 10^{-05} \end{array}
 \end{array} \right] = \begin{array}{c} \text{Measured Strain Values} \\ \downarrow \\ \begin{array}{c} \varepsilon_A \\ \varepsilon_B \\ \varepsilon_C \\ \varepsilon_D \\ \varepsilon_E \end{array} \end{array}
 \end{array}$$

Load Vector

Figure 8.13: Expanded equation that describes the relationship between the input loading and measured strains, with weighted averaged candidate points included in the proportionality (design) matrix.

### 8.5.1 Load Case 1

The results of the reconstructed loads for Load Case 1 are shown in Table 8.4 and it is clear that loads were not satisfactorily reconstructed. Since the magnitude of the weights used for experimentation is known, it was decided to solve the FE model with these loads as a starting point for further investigations. First of all, the measured values are compared to the element that is mostly covered by the strain gauge. For example, the majority of Gauge B (38.6 %) is mounted on Element 7029, thus the measured strain value of Gauge B will be compared to the strain response of Element 7029. The results are summarised in Table 8.5.

Table 8.4: Results of reconstructed loads for Load Case 1

Applied Load	Original Design Matrix		Averaged Design Matrix		Weighted Averaged Design Matrix	
Force C (8.435 kg)	11.880 kg	40.84 %	11.781 kg	39.67 %	12.152 kg	44.08 %
Force D (3.609 kg)	0.108 kg	96.99 %	0.601 kg	83.35 %	0.666 kg	81.55 %
RMS Error	-	53.53 %	-	49.04 %	-	51.68 %

Table 8.5: Measured and calculated strain values for Load Case 1

	Average Measured Strains [mm/mm]	Calculated FE Strains [mm/mm]	% Difference
Gauge A & Element 2 375	$-6.53 \times 10^{-05}$	$-2.24 \times 10^{-04}$	<b>244.0 %</b>
Gauge B & Element 7 029	$-3.28 \times 10^{-05}$	$-2.95 \times 10^{-05}$	10.1 %
Gauge C & Element 10 147	$-4.98 \times 10^{-04}$	$-3.86 \times 10^{-04}$	<b>22.4 %</b>
Gauge D & Element 12 687	$-4.16 \times 10^{-04}$	$-4.04 \times 10^{-04}$	3.0 %
Gauge E & Element 13 559	$-3.69 \times 10^{-04}$	$-3.37 \times 10^{-04}$	8.9 %

An error value of 244.0 % was calculated for the strain measured by Gauge A and Element 2375. The strain values of the surrounding elements in the FE model were looked into and the results are shown in Table 8.6. A better correlation was found between the measured value and the strain calculated at Element 2372, but when compared to the position of Gauge A, it can be seen that Element 2372 is approximately 8 mm away from where the gauge is actually mounted (Figure 8.14). The scattered errors calculated for the surrounding elements is an indication of a high strain gradient in the vicinity, which was not detected by the Strain Gradient filter. This suggests that the Strain Gradient filter is not strict enough in selecting outliers. Secondly, in the introduction to this chapter, it was mentioned that the welds were not included in the FE model, which suggests that within this specific vicinity the FE model does not accurately predict the real life structure, which can lead to high discrepancies. Furthermore, an error value of 22.4 % was calculated between Gauge C and Element 10147. If strain values of the surrounding elements are compared to the strain measured by Gauge C, it can be seen in Table D.18 that an error of only 1 % is calculated between the measured strain value and Element 10146. In addition, from the matrix in Figure 8.13 it is noted that Gauges A and C are the most sensitive to Loads C and D.

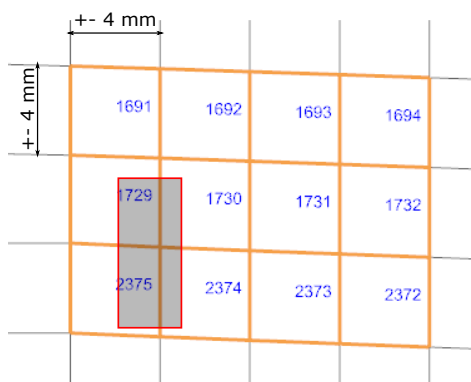


Figure 8.14: Location of Gauge A in the FE model with surrounding elements

Table 8.6: Strain values of elements surrounding Gauge A for Load Case 1.

Element	FE [mm/mm]	Measured [mm/mm]	% Error
1691	$-1.93 \times 10^{-04}$	$-6.53 \times 10^{-05}$	196 %
1729	$-2.27 \times 10^{-04}$	$-6.53 \times 10^{-05}$	248 %
2375	$-2.24 \times 10^{-04}$	$-6.53 \times 10^{-05}$	244 %
1692	$-1.45 \times 10^{-04}$	$-6.53 \times 10^{-05}$	122 %
1730	$-1.62 \times 10^{-04}$	$-6.53 \times 10^{-05}$	148 %
2374	$-1.49 \times 10^{-04}$	$-6.53 \times 10^{-05}$	128 %
1693	$-1.13 \times 10^{-04}$	$-6.53 \times 10^{-05}$	72 %
1731	$-1.14 \times 10^{-04}$	$-6.53 \times 10^{-05}$	74 %
2373	$-1.02 \times 10^{-04}$	$-6.53 \times 10^{-05}$	56 %
1694	$-8.38 \times 10^{-05}$	$-6.53 \times 10^{-05}$	28 %
1732	$-8.09 \times 10^{-05}$	$-6.53 \times 10^{-05}$	24 %
2372	$-6.80 \times 10^{-05}$	$-6.53 \times 10^{-05}$	4 %
Average Error			112 %

Xiaofeng *et al.* (n.d.) stated that the most significant source of error between the calculated and actual loads originates from the differences between the FE and actual model. It was decided to reconstruct the loads with a proportionality matrix that consists of the elements for which the smallest percentage difference was calculated, to investigate this statement made by Xiaofeng *et al.* (n.d.). In reality this will not be possible, since the magnitudes of the applied loads are not known. This ‘adapted’ proportionality matrix is shown in Figure D.4. Forces C and D were respectively reconstructed to be 8.731 kg (3.51 %) and 3.623 kg (0.39 %) with an RMS error of 3.23 %. In a non-experimental environment the analyst would not have the luxury of comparing the measured strains to the numerically calculated values. However, this significant improvement emphasises the importance of having a FE model that truly represents the real-life response. This correlation is the ultimate indicator for accurate load reconstruction. The effects of the strain gradient phenomenon is also actively illustrated here.

### 8.5.2 Load Case 2

The results of the reconstructed loads for Load Case 2 are shown in Table 8.7. These results are noticeably better than the loads reconstructed for Load Case 1. It is also proven that it is worth the effort to calculate the weighted averaged design matrix, since an RMS error of 12.48 % was obtained, in comparison to an 18.83 % RMS error for the averaged design matrix and an 17.96 % RMS error for the original design matrix.

Table 8.7: Results of reconstructed loads for Load Case 2

Applied Load	Original Design Matrix		Averaged Design Matrix		Weighted Averaged Design Matrix	
Force B (8.435 kg)	7.051 kg	16.41 %	7.093 kg	15.91 %	7.778 kg	7.78 %
Force C (3.609 kg)	4.503 kg	24.77 %	4.697 kg	30.15 %	4.654 kg	28.97 %
RMS Error	-	17.96 %	-	18.83 %	-	13.46 %

The difference between the numerically calculated and experimentally measured strain values were also compared, as for Load Case 1. From Table 8.8 it is seen that an error value of 48.5 % was calculated for the strain measured by Gauge A and Element 2375. The strain values of the surrounding elements in the FE model were looked into and the results are in Table D.19. A better correlation was found between the measured value and the strain calculated at Element 2374. From Table D.19 it is clear that the error values are still scattered, but that the average error in this vicinity improved (from 112 % for Load Case 1 to 64 %). This improvement in the reconstructed loads is the direct result of the more accurate correlation between real-life and FE models. Furthermore, an error value of 20.6 % was calculated between Gauge C and Element 10147. If strain values of the surrounding elements are compared to the strain value measured by Gauge C, it can be seen in Table D.20 that an error of only 3 % is calculated between the measured strain value and Element 10146.

Table 8.8: Measured strain values for Load Case 2

	Average Measured Strains [mm/mm]	Calculated FE Strains [mm/mm]	% Difference
Gauge A & Element 2 375	$-7.23 \times 10^{-06}$	$-1.07 \times 10^{-05}$	<b>48.5 %</b>
Gauge B & Element 7 029	$5.20 \times 10^{-05}$	$5.59 \times 10^{-05}$	7.5 %
Gauge C & Element 10 147	$-2.88 \times 10^{-04}$	$-2.29 \times 10^{-04}$	<b>20.6 %</b>
Gauge D & Element 12 687	$-2.66 \times 10^{-04}$	$-2.64 \times 10^{-04}$	1.1 %
Gauge E & Element 13 559	$-2.41 \times 10^{-04}$	$-2.05 \times 10^{-04}$	14.9 %

### 8.5.3 Load Case 3

A COV of 200.3 % was calculated for Gauge A in Load Case 3, due to the inability of the strain gauge to accurately measure below its minimum measuring capacity. This is confirmed by the strain values in the FE model for the elements surrounding Gauge A (see Table D.21). Since the measurements of Gauge A for Load Case 3 is unreliable, it was decided to exclude the first row of the respective proportionality

matrices. The reconstructed loads for Load Case 3, with these reduced matrices, are shown in Table 8.9. Once again, the effort of calculating the weighted averaged design matrix paid off, since an RMS error of 15.26 % was calculated in comparison to an 19.13 % RMS error for the averaged design matrix and an 19.49 % RMS error for the original design matrix. The measured strain values were compared to the numerically calculated strains and the results are shown in Table 8.10. It was satisfying to note that even though three of the four gauges had a percentage error greater than 20 %, the loads were still reconstructed with an RMS error of only 15.26 %.

Table 8.9: Results of reconstructed loads for Load Case 3

Applied Load	Original Design Matrix		Averaged Design Matrix		Weighted Averaged Design Matrix	
Force A (8.435 kg)	10.474 kg	24.43 %	10.183 kg	20.72 %	9.833 kg	16.57 %
Force B (3.609 kg)	2.952 kg	18.20 %	3.450 kg	4.41 %	3.684 kg	2.08 %
RMS Error	-	19.49 %	-	19.13 %	-	15.26 %

It is seen that an error value of 158.9 % was calculated for Gauge B and Element 7029, but no elements in the vicinity showed any better correlation. The strain values of the surrounding elements in the FE model are in Table D.21. Note that Element 7029 was still included in the matrix, even though an 158.9 % was calculated for the numerical and measured responses.

Table 8.10: Measured strain values for Load Case 3

	Average Strain [mm/mm]	Calculated FE Strains [mm/mm]	% Difference
Gauge B & Element 7 029	$1.07 \times 10^{-05}$	$2.77 \times 10^{-05}$	<b>158.9 %</b>
Gauge C & Element 10 147	$6.14 \times 10^{-05}$	$3.90 \times 10^{-05}$	<b>36.5 %</b>
Gauge D & Element 12 687	$-1.03 \times 10^{-04}$	$-1.00 \times 10^{-04}$	2.9 %
Gauge E & Element 13 559	$-1.04 \times 10^{-04}$	$-7.83 \times 10^{-05}$	<b>24.7 %</b>

## 8.6 Summary

An experiment was designed to test the ability of the load reconstruction technique to determine the applied loads on a simplified structure. First of all, the original candidate set was reduced through filtering, after which the resultant candidate set was optimised. From this last optimisation the optimal gauge locations and orientations were determined. Known weights were suspended from an aluminium frame and the strain results were captured at the optimal candidate points (design points). The measured strain values were used to reconstruct the loads with various versions of the proportionality matrix. Since the magnitude of the loads were known, the measured and calculated strain values could be compared.

# Chapter 9

## Conclusion

### 9.1 Project Summary

A methodology for estimating the applied forces, without explicitly measuring these loads, were developed. It was assumed that the structural response remains linear in order for the principle of superposition to hold. Then, the measured strain response of a prototype structure can be used, in conjunction with an FE model, to determine the magnitude of the applied loads with a least-squares estimate. First of all, the linear relationship between the input loading and output strain response had to be determined. This strain-load relationship model, also known as the candidate set, is constructed from the linear static strain solutions of unit-load FE models. Each column in the candidate set equals the strain field over the discretised model, due to an individual applied unit-load. The rows correspond to the strain response of a ‘virtual’ strain gauge at various locations and orientations. Next, the strain gauge mounting locations and orientations had to be established. Optimal sensor placements were determined with a D-optimal design; this design selects candidate points that will maximise the determinant of the information matrix. These optimal candidate points dictates sensor placements and comprises the proportionality (or design) matrix.

A variety of filters were designed to exclude specific finite-elements from the candidate set to prevent any practical difficulties in mounting strain gauges. The three structural filters remove triangular finite-elements as well as elements at open and sharp edges. It was found during trial tests that incorrect values will be measured if the strain output is below the minimum measuring capability of the gauge; a fourth filter was designed to identify all elements for which strain values below this minimum measuring ability were computed. Experience has taught that a strain gauge should be mounted in areas of high strain, but of low strain gradient. The fifth and final filter is an outlier based algorithm, designed to remove elements that are associated with areas of high strain gradient. An adjusted boxplot approach identifies which computed strain gradients are unacceptable.



It was numerically investigated how the number of candidate points in the proportionality matrix affects the accuracy of the reconstructed loads; the conclusion was that more points will ensure that loads are accurately reconstructed. The full optimisation method is the preferred method of optimisation, since only a single set of gauges need to be mounted to reconstruct multiple load cases. Finally, all considerations were incorporated into a single physical experiment, where the ability of the technique to reconstruct multiple loads was investigated. It was found that if a gauge is mounted over more than one finite-element, the loads were more precisely reconstructed with a weighted average proportionality matrix than a matrix that consists of the original optimal candidate points. As was expected, the ultimate indicator for accurate load reconstruction is the correlation between the FE and real-life model; the better the correlation, the more accurately the loads will be reconstructed. It was also illustrated how strain gradients result in incorrect strain measurements. The methodology that should be followed to reconstruct loads in future studies, is outlined in Figure 9.1.

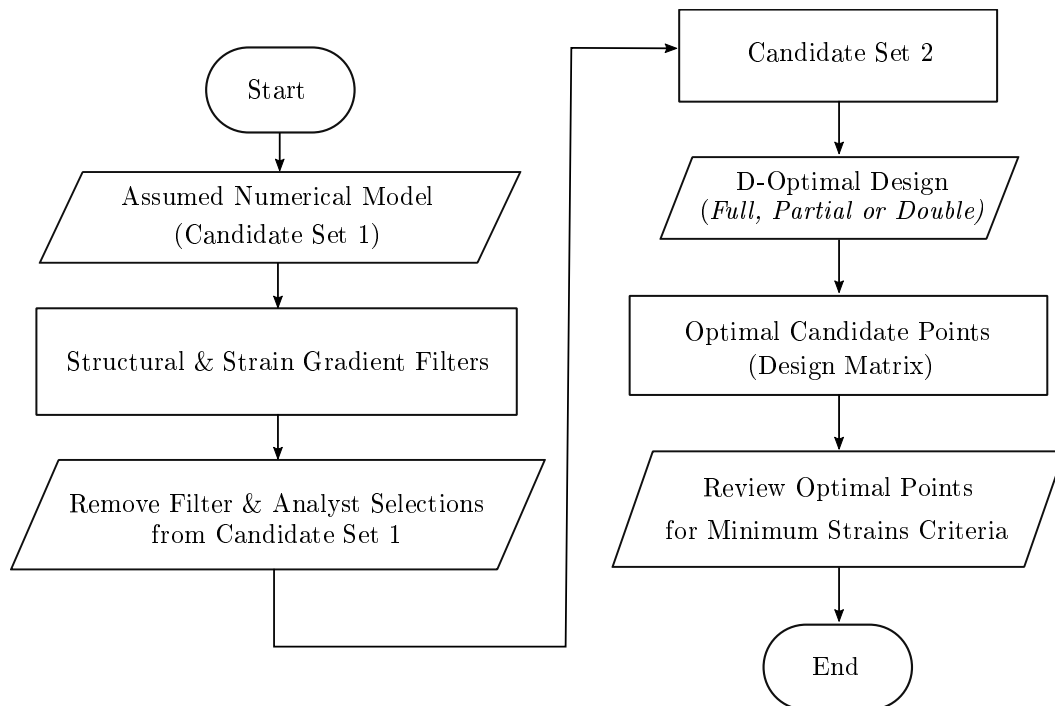


Figure 9.1: Final methodology for static load reconstruction

## 9.2 Future Recommendations

It was found in Chapter 8 that the greatest source of error between the calculated and actual loads originates from the differences between the FE and actual model. In future studies, a calibration step can be added to the methodology, where known

loads are applied to the structure in order to validate the accuracy of the FE model. Another interesting activity would be to compare the optimal candidate points selected in the D-optimal design to locations and orientations chosen by various engineers and technicians who mount strain gauges based on experience.

The designed filters were exceptionally effective, especially for complicated structures, like in Chapter 6. There is the option to develop more structural filters that will automate the removal of elements with limited manual input from the analyst. One could design a filter that removes elements in areas where loads and constraints are applied, since these regions are often inaccessible. Then, there is also the opportunity to design a filter that evaluates the quality of an element and excludes those that are considered to be ‘too warped’. It was found that measuring the elemental coordinate systems (ECSYS) of warped or distorted elements can be difficult. Lastly, a filter that removes welds and the surrounding areas with high residual strains and stresses, can be designed.

Furthermore, the Strain Gradient filter is a first of its kind and there is definitely an opportunity to improve its performance. For example, it was found in Chapter 8 that the filter did not manage to detect the strain gradient around Gauge A for Load Cases 1 and 2. The current method uses the Von Mises strain to avoid the directional characteristic of strain values. Alternatively, one could consider using supervised machine learning methods, such as classification, to identify areas of high strain and do a local strain gradient analysis. As another option, the use of alternative skewness measurement, as opposed to the medcouple, can be investigated. Perhaps this could improve the outliers detected by the adjusted boxplot method. The transformation approach proposed in Appendix B.1 were rejected due to its inability to introduce symmetry into the data set. However, it was recollected that these methods actually managed to identify more outliers than the adjusted boxplot method in Section 5.1.5. These ideas could perhaps be revisited and tested experimentally.

In Chapter 7 it was established that more candidate points in the proportionality matrix improves the accuracy of the reconstructed loads. However, in Figure 8.6 it was seen that the D-optimal design could not select more than five unique candidate points from a filtered candidate set. For future studies, the following approach is advised if the analyst wishes to increase the number of candidate points in the design matrix even though the D-optimal design cannot find more distinct design points. Firstly, the maximum number of design points of the filtered candidate set should be determined similarly to how the design points in Figure 8.7 were determined. Next, these selected candidate points should be removed from the candidate set with a layer of finite-elements surrounding these candidate points. If bordering layers are not removed, the D-optimal design will simply choose finite-elements next to the original optimal candidate points; this occurrence is noticed in Figure 8.3. After the original optimal candidate points, with a bordering layer of finite-elements, are removed from the filtered candidate set, this further reduced candidate set can be optimised for a second round.

# Appendices

# Appendix A

## Gauge Placement Function

Each candidate point in the candidate set corresponds to a specific combination of gauge location and orientation. This angle of orientation is defined with respect to the elemental coordinate system (ECSYS) of the corresponding two-dimensional (2D) element (Figure A.1). For a given list of 2D elements and corresponding orientation angles, this function yields the coordinate points and orientation angles of the gauges in any desired global coordinate system (GCSYS).

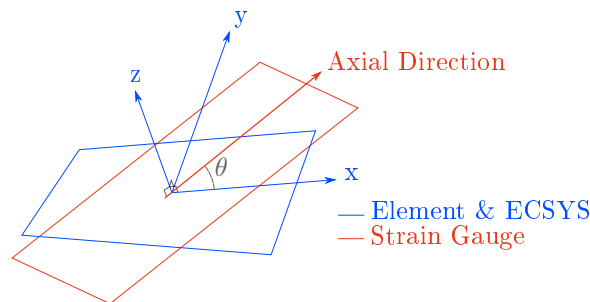


Figure A.1: Orientation of strain gauge with respect to a quadrilateral element and its elemental coordinate system (ECSYS).

### A.1 Coordinate Systems in Nastran

A short description of coordinate systems in Nastran is first required. Two types of *global* coordinate systems exist: the *basic* coordinate system is the implicitly defined absolute coordinate system and *local* coordinate systems can be explicitly defined in addition to the basic coordinate system. Local coordinate systems can be created using two different approaches: Type CORD1x defines a local coordinate system using the ID's of three grid points and Type CORD2x uses the coordinate of three points in a previously defined coordinate system (Siemens, 2014b, pg. 6-2).

The ‘x’ in the acronym can either be replaced by an ‘R’, ‘S’ or ‘C’ that respectively refers to a rectangular, spherical or cylindrical coordinate system. Only the CORD2R data card will be considered, since modern pre-/post-processor no longer makes use of Type CORD1x data cards and rectangular coordinate systems are sufficient. Another type of coordinate system is the elemental coordinate system (ECSYS). This coordinate system is inherent to the finite-element and schematics can be found in Figure 4.1.

The user is allowed to choose between releasing the location of the strain gauge in a predefined global rectangular coordinate system, either with respect to the origin of that coordinate system, or with respect to a reference node (Figure A.2). It was found during experimentation that creating an additional local coordinate system is sometimes unnecessary; one could just as well define the position of the strain gauge based on another known grid point (or node).

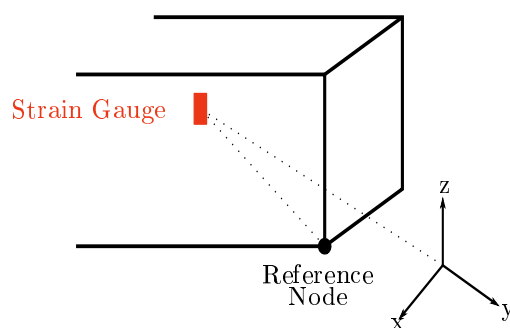


Figure A.2: Strain gauge position relative to the origin of a global coordinate system (GCSYS) or a reference node.

## A.2 Mathematical Background

The axial direction of the strain gauge can be visualised as a vector in the  $xy$ -plane of the ECSYS as shown in Figure A.1. This vector, denoted as  $\mathbf{A}$ , can be transformed to global coordinates, using vector transformations. The magnitude of  $\mathbf{A}$  remains the same, irrespective of the coordinate system (Widnall, 2009):

$$\mathbf{A} = A_1 \mathbf{i}_1 + A_2 \mathbf{i}_2 + A_3 \mathbf{i}_3 = A'_1 \mathbf{i}'_1 + A'_2 \mathbf{i}'_2 + A'_3 \mathbf{i}'_3 \quad (\text{A.1})$$

thus, the components of  $\mathbf{A}$  in the global coordinate system (GCSYS) can be determined in terms of the components in ECSYS, by taking the dot product of the unit vectors,

$$A'_j = A_1 \mathbf{i}'_j \cdot \mathbf{i}_1 + A_2 \mathbf{i}'_j \cdot \mathbf{i}_2 + A_3 \mathbf{i}'_j \cdot \mathbf{i}_3$$

and as a result,

$$\begin{pmatrix} A'_1 \\ A'_2 \\ A'_3 \end{pmatrix} = \begin{pmatrix} \mathbf{i}'_1 \cdot \mathbf{i}_1 & \mathbf{i}'_1 \cdot \mathbf{i}_2 & \mathbf{i}'_1 \cdot \mathbf{i}_3 \\ \mathbf{i}'_2 \cdot \mathbf{i}_1 & \mathbf{i}'_2 \cdot \mathbf{i}_2 & \mathbf{i}'_2 \cdot \mathbf{i}_3 \\ \mathbf{i}'_3 \cdot \mathbf{i}_1 & \mathbf{i}'_3 \cdot \mathbf{i}_2 & \mathbf{i}'_3 \cdot \mathbf{i}_3 \end{pmatrix} \begin{pmatrix} A_1 \\ A_2 \\ A_3 \end{pmatrix} \quad (\text{A.2})$$

The dot product of two unit vectors equal the cosine of the angle between these vectors. From this, the transformation matrix is given as:

$$\mathbf{Q} = \begin{pmatrix} \mathbf{i}'_1 \cdot \mathbf{i}_1 & \mathbf{i}'_1 \cdot \mathbf{i}_2 & \mathbf{i}'_1 \cdot \mathbf{i}_3 \\ \mathbf{i}'_2 \cdot \mathbf{i}_1 & \mathbf{i}'_2 \cdot \mathbf{i}_2 & \mathbf{i}'_2 \cdot \mathbf{i}_3 \\ \mathbf{i}'_3 \cdot \mathbf{i}_1 & \mathbf{i}'_3 \cdot \mathbf{i}_2 & \mathbf{i}'_3 \cdot \mathbf{i}_3 \end{pmatrix} = \begin{pmatrix} \cos(\theta_{11}) & \cos(\theta_{12}) & \cos(\theta_{13}) \\ \cos(\theta_{21}) & \cos(\theta_{22}) & \cos(\theta_{23}) \\ \cos(\theta_{31}) & \cos(\theta_{32}) & \cos(\theta_{33}) \end{pmatrix} \quad (\text{A.3})$$

The orientation of the strain gauge relative to the GCSYS is depicted in Figure A.3 and can be calculated using Equations A.2 and A.4:

$$\begin{aligned} \alpha &= \cos^{-1}(A'_1) \\ \beta &= \cos^{-1}(A'_2) \\ \gamma &= \cos^{-1}(A'_3) \end{aligned} \quad (\text{A.4})$$

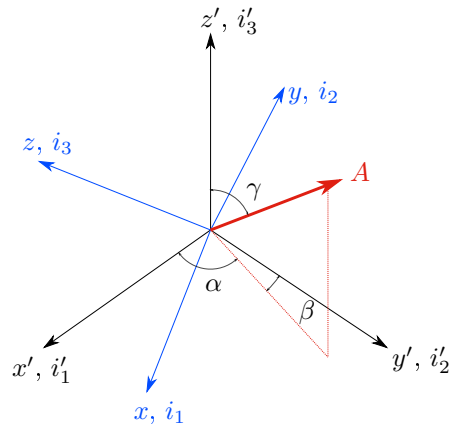


Figure A.3: Rotation angles of vector  $A$  relative to a global coordinate system (GCSYS).

### A.2.1 Performance of Strain Gauge Placement Function

The function was assessed on its ability to find the correct location and orientation of a strain gauge in a desired global coordinate system. Calculating its orientation is more complicated than finding the location of the strain gauge and will be elaborated on in the following content. A sample FE model (Figure A.4) was created of which the material parameters, mesh size, boundary and loading conditions are not of importance. Three local coordinate systems were additionally defined. It is important to note that these local coordinate systems will not be written to the Nastran's input file if it is not referenced, for example by a boundary condition, in the model itself.

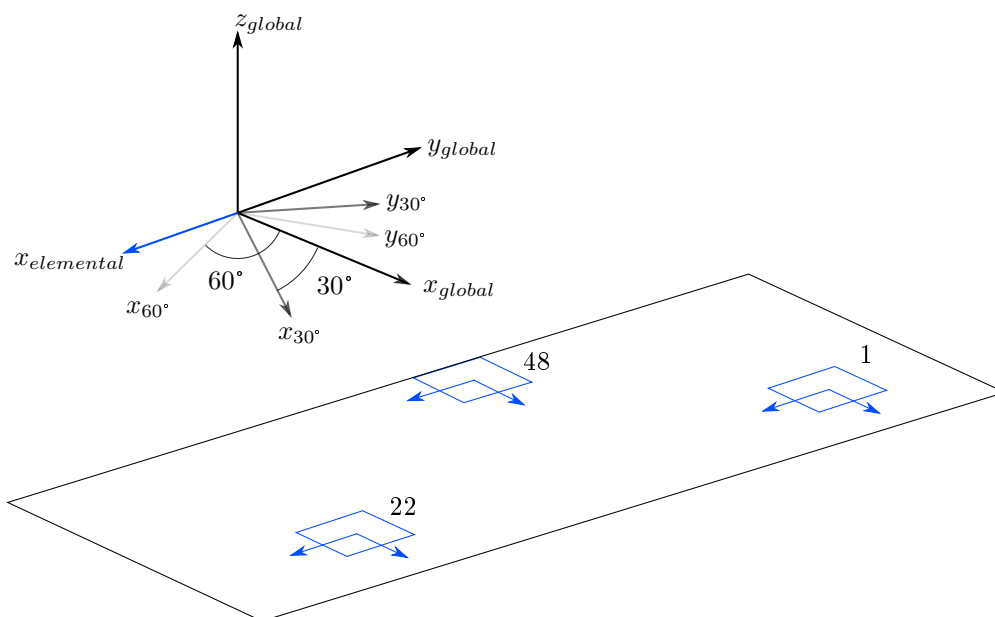


Figure A.4: Sample FE model to test mounting function.

CQUAD4 elements were chosen using a random integer generator and the ECSYS of these elements are shown in Figure A.4. It was assumed that the strain gauges need to be mounted at  $0^\circ$  and  $45^\circ$  with respect to the ECSYS of each element. The results for Element 1 is shown in Table A.1 and proves that the function accurately obtains the correct angles of orientation in any locally defined global coordinate system.

Table A.1: Results of mounting function.

$\theta$	GCSYS	Theoretical Calculations			Mounting Function Output		
		$\alpha$	$\beta$	$\gamma$	$\alpha$	$\beta$	$\gamma$
0°	30°	60	150	90	59.999	149.997	90.000
	60°	30	120	90	30.003	120.000	90.000
45°	30°	15	105	90	15.006	104.999	90.000
	60°	15	75	90	15.006	75.001	90.000



## Appendix B

# Symmetric Outlier Detection Methods

An attempt was made to introduce symmetry in the strain gradient data set to eventually use outlier detection methods commonly associated with normally distributed data, such as the use of standard deviations or the interquartile range (IQR). Symmetry is commonly achieved by means of transformation, such as taking the logarithm of each data point. The FE model in Figure B.1 was used to test the transformation technique.

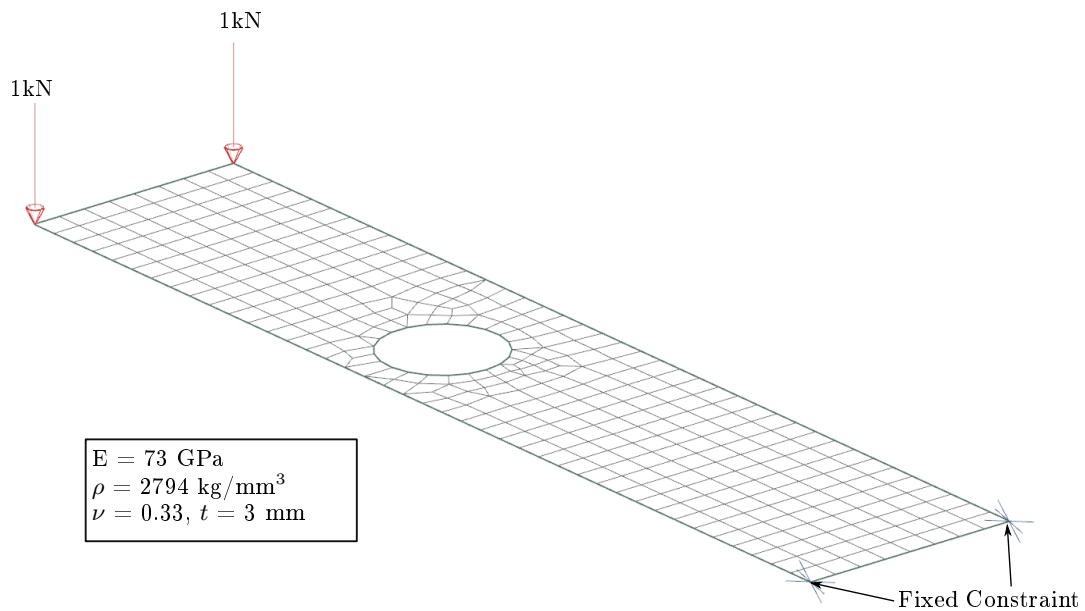


Figure B.1: Sample FE model used to test other outlier detection techniques.

The logarithm of each data point (strain gradient) of Figure B.1 is graphed in Figure B.4, where it is seen that the distribution is more symmetrical than the data in Figure 5.7. A standard boxplot, i.e. whose whiskers are defined by Equation 5.5, was used to identify outliers. A total of 194 outliers were detected and highlighted in Figure B.2. These elements are scattered all over the FE model and does not conform to what is desired. By transforming the data points, the outliers are brought closer to the original data set before attempting to detect them; thus, the outlier detection algorithm is more likely to eliminate good data points.

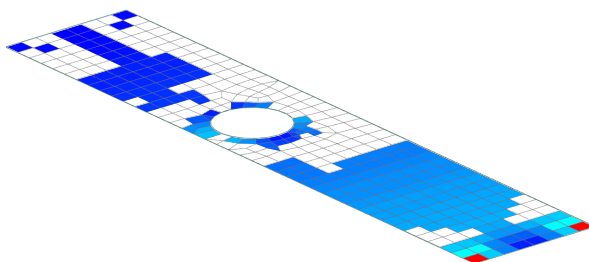


Figure B.2: Outliers detected based on *logarithmic transformation* and *standard boxplot* procedures.

It was decided to combine the adjusted outlier detection method with logarithmic transformation, since the data in Figure B.4 is not perfectly symmetric based on the analyst's subjective opinion. The boxplot and corresponding histogram is shown in Figure B.5. A total of 148 outliers were identified and highlighted in Figure B.3. This method conforms better to what is desired as opposed to the previous model, but is more conservative than the method in Section 5.1.5.

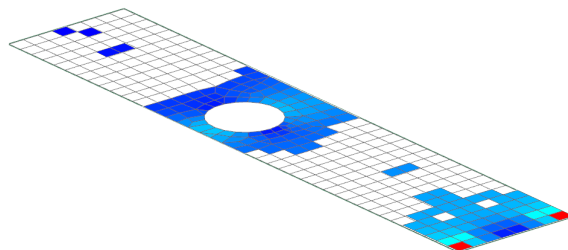


Figure B.3: Outliers detected based on *logarithmic transformation* and *adjusted boxplot* procedures.

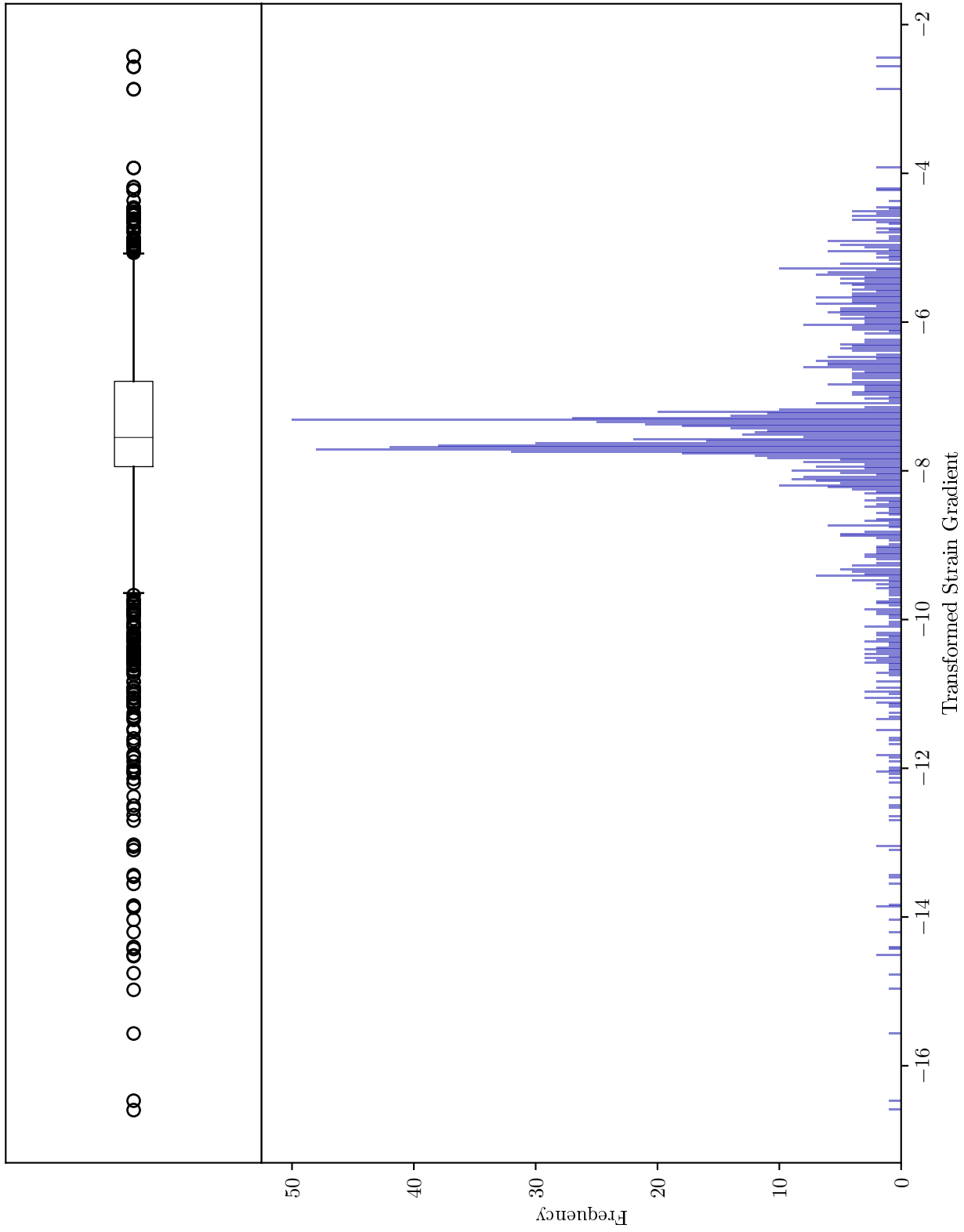


Figure B.4: Logarithmic transformed histogram of calculated strain gradients with standard boxplot parameters. Bins = 500; Whiskers = Equation 5.5; Data =  $\log_e(SG)$

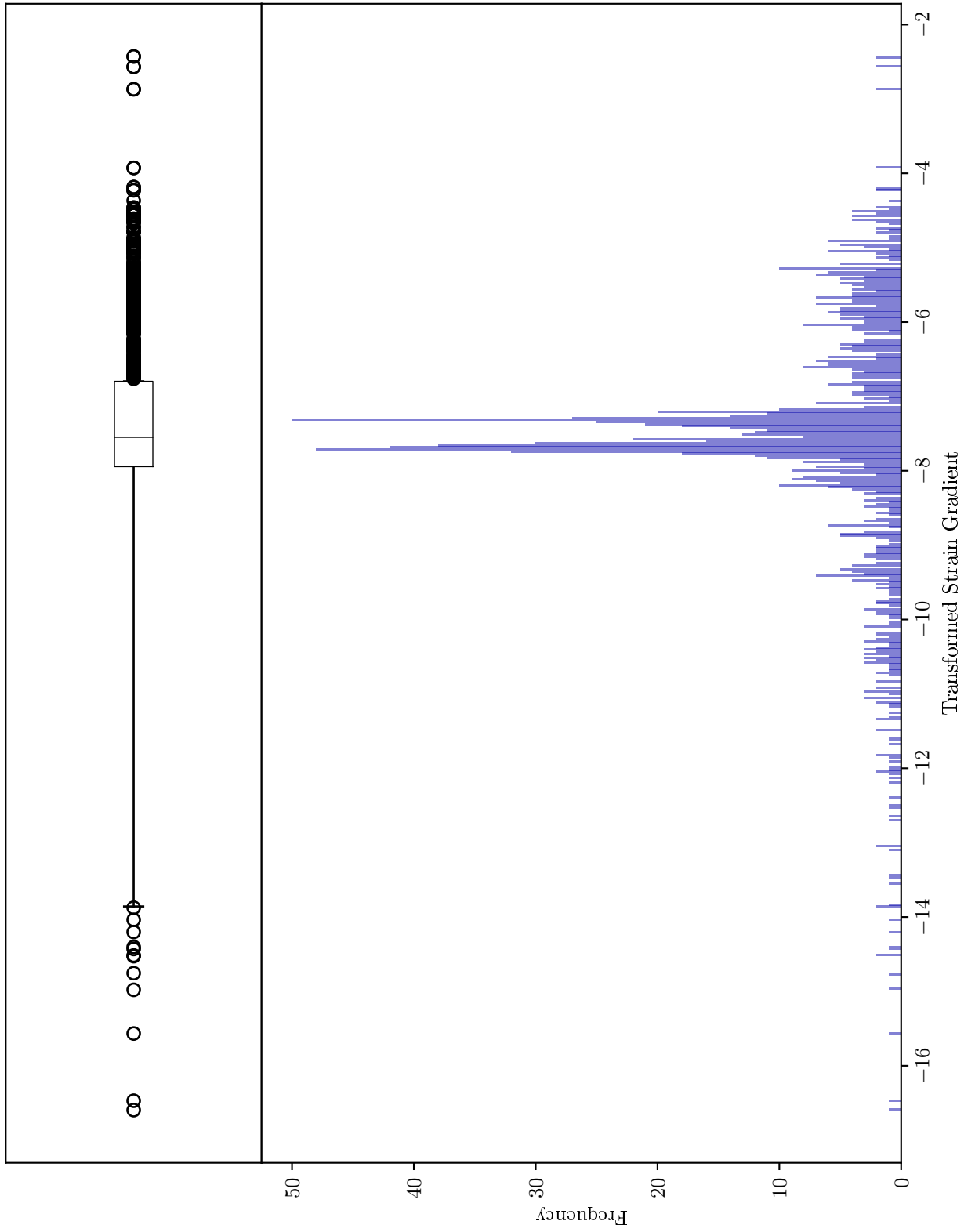
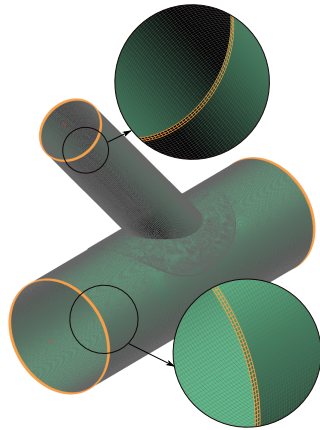


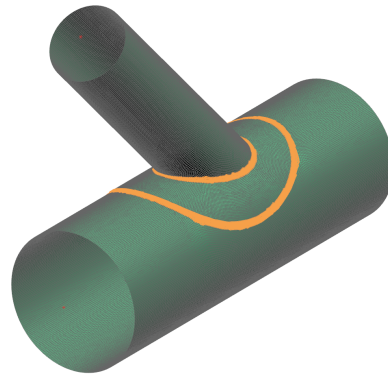
Figure B.5: Logarithmic transformed histogram of calculated strain gradients combined with the adjusted boxplot parameters. Bins = 500; Whiskers = Equation 5.6 & 5.7; Data =  $\log_e(SG)$

# Appendix C

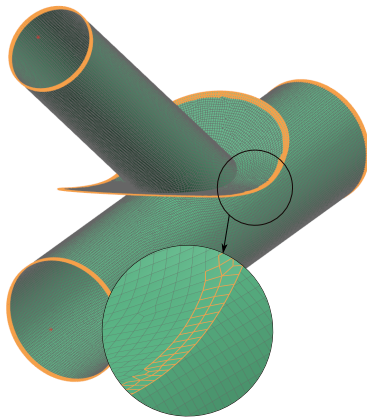
## Filtering Function Application



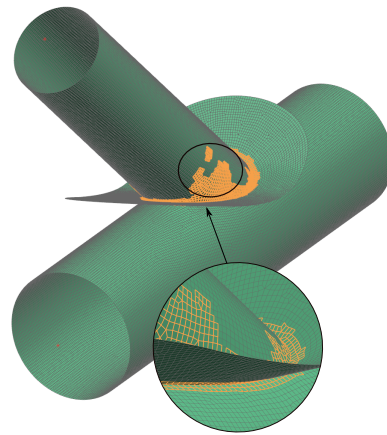
(a) Open Edges: Collar



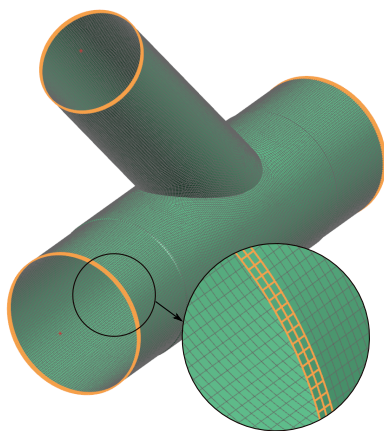
(b) Sharp Edges: Collar



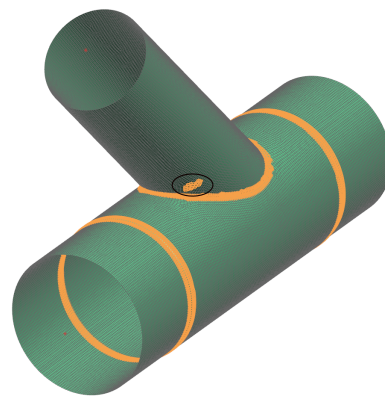
(c) Open Edges: Crotch



(d) Sharp Edges: Crotch

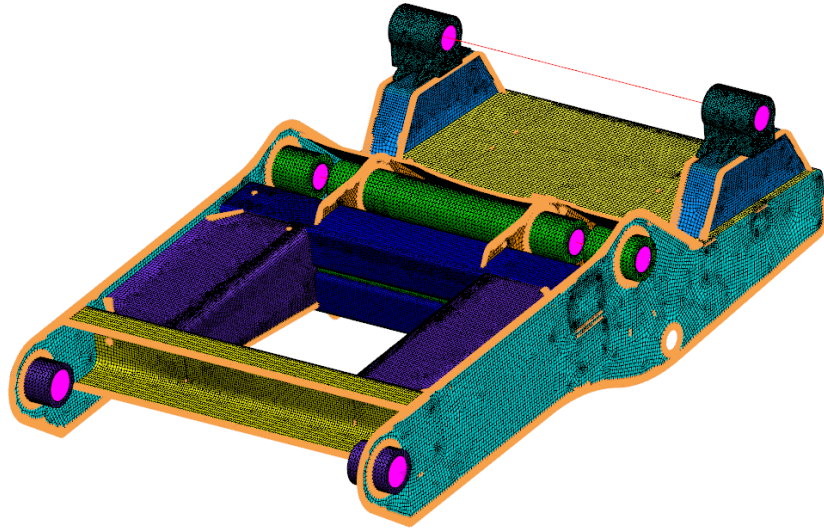


(e) Open Edges: Wrapper

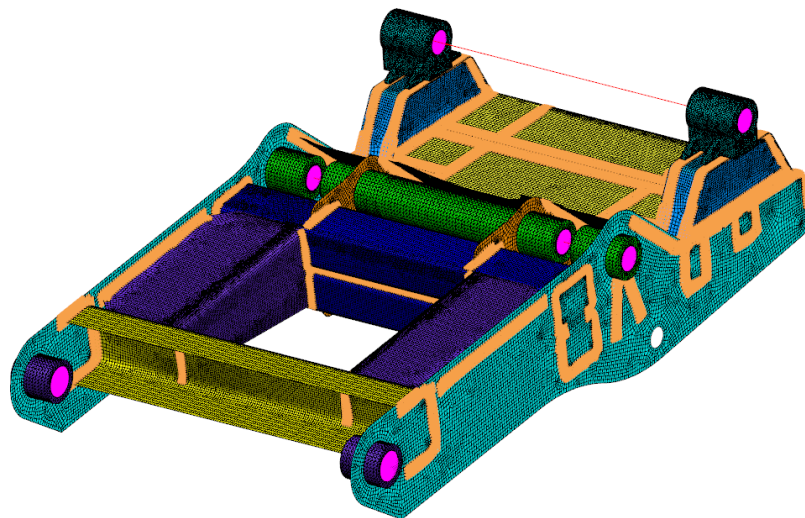


(f) Sharp Edges: Wrapper

Figure C.1: Structural filters on reinforced pipes with double layer removal.

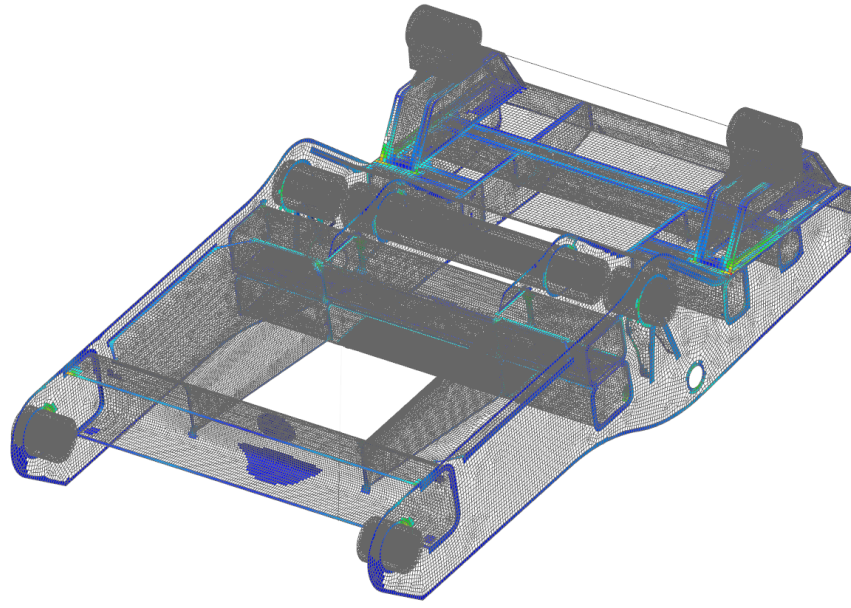


(a) Open Edges Filter

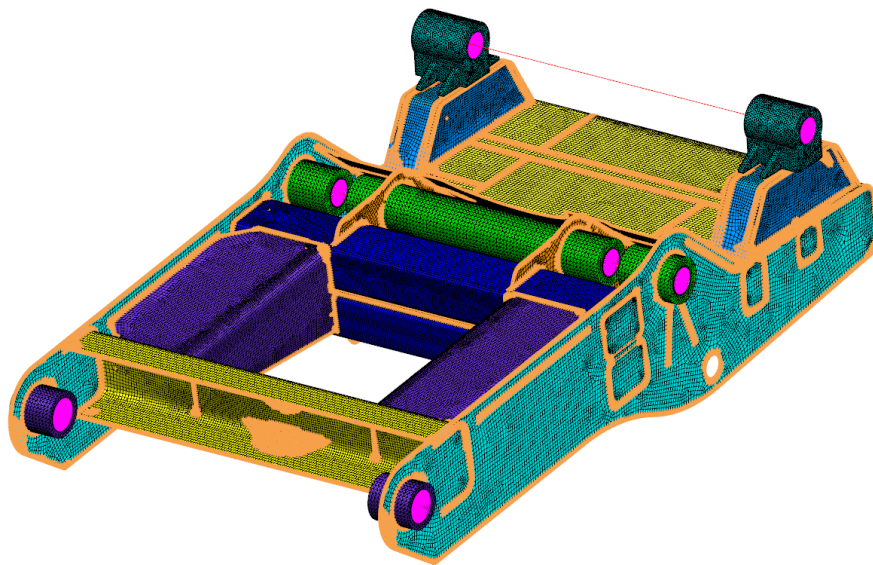


(b) Sharp Edges Filter

Figure C.2: Structural filters on hauler truck model with double layer removal.



(a) Wireframe View



(b) Elemental View

Figure C.3: All filters on hauler truck model.



# Appendix D

## Additional Experimental Material

### D.1 Candidate Points of Unfiltered Candidate Set

Table D.1: Optimal design points of Candidate Set 1 using the full optimisation method.

Consolidated Results		Design Points = 4		Design Points = 5		Design Points = 6		Design Points = 7	
Rotation	Element	Rotation	Element	Rotation	Element	Rotation	Element	Rotation	Element
90°	4764	90°	4764	90°	4764	90°	4764	90°	4764
45°	4983	45°	4983	-	-	-	4983	45°	4983
0°	6379	-	-	-	-	-	-	-	-
0°	6388	0°	6388	-	-	-	-	-	-
0°	6389	-	-	0°	6389	-	-	-	-
90°	8534	-	-	90°	8536	-	-	90°	8534
90°	8536	-	-	-	-	-	-	-	-
0°	8542	-	-	-	-	0°	8542	-	-
45°	10911	-	-	-	-	45°	10911	45°	10911
135°	11829	-	-	135°	11829	-	-	-	-
45°	13616	-	-	-	-	45°	13616	45°	13616
90°	15926	-	-	-	-	90°	15926	90°	15926
90°	15929	90°	15929	-	-	-	-	-	-
0°	15936	-	-	0°	15936	0°	15936	0°	15936

Design Points = 8		Design Points = 9		Design Points = 10		Design Points = 11		Design Points = 12	
Rotation	Element	Rotation	Element	Rotation	Element	Rotation	Element	Rotation	Element
90°	4764	90°	4764	90°	4764	90°	4764	90°	4764
45°	4983	45°	4983	45°	4983	45°	4983	45°	4983
-	-	0°	6379	-	-	-	-	0°	6379
-	-	-	-	-	-	-	-	-	-
0°	6389	-	-	-	-	-	-	-	-
90°	8534	90°	8534	90°	8534	90°	8534	90°	8534
-	-	-	-	-	-	-	-	-	-
-	-	-	-	45°	10911	-	-	45°	10911
135°	11829	135°	11829	-	-	-	-	135°	11829
-	-	-	-	45°	13616	-	-	-	-
-	-	90°	15926	90°	15926	-	-	-	-
-	-	-	-	-	-	-	-	90°	15926
0°	15936	0°	15936	0°	15936	0°	15936	0°	15936

## D.2 Measured Strain Responses

Table D.2: Measured strain values at optimal design points for Load Case 1

	Gauge A	Gauge B	Gauge C	Gauge D	Gauge E
Measurement 1	$-6.54 \times 10^{-05}$	$-3.30 \times 10^{-05}$	$-4.98 \times 10^{-04}$	$-4.15 \times 10^{-04}$	$-3.69 \times 10^{-04}$
Measurement 2	$-6.53 \times 10^{-05}$	$-3.31 \times 10^{-05}$	$-4.97 \times 10^{-04}$	$-4.18 \times 10^{-04}$	$-3.68 \times 10^{-04}$
Measurement 3	$-6.18 \times 10^{-05}$	$-3.24 \times 10^{-05}$	$-4.99 \times 10^{-04}$	$-4.17 \times 10^{-04}$	$-3.69 \times 10^{-04}$
Measurement 4	$-6.99 \times 10^{-05}$	$-3.27 \times 10^{-05}$	$-4.97 \times 10^{-04}$	$-4.16 \times 10^{-04}$	$-3.70 \times 10^{-04}$
Measurement 5	$-6.39 \times 10^{-05}$	$-3.27 \times 10^{-05}$	$-4.97 \times 10^{-04}$	$-4.15 \times 10^{-04}$	$-3.71 \times 10^{-04}$
Average	$-6.53 \times 10^{-05}$	$-3.28 \times 10^{-05}$	$-4.98 \times 10^{-04}$	$-4.16 \times 10^{-04}$	$-3.69 \times 10^{-04}$
Standard Deviation	$2.66 \times 10^{-06}$	$2.38 \times 10^{-07}$	$5.96 \times 10^{-07}$	$9.02 \times 10^{-07}$	$1.02 \times 10^{-06}$
COV [%]	-4.08 %	-0.73 %	-0.12 %	-0.22 %	-0.28 %

Table D.3: Measured strain values at optimal design points for Load Case 2

	Gauge A	Gauge B	Gauge C	Gauge D	Gauge E
Measurement 1	$-7.18 \times 10^{-06}$	$5.38 \times 10^{-05}$	$-2.89 \times 10^{-04}$	$-2.67 \times 10^{-04}$	$-2.41 \times 10^{-04}$
Measurement 2	$-6.83 \times 10^{-06}$	$4.95 \times 10^{-05}$	$-2.88 \times 10^{-04}$	$-2.64 \times 10^{-04}$	$-2.43 \times 10^{-04}$
Measurement 3	$-7.46 \times 10^{-06}$	$5.44 \times 10^{-05}$	$-2.88 \times 10^{-04}$	$-2.68 \times 10^{-04}$	$-2.40 \times 10^{-04}$
Measurement 4	$-7.40 \times 10^{-06}$	$4.87 \times 10^{-05}$	$-2.89 \times 10^{-04}$	$-2.67 \times 10^{-04}$	$-2.40 \times 10^{-04}$
Measurement 5	$-7.28 \times 10^{-06}$	$5.39 \times 10^{-05}$	$-2.88 \times 10^{-04}$	$-2.66 \times 10^{-04}$	$-2.39 \times 10^{-04}$
Average	$-7.23 \times 10^{-06}$	$5.20 \times 10^{-05}$	$-2.88 \times 10^{-04}$	$-2.66 \times 10^{-04}$	$-2.41 \times 10^{-04}$
Standard Deviation	$2.23 \times 10^{-07}$	$2.44 \times 10^{-06}$	$2.60 \times 10^{-07}$	$1.18 \times 10^{-06}$	$1.52 \times 10^{-06}$
COV [%]	-3.08 %	4.69 %	-0.09 %	-0.44 %	-0.63 %

Table D.4: Measured strain values at optimal design points for Load Case 3

	Gauge A	Gauge B	Gauge C	Gauge D	Gauge E
Measurement 1	$2.91 \times 10^{-07}$	$1.01 \times 10^{-05}$	$6.15 \times 10^{-05}$	$-1.06 \times 10^{-04}$	$-1.05 \times 10^{-04}$
Measurement 2	$3.57 \times 10^{-07}$	$1.06 \times 10^{-05}$	$6.21 \times 10^{-05}$	$-1.01 \times 10^{-04}$	$-1.06 \times 10^{-04}$
Measurement 3	$-5.87 \times 10^{-08}$	$1.09 \times 10^{-05}$	$6.48 \times 10^{-05}$	$-1.04 \times 10^{-04}$	$-1.04 \times 10^{-04}$
Measurement 4	$2.51 \times 10^{-08}$	$1.09 \times 10^{-05}$	$5.86 \times 10^{-05}$	$-1.01 \times 10^{-04}$	$-1.05 \times 10^{-04}$
Measurement 5	$-1.32 \times 10^{-07}$	$1.09 \times 10^{-05}$	$5.99 \times 10^{-05}$	$-9.98 \times 10^{-05}$	$-1.02 \times 10^{-04}$
Average	$9.66 \times 10^{-08}$	$1.07 \times 10^{-05}$	$6.14 \times 10^{-05}$	$-1.03 \times 10^{-04}$	$-1.04 \times 10^{-04}$
Standard Deviation	$1.93 \times 10^{-07}$	$3.04 \times 10^{-07}$	$2.12 \times 10^{-06}$	$2.40 \times 10^{-06}$	$1.18 \times 10^{-06}$
COV [%]	200.30 %	2.84 %	3.46 %	-2.34 %	-1.13 %

### D.3 Percentage Gauge Cover

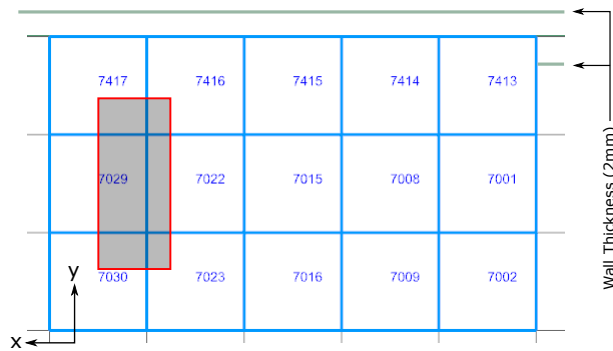


Figure D.1: Location of Gauge B

Table D.5: Surface coverage of Gauge B

Element	% Coverage
7022	18.7 %
7023	6.8 %
7029	38.6 %
7030	14.2 %
7416	7.1 %
7417	14.7 %

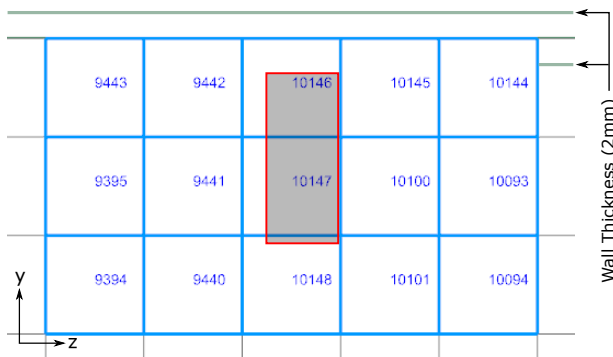


Figure D.2: Location of Gauge C

Table D.6: Surface coverage of Gauge C

Element	% Coverage
10146	37.5 %
10147	57.5 %
10148	4.9 %

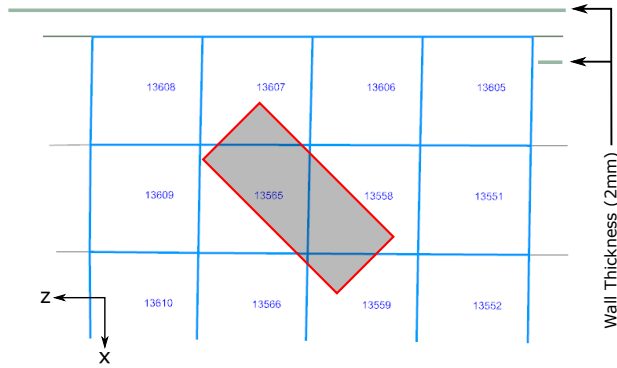


Table D.7: Surface coverage of Gauge E

Element	% Coverage
13558	12.6 %
13559	45.4 %
13565	0.4 %
13566	31.8 %
13607	9.8 %

Figure D.3: Location of Gauge E

## D.4 Averaged Design Matrix

Table D.8: Averaged candidate point corresponding to Gauge A

Design Point	Column A	Column B	Column C	Column D
1729, 0°	$-2.44 \times 10^{-13}$	$-1.23 \times 10^{-10}$	$-4.49 \times 10^{-06}$	$-5.25 \times 10^{-05}$
1730, 0°	$-4.36 \times 10^{-13}$	$-3.79 \times 10^{-11}$	$-2.71 \times 10^{-06}$	$-3.86 \times 10^{-05}$
2374, 0°	$-7.22 \times 10^{-13}$	$1.21 \times 10^{-11}$	$-1.28 \times 10^{-06}$	$-3.82 \times 10^{-05}$
2375, 0°	$-7.32 \times 10^{-13}$	$-4.76 \times 10^{-11}$	$-2.97 \times 10^{-06}$	$-5.52 \times 10^{-05}$
Averaged Design Point	$-5.34 \times 10^{-13}$	$-4.91 \times 10^{-11}$	$-2.86 \times 10^{-06}$	$-4.61 \times 10^{-05}$

Table D.9: Averaged candidate point corresponding to Gauge B

Design Point	Column A	Column B	Column C	Column D
7022, 90°	$-9.80 \times 10^{-12}$	$8.29 \times 10^{-06}$	$-2.51 \times 10^{-06}$	$-2.31 \times 10^{-06}$
7023, 90°	$-6.30 \times 10^{-12}$	$5.65 \times 10^{-06}$	$-1.67 \times 10^{-06}$	$-1.56 \times 10^{-06}$
7029, 90°	$-1.07 \times 10^{-11}$	$7.67 \times 10^{-06}$	$-2.44 \times 10^{-06}$	$-2.48 \times 10^{-06}$
7030, 90°	$-6.89 \times 10^{-12}$	$5.41 \times 10^{-06}$	$-1.62 \times 10^{-06}$	$-1.69 \times 10^{-06}$
7416, 90°	$-1.36 \times 10^{-11}$	$1.22 \times 10^{-05}$	$-3.34 \times 10^{-06}$	$-2.92 \times 10^{-06}$
7417, 90°	$-1.50 \times 10^{-11}$	$1.07 \times 10^{-05}$	$-3.30 \times 10^{-06}$	$-3.13 \times 10^{-06}$
Averaged Design Point	$-1.04 \times 10^{-11}$	$8.31 \times 10^{-06}$	$-2.48 \times 10^{-06}$	$-2.35 \times 10^{-06}$

Table D.10: Averaged candidate point corresponding to Gauge C

Design Point	Column A	Column B	Column C	Column D
10146, 90°	$1.52 \times 10^{-05}$	$-1.68 \times 10^{-05}$	$-4.32 \times 10^{-05}$	$-3.79 \times 10^{-05}$
10147, 90°	$1.01 \times 10^{-05}$	$-1.29 \times 10^{-05}$	$-3.33 \times 10^{-05}$	$-2.92 \times 10^{-05}$
10148, 90°	$6.71 \times 10^{-06}$	$-8.73 \times 10^{-06}$	$-2.25 \times 10^{-05}$	$-1.97 \times 10^{-05}$
Averaged Design Point	$1.07 \times 10^{-05}$	$-1.28 \times 10^{-05}$	$-3.30 \times 10^{-05}$	$-2.89 \times 10^{-05}$

Table D.11: Averaged candidate point corresponding to Gauge D

Design Point	Column A	Column B	Column C	Column D
12679, 45°	$-4.09 \times 10^{-06}$	$-1.21 \times 10^{-05}$	$-2.79 \times 10^{-05}$	$-2.24 \times 10^{-05}$
12680, 45°	$-4.13 \times 10^{-06}$	$-1.52 \times 10^{-05}$	$-3.58 \times 10^{-05}$	$-2.60 \times 10^{-05}$
12686, 45°	$-5.95 \times 10^{-06}$	$-1.23 \times 10^{-05}$	$-2.86 \times 10^{-05}$	$-2.22 \times 10^{-05}$
12687, 45°	$-5.45 \times 10^{-06}$	$-1.55 \times 10^{-05}$	$-3.67 \times 10^{-05}$	$-2.61 \times 10^{-05}$
12731, 45°	$-6.83 \times 10^{-06}$	$-1.56 \times 10^{-05}$	$-3.70 \times 10^{-05}$	$-2.57 \times 10^{-05}$
12732, 45°	$-3.80 \times 10^{-06}$	$-1.85 \times 10^{-05}$	$-4.42 \times 10^{-05}$	$-3.01 \times 10^{-05}$
12733, 45°	$-3.49 \times 10^{-06}$	$-1.84 \times 10^{-05}$	$-4.39 \times 10^{-05}$	$-2.99 \times 10^{-05}$
Averaged Design Point	$-4.82 \times 10^{-06}$	$-1.54 \times 10^{-05}$	$-3.63 \times 10^{-05}$	$-2.61 \times 10^{-05}$

Table D.12: Averaged candidate point corresponding to Gauge E

Design Point	Column A	Column B	Column C	Column D
13558, 135°	$-4.10 \times 10^{-06}$	$-1.52 \times 10^{-05}$	$-3.58 \times 10^{-05}$	$-3.73 \times 10^{-05}$
13559, 135°	$-4.08 \times 10^{-06}$	$-1.22 \times 10^{-05}$	$-2.82 \times 10^{-05}$	$-2.74 \times 10^{-05}$
13565, 135°	$-5.42 \times 10^{-06}$	$-1.55 \times 10^{-05}$	$-3.65 \times 10^{-05}$	$-3.84 \times 10^{-05}$
13566, 135°	$-5.79 \times 10^{-06}$	$-1.24 \times 10^{-05}$	$-2.87 \times 10^{-05}$	$-2.85 \times 10^{-05}$
13607, 135°	$-3.53 \times 10^{-06}$	$-1.83 \times 10^{-05}$	$-4.37 \times 10^{-05}$	$-4.73 \times 10^{-05}$
Averaged Design Point	$-4.58 \times 10^{-06}$	$-1.47 \times 10^{-05}$	$-3.46 \times 10^{-05}$	$-3.58 \times 10^{-05}$

## D.5 Weighted Averaged Design Matrix

Table D.13: Weighted averaged candidate point corresponding to Gauge A

Design Point	Weights	Column A	Column B	Column C	Column D
1729, 0°	30.15 %	$-7.36 \times 10^{-14}$	$-3.71 \times 10^{-11}$	$-1.36 \times 10^{-06}$	$-1.58 \times 10^{-05}$
1730, 0°	15.58 %	$-6.80 \times 10^{-14}$	$-5.91 \times 10^{-12}$	$-4.22 \times 10^{-07}$	$-6.01 \times 10^{-06}$
2374, 0°	18.38 %	$-2.59 \times 10^{-13}$	$4.34 \times 10^{-12}$	$-4.59 \times 10^{-07}$	$-1.37 \times 10^{-05}$
2375, 0°	35.89 %	$-1.35 \times 10^{-13}$	$-8.74 \times 10^{-12}$	$-5.47 \times 10^{-07}$	$-1.01 \times 10^{-05}$
Weighted Design Point	100.00 %	$-5.35 \times 10^{-13}$	$-4.74 \times 10^{-11}$	$-2.78 \times 10^{-06}$	$-4.57 \times 10^{-05}$

Table D.14: Weighted averaged candidate point corresponding to Gauge B

Design Point	Weights	Column A	Column B	Column C	Column D
7022, 90°	18.67 %	$-1.83 \times 10^{-12}$	$1.55 \times 10^{-06}$	$-4.68 \times 10^{-07}$	$-4.31 \times 10^{-07}$
7023, 90°	6.79 %	$-4.28 \times 10^{-13}$	$3.84 \times 10^{-07}$	$-1.13 \times 10^{-07}$	$-1.06 \times 10^{-07}$
7029, 90°	38.57 %	$-4.12 \times 10^{-12}$	$2.96 \times 10^{-06}$	$-9.42 \times 10^{-07}$	$-9.56 \times 10^{-07}$
7030, 90°	14.17 %	$-9.76 \times 10^{-13}$	$7.67 \times 10^{-07}$	$-2.29 \times 10^{-07}$	$-2.39 \times 10^{-07}$
7416, 90°	7.08 %	$-9.64 \times 10^{-13}$	$8.63 \times 10^{-07}$	$-2.36 \times 10^{-07}$	$-2.06 \times 10^{-07}$
7417, 90°	14.73 %	$-2.20 \times 10^{-12}$	$1.57 \times 10^{-06}$	$-4.86 \times 10^{-07}$	$-4.16 \times 10^{-07}$
Weighted Design Point	100.00 %	$-1.05 \times 10^{-11}$	$8.09 \times 10^{-06}$	$-2.47 \times 10^{-06}$	$-2.40 \times 10^{-06}$

Table D.15: Weighted averaged candidate point corresponding to Gauge C

Design Point	Weights	Column A	Column B	Column C	Column D
10146, 90°	37.54 %	$5.70 \times 10^{-06}$	$-6.29 \times 10^{-06}$	$-1.62 \times 10^{-05}$	$-1.42 \times 10^{-05}$
10147, 90°	57.53 %	$5.84 \times 10^{-06}$	$-7.43 \times 10^{-06}$	$-1.91 \times 10^{-05}$	$-1.68 \times 10^{-05}$
10148, 90°	4.93 %	$3.31 \times 10^{-07}$	$-4.31 \times 10^{-07}$	$-1.11 \times 10^{-06}$	$-9.72 \times 10^{-07}$
Weighted Design Point	100.00 %	$1.19 \times 10^{-05}$	$-1.42 \times 10^{-05}$	$-3.65 \times 10^{-05}$	$-3.20 \times 10^{-05}$

Table D.16: Weighted averaged candidate point corresponding to Gauge D

Design Point	Weights	Column A	Column B	Column C	Column D
12679, 45°	18.06 %	$-7.38 \times 10^{-07}$	$-2.18 \times 10^{-06}$	$-5.05 \times 10^{-06}$	$-4.05 \times 10^{-06}$
12680, 45°	1.77 %	$-7.30 \times 10^{-08}$	$-2.68 \times 10^{-07}$	$-6.33 \times 10^{-07}$	$-4.60 \times 10^{-07}$
12686, 45°	19.06 %	$-1.13 \times 10^{-06}$	$-2.35 \times 10^{-06}$	$-5.46 \times 10^{-06}$	$-4.23 \times 10^{-06}$
12687, 45°	54.88 %	$-2.99 \times 10^{-06}$	$-8.53 \times 10^{-06}$	$-2.01 \times 10^{-05}$	$-1.43 \times 10^{-05}$
12731, 45°	2.37 %	$-1.62 \times 10^{-07}$	$-3.70 \times 10^{-07}$	$-8.75 \times 10^{-07}$	$-6.07 \times 10^{-07}$
12732, 45°	1.99 %	$-7.57 \times 10^{-08}$	$-3.68 \times 10^{-07}$	$-8.79 \times 10^{-07}$	$-5.99 \times 10^{-07}$
12733, 45°	1.88 %	$-6.55 \times 10^{-08}$	$-3.45 \times 10^{-07}$	$-8.24 \times 10^{-07}$	$-5.62 \times 10^{-07}$
Weighted Design Point	100.00 %	$-5.24 \times 10^{-06}$	$-1.44 \times 10^{-05}$	$-3.39 \times 10^{-05}$	$-2.48 \times 10^{-05}$

Table D.17: Weighted averaged candidate point corresponding to Gauge E

Design Point	Weights	Column A	Column B	Column C	Column D
13558, 135°	12.59 %	$-5.16 \times 10^{-07}$	$-1.91 \times 10^{-06}$	$-4.51 \times 10^{-06}$	$-4.69 \times 10^{-06}$
13559, 135°	45.39 %	$-1.85 \times 10^{-06}$	$-5.53 \times 10^{-06}$	$-1.28 \times 10^{-05}$	$-1.24 \times 10^{-05}$
13565, 135°	0.40 %	$-2.17 \times 10^{-08}$	$-6.20 \times 10^{-08}$	$-1.46 \times 10^{-07}$	$-1.54 \times 10^{-07}$
13566, 135°	31.82 %	$-1.84 \times 10^{-06}$	$-3.95 \times 10^{-06}$	$-9.15 \times 10^{-06}$	$-9.06 \times 10^{-06}$
13607, 135°	9.80 %	$-3.46 \times 10^{-07}$	$-1.80 \times 10^{-06}$	$-4.28 \times 10^{-06}$	$-4.64 \times 10^{-06}$
Weighted Design Point	100.00 %	$-4.58 \times 10^{-06}$	$-1.33 \times 10^{-05}$	$-3.09 \times 10^{-05}$	$-3.10 \times 10^{-05}$

## D.6 Additional Load Reconstruction Material

### D.6.1 Load Case 1

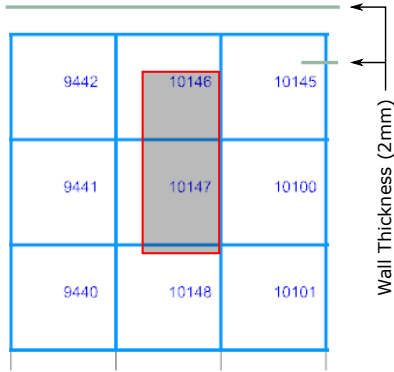


Figure D.2: Location of Gauge C in the FE model (repeated from page 98)

Table D.18: Strain values at elements surrounding Gauge C for Load Case 1.

Element	FE [mm/mm]	Measured [mm/mm]	% Difference
9442	$-5.20 \times 10^{-04}$	$-4.98 \times 10^{-04}$	4 %
10146	$-5.01 \times 10^{-04}$	$-4.98 \times 10^{-04}$	1 %
10145	$-4.95 \times 10^{-04}$	$-4.98 \times 10^{-04}$	1 %
9441	$-3.95 \times 10^{-04}$	$-4.98 \times 10^{-04}$	21 %
10147	$-3.86 \times 10^{-04}$	$-4.98 \times 10^{-04}$	22 %
10100	$-3.78 \times 10^{-04}$	$-4.98 \times 10^{-04}$	24 %
9440	$-2.66 \times 10^{-04}$	$-4.98 \times 10^{-04}$	46 %
10148	$-2.61 \times 10^{-04}$	$-4.98 \times 10^{-04}$	48 %
10101	$-2.55 \times 10^{-04}$	$-4.98 \times 10^{-04}$	49 %

$$\begin{array}{l}
 \begin{array}{l}
 (2372, 0^\circ) \rightarrow \\
 (7029, 90^\circ) \rightarrow \\
 (10146, 90^\circ) \rightarrow \\
 (12687, 45^\circ) \rightarrow \\
 (13559, 135^\circ) \rightarrow
 \end{array}
 \begin{array}{c}
 \left[ \begin{array}{cccc}
 -6.58 \times 10^{-13} & 6.66 \times 10^{-11} & 6.23 \times 10^{-07} & -2.03 \times 10^{-05} \\
 -1.07 \times 10^{-11} & 7.67 \times 10^{-06} & -2.44 \times 10^{-06} & -2.48 \times 10^{-06} \\
 1.52 \times 10^{-05} & -1.68 \times 10^{-05} & -4.32 \times 10^{-05} & -3.79 \times 10^{-05} \\
 -5.45 \times 10^{-06} & -1.55 \times 10^{-05} & -3.67 \times 10^{-05} & -2.61 \times 10^{-05} \\
 -4.08 \times 10^{-06} & -1.22 \times 10^{-05} & -2.82 \times 10^{-05} & -2.74 \times 10^{-05}
 \end{array} \right]
 \end{array}
 \begin{array}{c}
 \text{Load Vector} \\
 (\text{Load Case 1}) \\
 \left. \begin{array}{c} \downarrow \\ 0 \\ 0 \\ f_C \\ f_D \end{array} \right\}
 \end{array}
 =
 \begin{array}{c}
 \text{Measured Strain Values} \\
 \left. \begin{array}{c} \downarrow \\ -7.23 \times 10^{-06} \\ 5.20 \times 10^{-05} \\ -2.88 \times 10^{-04} \\ -2.66 \times 10^{-04} \\ -2.41 \times 10^{-04} \end{array} \right\}
 \end{array}
 \end{array}$$

Figure D.4: ‘Adapted’ proportionality matrix for Load Case 1



## D.6.2 Load Case 2

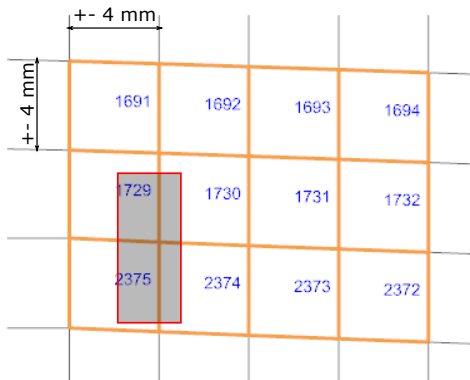


Figure 8.14: Elements surrounding Gauge A (repeated from page 74)

Table D.19: Strain values at elements surrounding Gauge A for Load Case 2.

Element	FE [mm/mm]	Measured [mm/mm]	% Difference
1691	$-1.58 \times 10^{-05}$	$-7.23 \times 10^{-06}$	119 %
1729	$-1.62 \times 10^{-05}$	$-7.23 \times 10^{-06}$	124 %
2375	$-1.07 \times 10^{-05}$	$-7.23 \times 10^{-06}$	48 %
1692	$-1.10 \times 10^{-05}$	$-7.23 \times 10^{-06}$	52 %
1730	$-9.78 \times 10^{-06}$	$-7.23 \times 10^{-06}$	35 %
2374	$-4.61 \times 10^{-06}$	$-7.23 \times 10^{-06}$	36 %
1693	$-7.82 \times 10^{-06}$	$-7.23 \times 10^{-06}$	8 %
1731	$-5.24 \times 10^{-06}$	$-7.23 \times 10^{-06}$	28 %
2373	$-5.54 \times 10^{-07}$	$-7.23 \times 10^{-06}$	92 %
1694	$-5.36 \times 10^{-06}$	$-7.23 \times 10^{-06}$	26 %
1732	$-2.55 \times 10^{-06}$	$-7.23 \times 10^{-06}$	65 %
2372	$2.25 \times 10^{-06}$	$-7.23 \times 10^{-06}$	131 %
Average Error			64 %

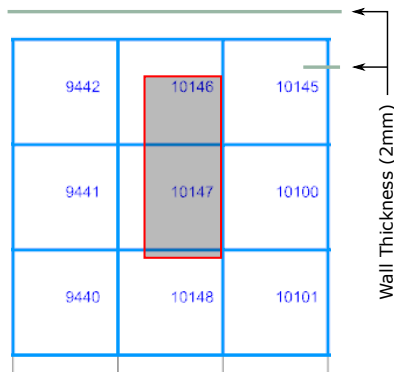


Figure D.2: Location of Gauge C in the FE model (repeated from page 98)

Table D.20: Strain values at elements surrounding Gauge C for Load Case 2.

Element	FE [mm/mm]	Measured [mm/mm]	% Difference
9442	$-3.01 \times 10^{-04}$	$-2.88 \times 10^{-04}$	4 %
10146	$-2.97 \times 10^{-04}$	$-2.88 \times 10^{-04}$	3 %
10145	$-3.01 \times 10^{-04}$	$-2.88 \times 10^{-04}$	4 %
9441	$-2.29 \times 10^{-04}$	$-2.88 \times 10^{-04}$	20 %
10147	$-2.29 \times 10^{-04}$	$-2.88 \times 10^{-04}$	21 %
10100	$-2.29 \times 10^{-04}$	$-2.88 \times 10^{-04}$	20 %
9440	$-1.55 \times 10^{-04}$	$-2.88 \times 10^{-04}$	46 %
10148	$-1.55 \times 10^{-04}$	$-2.88 \times 10^{-04}$	46 %
10101	$-1.55 \times 10^{-04}$	$-2.88 \times 10^{-04}$	46 %

## D.6.3 Load Case 3

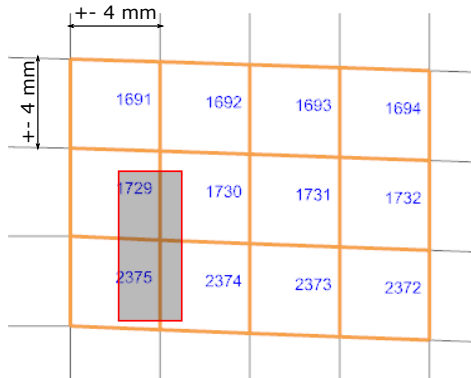


Figure 8.14: Elements surrounding Gauge A (repeated from page 74)

Table D.21: Strain values at elements surrounding Gauge A for Load Case 3.

Element	FE [mm/mm]	Measured [mm/mm]	% Difference
1691	$-9.05 \times 10^{-10}$	$9.66 \times 10^{-08}$	-100.94 %
1729	$-4.46 \times 10^{-10}$	$9.66 \times 10^{-08}$	-100.46 %
2375	$-1.78 \times 10^{-10}$	$9.66 \times 10^{-08}$	-100.18 %
1692	$-3.46 \times 10^{-10}$	$9.66 \times 10^{-08}$	-100.36 %
1730	$-1.41 \times 10^{-10}$	$9.66 \times 10^{-08}$	-100.15 %
2374	$3.75 \times 10^{-11}$	$9.66 \times 10^{-08}$	-99.96 %
1693	$-9.61 \times 10^{-11}$	$9.66 \times 10^{-08}$	-100.10 %
1731	$5.81 \times 10^{-11}$	$9.66 \times 10^{-08}$	-99.94 %
2373	$1.59 \times 10^{-10}$	$9.66 \times 10^{-08}$	-99.83 %
1694	$8.75 \times 10^{-11}$	$9.66 \times 10^{-08}$	-99.91 %
1732	$1.79 \times 10^{-10}$	$9.66 \times 10^{-08}$	-99.81 %
2372	$2.35 \times 10^{-10}$	$9.66 \times 10^{-08}$	-99.76 %

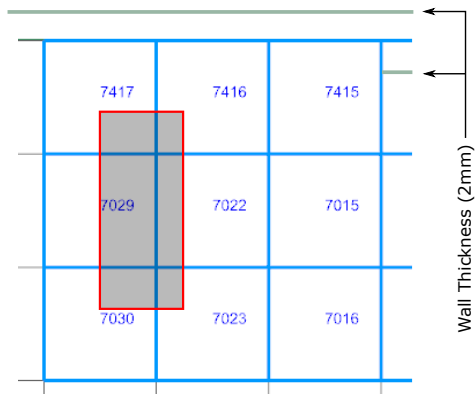


Figure D.1: Elements surrounding Gauge B (repeated from page 98)

Table D.22: Strain values at elements surrounding Gauge B for Load Case 3.

Element	FE [mm/mm]	Measured [mm/mm]	% Difference
7417	$3.84 \times 10^{-05}$	$1.07 \times 10^{-05}$	259 %
7416	$4.40 \times 10^{-05}$	$1.07 \times 10^{-05}$	311 %
7415	$4.66 \times 10^{-05}$	$1.07 \times 10^{-05}$	335 %
7029	$2.77 \times 10^{-05}$	$1.07 \times 10^{-05}$	159 %
7022	$2.99 \times 10^{-05}$	$1.07 \times 10^{-05}$	180 %
7015	$3.08 \times 10^{-05}$	$1.07 \times 10^{-05}$	188 %
7030	$1.95 \times 10^{-05}$	$1.07 \times 10^{-05}$	83 %
7023	$2.04 \times 10^{-05}$	$1.07 \times 10^{-05}$	91 %
7016	$2.06 \times 10^{-05}$	$1.07 \times 10^{-05}$	93 %

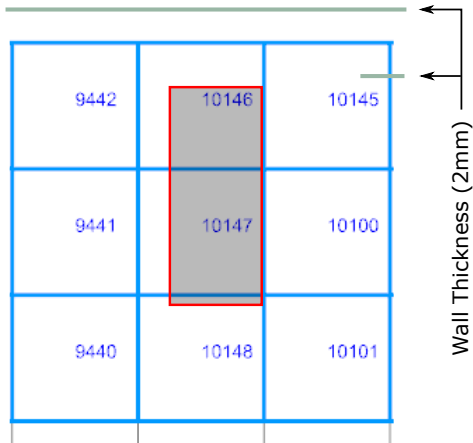


Figure D.2: Elements surrounding Gauge C (repeated from page 98)

Table D.23: Strain values at elements surrounding Gauge C for Load Case 3.

Element	FE [mm/mm]	Measured [mm/mm]	% Difference
10145	$6.27 \times 10^{-0.5}$	$6.14 \times 10^{-0.5}$	2 %
10146	$6.75 \times 10^{-0.5}$	$6.14 \times 10^{-0.5}$	10 %
9442	$6.27 \times 10^{-0.5}$	$6.14 \times 10^{-0.5}$	2 %
10100	$3.64 \times 10^{-0.5}$	$6.14 \times 10^{-0.5}$	41 %
10147	$3.90 \times 10^{-0.5}$	$6.14 \times 10^{-0.5}$	37 %
9441	$3.64 \times 10^{-0.5}$	$6.14 \times 10^{-0.5}$	41 %
10101	$2.43 \times 10^{-0.5}$	$6.14 \times 10^{-0.5}$	60 %
10148	$2.51 \times 10^{-0.5}$	$6.14 \times 10^{-0.5}$	59 %
9440	$2.43 \times 10^{-0.5}$	$6.14 \times 10^{-0.5}$	60 %

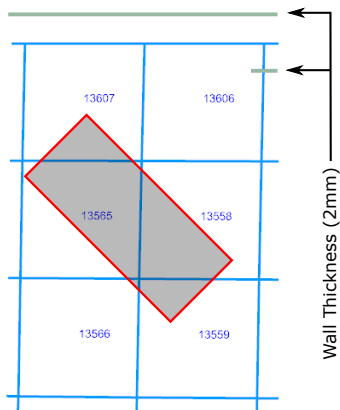


Figure D.3: Elements surrounding Gauge E (repeated from page 99)

Table D.24: Strain values at elements surrounding Gauge E for Load Case 3.

Element	FE [mm/mm]	Measured [mm/mm]	% Difference
13607	$-9.58 \times 10^{-0.5}$	$-1.04 \times 10^{-0.4}$	7.7%
13565	$-1.02 \times 10^{-0.4}$	$-1.04 \times 10^{-0.4}$	2.1%
13566	$-9.37 \times 10^{-0.5}$	$-1.04 \times 10^{-0.4}$	9.8%
13558	$-8.95 \times 10^{-0.5}$	$-1.04 \times 10^{-0.4}$	13.8%
13559	$-7.83 \times 10^{-0.5}$	$-1.04 \times 10^{-0.4}$	24.5%

# List of References

- Aggarwal, C.C. (2013). *Outlier Analysis*. Springer.
- Augustine, P. (2015). *Dynamic Moving Load Identification Using Optimal Sensor Placement and Model Reduction*. Master's thesis, University of Wisconsin-Milwaukee.
- Augustine, P., Hunter, T., Sievers, N. and Guo, X. (2016). Load identification of a suspension assembly using True-Load self transducer generation. In: *SAE 2016 World Congress and Exhibition*. SAE International. ISSN 0148-7191.
- Barry, R. (2017). *Analysis of Reinforcement Designs for Specials in Steel Pipelines Analysis of Reinforcement Designs for Specials in Steel Pipelines*. Master's thesis, Stellenbosch University.
- Barry, R. and Venter, G. (2019). Analysis of reinforcement designs for specials in steel pipelines. *International Journal of Pressure Vessels and Piping*, vol. 169, pp. 204–214.
- Bovo, F. (2020). Robustats. Available at: <https://github.com/FilippoBovo/robustats>, [2019, November 8].
- Brys, G., Hubert, M. and Struyf, A. (2004). A robust measure of skewness. *Journal of Computational and Graphical Statistics*, vol. 13, no. 4, pp. 996–1017. Available at: <https://doi.org/10.1198/106186004X12632>
- BS EN 13749:2011 (2011). Railway applications - wheelsets and bogies - method of specifying the structural requirements of bogie frames. Standard, British Standard Institution (BSI).
- Chembakassery, B. (2018). *Impact Load Identification Using Optimal Sensor Placement and Model Reduction*. Master's thesis, University of Wisconsin-Milwaukee.
- Connor, P. (2019). The railway technical website: Bogies. <http://www.railway-technical.com/trains/rolling-stock-index-1/bogies.html>.
- Cook, R., Malkus, D., Plesha, M. and Witt, R. (2002). *Concepts and Applications of Finite Element Analysis*. 4th edn. John Wiley and Sons, Inc.

- Dhingra, A., Hunter, T. and Gupta, D. (2013 October). Load recovery in components based on dynamic strain measurements. *Journal of Vibration and Acoustics*.
- Dietz, S., Netter, H. and Sachau, D. (1998). Fatigue life prediction of a railway bogie under dynamic loads through simulation. *Vehicle System Dynamics*, vol. 29, no. 6, pp. 385–402.
- Doyle, S. (2019). Welcome to pyNastran’s documentation for Master! Available at: <https://pynastran-git.readthedocs.io/en/latest/>, [2020, November 12].
- Ebrahimi, E. (2018). Available at: [https://www.researchgate.net/post/What\\_are\\_the\\_acceptable\\_values\\_for\\_the\\_percentage\\_deviation\\_DEV\\_and\\_the\\_coefficient\\_of\\_variance\\_CV#:~:text=Basically%20CV%3C10%20is%20very,CV%3E30%20is%20not%20acceptable.](https://www.researchgate.net/post/What_are_the_acceptable_values_for_the_percentage_deviation_DEV_and_the_coefficient_of_variance_CV#:~:text=Basically%20CV%3C10%20is%20very,CV%3E30%20is%20not%20acceptable.), [2020, October 25].
- Erikson, L. (2017). D-optimal design â what it is and when to use it. Available at: [https://www.youtube.com/watch?v=Zs5zvOv\\_XrI&t=19s3](https://www.youtube.com/watch?v=Zs5zvOv_XrI&t=19s3), [2020, November 6].
- Feng, C., Wang, H. and Lu, N. (2014). Log-transformation and its implications for data analysis. *Shanghai Archives of Psychiatry*, vol. 26, no. 2.
- Gupta, D. (2013). *Inverse Methods for Load Identification Augmented By Optimal Sensor Placement and Model Order Reduction*. Ph.D. thesis, University of Wisconsin-Milwaukee.
- Hagberg, A., Schult, D. and Swart, P. (2019). Network analysis in python. Available at: <https://networkx.github.io/documentation/stable/tutorial.html>, [2020, April 24].
- Heath, M. (2002). *Scientific Computing: An Introductory Survey*. 2nd edn. The McGraw-Hill Companies, Inc.
- Hibbeler, R. and Sekar, K. (2013). *Mechanics of Materials*. Pearson Education South Asia Pte Limited. ISBN 9789810694364.
- Hubert, M. and Van der Veeken, S. (2008). Outlier detection for skewed data. *Journal of Chemometrics*, vol. 22, no. 3, pp. 235–246.  
Available at: <https://onlinelibrary.wiley.com/doi/abs/10.1002/cem.1123>
- Hubert, M. and Vandervieren, E. (2008). An adjusted boxplot for skewed distributions. *Computational Statistics and Data Analysis*, vol. 52, pp. 5186–5201.  
Available at: <https://doi.org/10.1016/j.csda.2007.11.008>
- Hunter, T. (2018). Available at: <https://www.wolfstartech.com/nafems>. NAFEMS CAASE Conference Workshop.
- Johannesson, P. and Speckert, M. (eds.) (2014). *Guide to Load Analysis for Durability in Vehicle Engineering*. Automotive Series. John Wiley and Sons, Ltd.

- Kobiske, A. (2015). *Inverse Approaches for Recovery of Distributed Loads*. Master's thesis, University of Wisconsin-Milwaukee.
- Luo, R., Gabbitas, B. and V Brickle, B. (1994). Fatigue life evaluation of a railway vehicle bogie using an integrated dynamic simulation. *Proceedings of the Institution of Mechanical Engineers, Part F: Journal of Rail and Rapid Transit*, vol. 208, pp. 123–132.
- Maas, J. (2015). Use of Abaqus/CAE and True-Load to determine external and internal loading of a full suspension mountain bicycle. 2015 SIMULIA Community Conference.
- Masroor, S. and Zachary, L. (1991). Designing an all-purpose force transducer. In:
- Miller, A. and Nguyen, N. (1994). Algorithm as 295: A fedorov exchange algorithm for d-optimal design. *Journal of the Royal Statistical Society. Series C (Applied Statistics)*, vol. 43, no. 4, pp. 669–677.
- Murphy, C. and Tanner, W. (2015). 1243 adt scraper tail validation project. Online.
- Myers, R., Montgomery, D. and Anderson-Cook, C. (2009). *Response Surface Methodology: Process and Product Optimization Using Designed Experiments*. 3rd edn. John Wiley and Sons, Inc., Hoboken, New Jersey.
- nCode (2020). nCode. Available at: <https://www.ncode.com>, [2020, October 15].
- Nickerson, B. (2017). *Development of an integrated numerical method for the fatigue analysis of railway bogies*. Master's thesis, Mechanical Engineering, University of Stellenbosch, Stellenbosch, South Africa.
- Plaskitt, R. (2016). Loads reconstruction. HBM Prenscia: Business Document.
- Siemens (2014a). *Element Library Reference*. Siemens Product Lifecycle Management Software Inc.
- Siemens (2014b). *NX Nastran User's Guide*. Siemens Product Lifecycle Management Software Inc.
- Slowinski, D. (2017). Front-end loader linkage durability analysis using load input from True-Load. Available at: <https://www.wolfstartech.com/cnh>. Wolf Star Technologies Product Review.
- Stichel, S. and Knothe, K. (1998). Fatigue life prediction for an S-train bogie. *Vehicle System Dynamics*, vol. 29, no. sup1, pp. 390–403.
- Trutna, L., Spagon, P., del Castillo, E., Moore, T., Hartley, S. and Hurwitz, A. (2013). *NIST/SEMATECH e-Handbook of Statistical Methods*, chap. 5.

- Wagle, B. (2018). *Transient Load Recovery Using Strain Measurements and Model Reduction*. Master's thesis, University of Wisconsin-Milwaukee.
- Walpole, R., Myers, R., Myers, S. and Keying, Y. (2016). *Probability and Statistics for Engineers and Scientists*. 9th edn. Pearson.
- Wannenburg, J. (2007). *A study of fatigue loading on automotive and transport structures*. Ph.D. thesis, University of Pretoria.
- Wannenburg, J. and Heyns, S. (2010). An overview of numerical methodologies for durability assessment of vehicle and transport structures. *International Journal of Vehicle Systems Modelling and Testing*, vol. 5.
- Wickham, M.J., Riley, D.R. and Nachtsheim, C.J. (1995). Integrating optimal experimental design into the design of a multi-axis load transducer. In:
- Widnall, S. (2009). Vectors, matrices and coordinate transformations. Online.
- Wili, P., Maquer, G., Panyasantisuk, J. and Zysset, P. (2017 06). Estimation of the effective yield properties of human trabecular bone using nonlinear micro finite element analyses. *Biomechanics and Modeling in Mechanobiology*, vol. 16.
- Wolf Star Technologies (2017). Load calculation software. Available at: <https://www.wolfstartech.com>, [2020, October 15].
- Xiaofeng, L., Caixia, G., Hunter, T. and Haidong, L. (nd). Research on reverse evaluation of the load based on True-Load algorithm. Peer-Reviewed Paper (Dalian Jiaotong University).